

Herschel-PACS[★] photometry of faint stars for sensitivity performance assessment and establishment of faint FIR primary photometric standards

U. Klaas¹, Z. Balog¹, M. Nielbock^{1,2}, T.G. Müller³, H. Linz¹, and Cs. Kiss⁴

¹ Max-Planck-Institut für Astronomie (MPIA), Königstuhl 17, 69117 Heidelberg, Germany
e-mail: klaas@mpia.de

² Haus der Astronomie, MPIA-Campus, Königstuhl 17, 69117 Heidelberg, Germany

³ Max-Planck-Institut für extraterrestrische Physik (MPE), PO Box 1312, Giessenbachstraße, 85741 Garching, Germany

⁴ Konkoly Observatory, Research Centre for Astronomy and Earth Sciences, Hungarian Academy of Sciences, 1121 Budapest, Konkoly Thege Miklós út 15-17, Hungary

Received 23 August 2017 / Accepted 7 December 2017

ABSTRACT

Aims. Our aims are to determine flux densities and their photometric accuracy for a set of seventeen stars that range in flux from intermediately bright ($\lesssim 2.5$ Jy) to faint ($\gtrsim 5$ mJy) in the far-infrared (FIR). We also aim to derive signal-to-noise dependence with flux and time, and compare the results with predictions from the *Herschel* exposure-time calculation tool.

Methods. We obtain aperture photometry from *Herschel*-PACS high-pass-filtered scan maps and chop/nod observations of the faint stars. The issues of detection limits and sky confusion noise are addressed by comparison of the field-of-view at different wavelengths, by multi-aperture photometry, by special processing of the maps to preserve extended emission, and with the help of large-scale absolute sky brightness maps from *AKARI*. This photometry is compared with flux-density predictions based on photospheric models for these stars. We obtain a robust noise estimate by fitting the flux distribution per map pixel histogram for the area around the stars, scaling it for the applied aperture size and correcting for noise correlation.

Results. For 15 stars we obtain reliable photometry in at least one PACS filter, and for 11 stars we achieve this in all three PACS filters (70, 100, 160 μm). Faintest fluxes, for which the photometry still has good quality, are about 10 – 20 mJy with scan map photometry. The photometry of seven stars is consistent with models or flux predictions for pure photospheric emission, making them good primary standard candidates. Two stars exhibit source-intrinsic far-infrared excess: β Gem (Pollux), being the host star of a confirmed Jupiter-size exoplanet, due to emission of an associated dust disk, and η Dra due to dust emission in a binary system with a K1 dwarf. The investigation of the 160 μm sky background and environment of four sources reveals significant sky confusion prohibiting the determination of an accurate stellar flux at this wavelength. As a good model approximation, for nine stars we obtain scaling factors of the continuum flux models of four PACS fiducial standards with the same or quite similar spectral type. We can verify a linear dependence of signal-to-noise ratio (S/N) with flux and with square root of time over significant ranges. At 160 μm the latter relation is, however, affected by confusion noise.

Conclusions. The PACS faint star sample has allowed a comprehensive sensitivity assessment of the PACS photometer. Accurate photometry allows us to establish a set of five FIR primary standard candidates, namely α Ari, ε Lep, ω Cap, HD 41047 and 42 Dra, which are 2 – 20 times fainter than the faintest PACS fiducial standard (γ Dra) with absolute accuracy of $< 6\%$. For three of these primary standard candidates, essential stellar parameters are known, meaning that a dedicated flux model code may be run.

Key words. Space vehicles: instruments – Methods: data analysis – Techniques: photometric – Infrared: stars – Stars: atmospheres – Radiation mechanisms: thermal

1. Introduction

The photometric calibration of the PACS photometer (Poglitsch et al. 2010) on-board the *Herschel* Space Observatory (Pilbratt et al. 2010) is based on celestial standard stars (Balog et al. 2014; Nielbock et al. 2013). These primary standard stars have well-modelled spectral energy distributions (SEDs) of their photospheric emission and an accurate absolute calibration in the K-band (Dehaes et al. 2011). They are still relatively bright in the far-infrared (in the range 1 - 10 Jy) to achieve high signal-to-noise ratios (S/N) within reasonable measurement times. Be-

sides repeated measurements of these standard stars, a set of fainter secondary standard stars was repeatedly measured by PACS as part of the calibration program during the *Herschel* Performance Verification and Routine Operations periods. This included sources down to a few mJy. The PACS photometer is linear over a flux range exceeding the primary standard fluxes, with an optimized detector set-up for the flux background from the telescope. Flux nonlinearity is therefore an issue for considerably brighter sources and has been addressed elsewhere (Müller et al. 2016). However, including fainter sources with well known flux predictions allows to us address the following questions:

1) How does the sensitivity scale with flux and time?

[★] *Herschel* is an ESA space observatory with science instruments provided by European-led Principal Investigator consortia and with important participation from NASA.

Table 1. Faint secondary standards observed by *Herschel*-PACS. Source fluxes from Gordon et al. (2007) are for an effective wavelength of $71.42\ \mu\text{m}$ and have been colour-corrected to the PACS central wavelength of $70\ \mu\text{m}$ by dividing by the factor 0.961 (cf. Müller et al. 2011) for a Rayleigh-Jeans-tail-type SED. 100 and $160\ \mu\text{m}$ fluxes for these sources are then extrapolated values for this adopted SED.

HD	Other name	Model flux prediction (mJy)			Spectral type	Reference
		f_{70}	f_{100}	f_{160}		
62509	β Gem	2457 ($\pm 5.73\%$)	1190 ($\pm 5.73\%$)	455.9 ($\pm 5.73\%$)	K0IIIb	Cohen et al. (1996) ^a
12929	α Ari	1707 ($\pm 5.9\%$)	831.4 ($\pm 5.9\%$)	321.0 ($\pm 5.9\%$)	K2III	Cohen et al. (1996) ^a
32887	ε Lep	1182 ($\pm 5.9\%$)	576.2 ($\pm 5.9\%$)	222.7 ($\pm 5.9\%$)	K4III	Cohen et al. (1996) ^a
198542	ω Cap	857.7 ($\pm 6.03\%$)	418.0 ($\pm 6.03\%$)	161.5 ($\pm 6.03\%$)	M0III	Cohen et al. (1996) ^a
148387	η Dra	479.5 ($\pm 3.38\%$)	232.6 ($\pm 3.45\%$)	89.4 ($\pm 3.51\%$)	G8III	Hammersley et al. (1998) ^b
180711	δ Dra	428.9 ($\pm 5.7\%$)	207.7 ($\pm 5.7\%$)	79.6 ($\pm 5.7\%$)	G9III	Cohen et al. (1996) ^a
139669	θ Umi	286.2 ($\pm 5.67\%$)	139.5 ($\pm 5.67\%$)	53.9 ($\pm 5.67\%$)	K5III	Cohen et al. (1996) ^a
41047	HR 2131	195.6 ($\pm 5.96\%$)	95.4 ($\pm 5.96\%$)	36.9 ($\pm 5.96\%$)	K5III	Cohen et al. (1996) ^a
170693	42 Dra	153.7 ± 4.6	75.3 ($\pm 3.0\%$)	29.4 ($\pm 3.0\%$)	K1.5III	Gordon et al. (2007)
138265	HR 5755	115.9 ± 4.0	56.8 ($\pm 3.5\%$)	22.2 ($\pm 3.5\%$)	K5III	Gordon et al. (2007)
159330	HR 6540	64.2 ± 2.1	31.5 ($\pm 3.3\%$)	12.3 ($\pm 3.3\%$)	K2III	Gordon et al. (2007)
152222	SAO 17226	39.4 ± 1.9	19.3 ($\pm 5.0\%$)	7.5 ($\pm 5.0\%$)	K2III	Gordon et al. (2007)
39608	SAO 249364	30.9 ± 1.2	15.1 ($\pm 4.0\%$)	5.9 ($\pm 4.0\%$)	K5III	Gordon et al. (2007)
181597	HR 7341	28.0 ($\pm 3.29\%$)	13.6 ($\pm 3.34\%$)	5.2 ($\pm 3.42\%$)	K1III	Hammersley et al. (1998) ^b
15008	δ Hyi	22.9 ± 0.8	11.2 ($\pm 3.5\%$)	4.4 ($\pm 3.5\%$)	A1/2V	Gordon et al. (2007)
156729	e Her	12.0 ($\pm 3.21\%$)	5.8 ($\pm 3.25\%$)	2.2 ($\pm 3.28\%$)	A2V	Hammersley et al. (1998) ^b
168009	HR 6847	10.0 ($\pm 3.40\%$)	4.9 ($\pm 3.45\%$)	1.9 ($\pm 3.50\%$)	G2V	Hammersley et al. (1998) ^b

Notes. Source flux models are from

^(a) http://general-tools.cosmos.esa.int/iso/users/expl_lib/ISO/wwwcal/isoprep/cohen/extraps/

^(b) http://general-tools.cosmos.esa.int/iso/users/expl_lib/ISO/wwwcal/isoprep/gbpp/

- 2) How does the finally achieved sensitivity compare with predictions by the PACS exposure-time calculator of the *Herschel* observation planning tool?
- 3) What is the impact and consistency of the applied data reduction scheme on the resulting source flux for fainter and fainter flux contributions on top of the telescope background level?
- 4) What is the impact of background confusion noise on the resulting fluxes and the sensitivity limit?

Ultimately, some of the faint sources may be characterized well enough to become primary standard sources for future powerful and sensitive FIR space telescopes, such as SPICA (e.g. Sibthorpe et al. 2015), Millimetron (e.g. Smirnov et al. 2012) or the Origins Space Telescope (Meixner et al. 2017).

Most of the observations have been done in mini-scan-map mode, but we have included also a valuable set of complementary chop/nod point-source photometry. We first report the scan map photometry including the sensitivity verification. Then we present the chop/nod photometry and compare it with the scan map results. Finally, we analyse the source spectral energy distributions (SEDs) by comparison with model SEDs and establish which sources are suitable as accurate celestial standards.

2. Source selection

In preparation of the PACS in-flight photometric calibration, secondary standard source lists with stars described in Cohen et al. (1996), Hammersley et al. (1998), and Gordon et al. (2007) were prepared by the PACS Instrument Control Centre (ICC) team. Depending on the source visibility during the *Herschel* mission, a subset of sources from these lists were observed to cover the flux range from 0.5 - 2.5 Jy down to 2 - 10 mJy over the three photometer wavelengths 70, 100, and $160\ \mu\text{m}$. The finally observed 17 sources are listed in Table 1.

3. Scan map photometry

Fifteen out of the 17 sources were observed in the PACS mini-scan-map point-source observing mode. This was the recommended scientific observing mode for point sources after *Herschel*'s Science Demonstration Phase (SDP), because it had a better sensitivity and allowed a better characterization of the source vicinity and larger-scale structures of the background than chop/nod photometry. The satellite scans were mostly done with the nominal $20''/s$ speed; a few early ones were done with the originally adopted speed of $10''/s$. The scan map dimension parameters are usually $3'$ leg length and ten legs with a separation of $4''$ with scan angles in array coordinates of 70° and 110° (along the diagonal of the bolometer arrays). Only a few early measurements had different parameters from these values, when still probing for the optimum parameter set. In the case of repetition factors larger than 1, in particular for our faintest targets, the whole scan map was repeatedly executed according to the specified factor. We note that a repetition factor may have been optimized for the short wave filter measurement and is hence less optimal for the $160\ \mu\text{m}$ filter, where the star is fainter. The observations were usually done in high gain mode. There are a few exceptions taken for comparative performance checks. Selected observing parameters are listed for all individual scan map observations in Tables A.3 to A.5.

3.1. Data analysis and calibration

The data reduction and calibration performed in HIPE¹ (Ott 2010) followed the description in Balog et al. (2014), applying the high-pass filter (HPF) algorithm to remove the $\frac{1}{f}$ -noise

¹ HIPE is a joint development by the *Herschel* Science Ground Segment Consortium, consisting of ESA, the NASA *Herschel* Science center, and the HIFI, PACS and SPIRE consortia.

Table 2. Relevant scan map parameters for photometry and noise determination. $r_{\text{aper}}^{\text{phot}}$ is the radius of the aperture used for the point-source photometry, c_{aper} is the corresponding correction factor to scale the flux to its total value, $cc(\lambda_{\text{ref}})$ is the colour-correction factor to derive the source flux at the reference wavelength λ_{ref} of the filter (Müller et al. 2011), HPF is the abbreviation for high pass filter, pixfrac is the ratio of drop size to input pixel size used for the drizzling algorithm (Fruchter & Hook 2002) within the photProject() mapper, outpix is the output pixel size in the final map, N_{aper} is the number of output pixels inside the photometry aperture with $r_{\text{aper}}^{\text{phot}}$, and f_{corr} is the correlated noise correction factor depending on the combination of HPF radius / pixfrac / outpix.

Filter (μm)	$r_{\text{aper}}^{\text{phot}}$ ($''$)	c_{aper}	$cc_{\text{star}}(\lambda_{\text{ref}})$	HPF radius ^a	pixfrac	outpix ($''$)	N_{aper}	f_{corr}
70	5.6	1.61	1.016	15	1.0	1.1	81.42	3.13
100	6.8	1.56	1.033	20	1.0	1.4	74.12	2.76
160	10.7	1.56	1.074	35	1.0	2.1	81.56	4.12

Notes. ^(a) This parameter determines the elementary section of a scan over which the high-pass filter algorithm computes a running median value. Its unit is "number of read-outs". The spatial interval between two readouts is $\alpha_{\text{ro}} = \frac{v_{\text{scan}}}{v_{\text{ro}}}$. For the standard $v_{\text{ro}} = 10$ Hz read-out scheme in PACS prime mode, and a scan speed $v_{\text{scan}} = 20$ "/s, the spatial interval α_{ro} between two read-outs corresponds to 2". The entire width of the HPF window ($''$) = $[(2 \times \text{HPF radius}) + 1] \times \alpha_{\text{ro}}$.

from the scan data of the bolometer detectors. A few recent developments in PACS data reduction (gyro correction and updated pointing products, refined focal plane geometry calibration and more precise timing of the detector readouts) have been included.

The source flux is determined by aperture photometry. The relation between the final stellar flux at the reference wavelength of the respective filter (70, 100 and 160 μm), $f_{\text{star}}(\lambda_{\text{ref}})$, and the integrated background subtracted map flux inside the aperture, f_{aper} , is given by

$$f_{\text{star}}(\lambda_{\text{ref}}) = \frac{c_{\text{aper}}(\lambda_{\text{ref}}) \times f_{\text{aper}}(\lambda_{\text{ref}})}{cc_{\text{star}}(\lambda_{\text{ref}})}, \quad (1)$$

where c_{aper} is the aperture correction factor to get the total non-colour-corrected source flux, f_{tot} . Since the PACS calibration scheme yields a flux related to a SED $\nu \times f = \text{const.}$ the colour-correction factor $cc_{\text{star}}(\lambda_{\text{ref}})$ provides the appropriate correction for the stellar SED (5000 K blackbody). The aperture and colour-correction factors are listed in Table 2.

For the investigation of background contamination we also used the JScanam algorithm (Graciá-Carpio et al. 2015), which better preserves extended emission. For the final projection of all data, the HIPE algorithm photProject() was applied; the selected mapping parameters pixfrac and output pixel size are listed in Table 2.

3.2. Optimum aperture size for faint star photometry

For the faint star photometry we have selected smaller apertures (cf. Table 2) than were used for the fiducial star photometry in Balog et al. (2014) (12'', 12'', 22'', respectively). These are the same aperture sizes as for chop-nod photometry.

These smaller apertures, which are adapted to the PSF FWHM in the respective filter, result in a much higher flux reproducibility among the individual measurements and hence a smaller standard deviation of the mean source flux, as well as more reliable and consistent (with regard to the relative spectral shape) source flux measurements for the faintest sources. This is shown in Table A.1 in Appendix A.1, where photometry with the large standard apertures is compared with the photometry applying the smaller apertures. For the cases with ≥ 4 individual measurements the improvement in reproducibility can be up to a factor of 2 – 3. The finally achieved average reproducibility

Table 3. Average photometric reproducibility and its standard deviation for the six brightest stars with at least eight individual measurements per filter.

Filter (μm)	Photometric reproducibility (%)
70	0.23 ± 0.15
100	0.57 ± 0.63
160	1.85 ± 1.80

for sources with eight individual measurements in each filter is listed in Table 3.

From a statistical analysis of the signals of the approximately 21,000 PACS photometer internal calibration source measurements, Moór et al. (2014) derived a stability of the PACS bolometer response of about 0.2% standard deviation or 2%, 3%, and 5% peak-to-peak at 70, 100, and 160 μm , respectively, after correction for evaporator temperature effects and initial signal drifts after cooler recycling and photometer switch-on. Our photometry includes the evaporator temperature correction and practically all measurements are outside phases with noticeable initial signal drifts. The mean reproducibility of the 70 μm stellar fluxes comes close to the standard deviation of the bolometer response. At 100 and 160 μm the mean reproducibility is less good and shows a larger scatter, firstly because the sources are weaker and secondly because the uncertainties in background subtraction are higher.

3.3. Noise and S/N determination

A flux histogram has been constructed for all output pixels of the image map, where the corresponding coverage map² indicates that $\text{cover}_{\text{pix}} \gtrsim \frac{1}{2} \text{cover}_{\text{max}}$. This is justified, since the stars are located in the central part of the map around the highest coverage. A Gauss fit has been performed to the histogram but restricted to the part with fluxes below the bin associated with the maximum number, representing in first approximation the background level, and hence avoiding contamination of the derived

² The coverage map gives the sum of all complete (= 1.0) or partial (< 1.0) coverage occurrences of each map output pixel by any physical array pixel, reduced to the specified drop size, from all unmasked read-out frames along the scan time-line.

noise per pixel, σ_{pix} , by flux of faint sources (to optimize the quality of the fit, actually about 10 bins above the bin with the maximum number are included in the fit). An example of this procedure is shown in Fig. 1. This method provides very reliable and homogeneous noise figures.

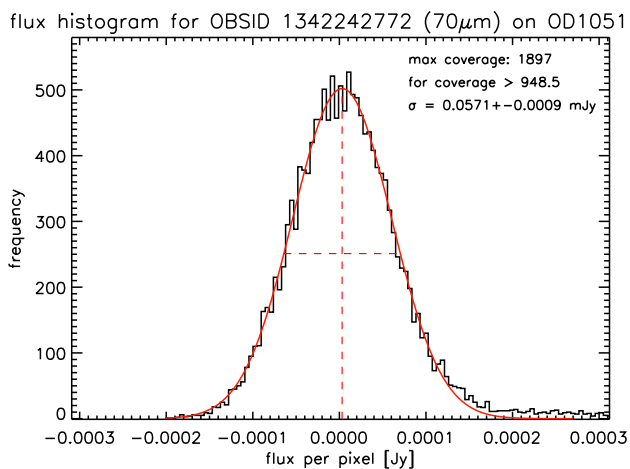


Fig. 1. Illustration of the histogram method to determine the background noise. The example shows the number of pixels per flux bin of the $70\ \mu\text{m}$ map of OBSID 1342242772 (β Gem on OD 1051) for all pixels with a coverage value $> \frac{1}{2} \text{cover}_{\text{max}}$ (>948.5). The displayed flux distribution is cut off towards higher fluxes. The red curve is the Gaussian fit to this histogram. For this fit we took all bins left of the distribution maximum into account, but limited the right fitting range to ten bins beyond the distribution maximum in order to avoid a bias of the fitted width by true source flux. The vertical and horizontal red dashed lines indicate the mean background level and the $FWHM = \sqrt{2 \log(2)} \sigma_{\text{pix}}$, respectively. For fluxes per pixel above ≈ 0.12 mJy the contribution by true sources becomes noticeable.

For our photometric measurements, the noise inside the measurement aperture must be determined from the noise per pixel σ_{pix} . This is given by

$$\sigma_{\text{aper}} = \sqrt{N_{\text{aper}}} \times \sigma_{\text{pix}}, \quad (2)$$

with N_{aper} being the number of map output pixels inside the measurement aperture. The respective numbers of N_{aper} are listed in Table 2.

The high pass filtering and map projection lead to correlated noise which must be corrected to reconstruct the real detector noise (Popesso et al. 2012). This is achieved by applying the correlated noise correction factor f_{corr}

$$f_{\text{corr}} = \sum_{0 \leq i+j+k \leq n}^{n=3} c_{ijk} \text{hp} f^i \text{outpix}^j \text{pixfrac}^k \quad (3)$$

$$k = 0, n; \quad j = 0, (n-k); \quad i = 0, (n-k-j)^3.$$

Hence, the noise corrected for correlated noise inside the measurement aperture is

$$\sigma_{\text{aper,corr}} = \sqrt{N_{\text{aper}}} \times f_{\text{corr}} \times \sigma_{\text{pix}}. \quad (4)$$

The S/N of the measurement is then determined as

$$\frac{S}{N} = \frac{f_{\text{aper}}}{\sigma_{\text{aper,corr}}}, \quad (5)$$

³ c_{ijk} is related to the 20 parameters P(0) . . . P(19) in Table 9 of Popesso et al. (2012) by running three nested DO-loops with (from outer to inner) $k = 0, n; j = 0, (n-k);$ and $i = 0, (n-k-j)$.

Table 4. RMS noise values $f_{1\sigma,1s}$, the 1σ ($\frac{S}{N} = 1$) flux level being achievable with an integration time of 1 s, used in HSpot for S/N calculation.

Filter (μm)	$f_{1\sigma,1s}$ (mJy)
70	30.6
100	36.0
160	68.5

Table 5. Central coverage time of a source during a scan map execution depending on the scan map parameters (scan leg length, scan leg separation and number of scan legs) as calculated by HSpot. The combination in bold face is the default combination used for the majority of the measurements.

Scan map parameters ("/#)	Map angle (deg)	$t_{\text{obscovercent}}$ (s)
scan speed 20"/s		
150/4/10	70/110	80
180/4/10	70/110	90
210/4/20	90	220
210/4/25	90	275
240/4/8	63/117	96
90/5/9	70/110	45
210/15/4	90	44
scan speed 10"/s		
120/3/21	80/100	252
150/4/9	85/95	144
210/4/20	90	440
210/4/25	90	550
90/5/9	60/120	90
120/5/9	80/100	108
210/15/4	90	88

where f_{aper} is the part of the source flux measured inside the aperture.

3.4. The dependence of S/N on exposure time and flux

The measured S/Ns are compared with the S/N predictions of the exposure time calculation tool in the *Herschel* Observatory Planning Tool HSpot (Herschel-Spot (HSpot) User's Guide: Herschel Observation Planning Tool 2013). HSpot calculates the S/Ns based on an rms noise due to telescope thermal noise emission and the electrical noise of the read-out electronics, cf. Table 4:

$$\frac{S}{N}_{\text{HSpot}} = \frac{f_{\text{star}}}{f_{1\sigma,1s}} \sqrt{n_{\text{rep}} t_{\text{obscover}}}, \quad (6)$$

with f_{star} using the colour- and aperture-corrected total stellar flux.

This S/N scales with the square root of the coverage time of the source during one scan map, t_{obscover} and the number of scan map repetitions, n_{rep} . For mini-scan-maps, t_{obscover} is maximum at the map centre and decreases towards the borders. In analogy to the noise determination in the final maps, as described in Sect. 3.3, we use $t_{\text{obscover}} = \frac{1}{2} t_{\text{obscovercent}}$. The value of t_{obscover} depends on the scan map parameters (scan leg length, scan leg separation and number of scan legs) and is listed in Table 5 for all scan map parameter combinations used for our observations.

Figure 2 shows the dependence of the achieved S/Ns on time, represented as number of scan repetitions, and the comparison with the HSpot prediction. This includes combined maps of scan and cross-scans, which have the sum of the scan repetitions of the individual maps.

For 70 and 100 μm measurements we find $S/N \propto \sqrt{n_{\text{rep}}}$. There are deviations from this relation in that respect that the S/N of the combined maps is higher than the expected factor of $\sqrt{2}$ by a few percent. The ratio of the average measured S/N to the HSpot prediction is 1.14–1.22 at 70 μm and 1.03–1.09 at 100 μm , respectively. Given the fact that the HSpot prediction is for half maximum coverage and the noise determination in the maps is above a threshold of half maximum coverage, the measured S/N can be considered as consistent with the HSpot prediction.

For the 160 μm measurements we find for small repetition numbers ($n_{\text{rep}} \leq 12$) that the S/N increases with the $\sqrt{n_{\text{rep}}}$ for single and combined maps. For higher repetition numbers it is obvious that the increase of the measured S/Ns is flatter. This flattening is caused by confusion noise, which will be discussed in the following Section. The ratio of the average measured S/N to the HSpot prediction is around 0.80. We note, however, that there is some margin in achievable S/N depending on the selection of the high-pass filter (HPF) radius. We calculate a decrease of the resulting noise by $\approx 23\%$ between HPF radius = 40 read-outs and HPF radius = 15 read-outs for $\text{pixfrac} = 1.0$ and output pixel size of $2''.0$ according to the formalism in Popesso et al. (2012). The latter harsh filter width would only be applied for maps with very weak sources covering only a few pixels. The HSpot values were derived from cosmological fields, where harsh HPF filter widths could be applied, and that would explain the somewhat worse performance for our milder HPF radius of 35 read-outs.

After OD 1375, half of the red photometer array was lost. We have one good case, namely the 160 μm observations of ϵ Lep from OD 1377, to check the performance relative to full array observations. With regard to comparable observations from ODs 502, 833, and 1034 (cf. Table A.5), we find the following: The coverage is 0.51 of the full array map, but the noise is increased by only a factor of 1.21.

In the case of η Dra the performance of scan speeds 10"/s and 20"/s can be inter-compared. While the coverage time of the 10"/s scan speed maps is always greater than or equal to twice the coverage time of the 20"/s scan speed (cf. configurations in Tables A.3 to A.5 and corresponding coverage times in Table 5), the measured S/N of the 20"/s scan speed is above the HSpot prediction at 70 and 100 μm , while the measured S/Ns of all 10"/s scan speed combinations are below the HSpot prediction. This is a clear demonstration that the 20"/s scan speed maps are relatively more sensitive than their 10"/s scan speed counterparts. At 160 μm this is even more pronounced; the S/N of the 20"/s scan speed map with half of the coverage time is better than that of the 10"/s scan speed map with otherwise identical map parameters.

Figure 3 shows the dependence of the achieved S/Ns on flux. For the 70 and 100 μm filters we can verify that the S/N scales linearly with flux over two decades of flux and at least down to total (aperture corrected) source fluxes of 30 mJy and 18 mJy, respectively. For the 160 μm filter the linearity with flux can be verified over about one decade in flux down to a total (aperture corrected) source flux of 85 mJy for repetition factors 1 – 12. For fainter fluxes measurements with higher (≥ 20) repetition factors are necessary to achieve a S/N which is sufficiently above values close to the detection limit ($S/N \lesssim 1.5$, cf. Sect. 3.6). These high repetition factors give an increase in S/N that is smaller

than expected, which we explain in the following Section as being due to a confusion noise contribution. Since the confusion noise contribution is not the same in the different source fields, the linearity of the S/N with flux cannot be verified any more straightforwardly in the 160 μm flux range below 85 mJy.

3.5. Impact on S/N by background confusion noise

In particular at 160 μm , there may be another relevant noise source, which is FIR background confusion noise. This is composed of a cosmic infrared background component and a galactic cirrus component. Examples of background confusion, which also affects the source photometry, are shown in Figs. 5 and 6. The confusion noise is independent of on-source observation time, that is, in the case of approaching the confusion noise limit, the S/N does not improve anymore with on-source observation time.

$$\frac{S}{N}_{\text{HSpot,conf}} = \frac{f_{\text{star}}}{\sqrt{\frac{f_{1\sigma,1s}^2}{n_{\text{rep}} t_{\text{obscover}}} + f_{\text{confnoise}}^2}}. \quad (7)$$

This leads to the effect that the S/N curve with time flattens out as observed for the 160 μm S/Ns in Fig. 2. For our source fields, HSpot returns a 160 μm point source equivalent confusion noise estimate $f_{\text{confnoise}}$ between 1.3 and 1.5 mJy. The typical on-source observation time for repetition factor 1 is 45 s, resulting in a 160 μm noise level of 10 mJy. This is about a factor of 7 higher than the estimated confusion noise and only for large scan map repetition factors (>10), does the confusion noise become significant.

3.6. Detection limits

HD 181597 and HD 15008 (δ Hyi) are good examples for non-detections at 160 μm , because the expected source flux is below the detection limit. Both sources have a clear detection at 70 μm ($S/N = 30$ and 15, respectively), which allows to identify the expected source position on the 160 μm maps (see Fig. 4). Table 6 lists the determined S/Ns, which are <1.5 (we note, that the S/N measurement in the map is actually higher by the factor $f_{\text{corr}} = 4.12$, which corresponds to the classic S/N detection limit of 5 – 6). This is in accordance that no source can be detected at the location of the star in the 160 μm map.

Table 6. S/N determination at 160 μm for HD 181597 and HD 15008, which are below the detection limit ($S/N \lesssim 1.5$) at this wavelength.

HD (μm)	f_{predict} (mJy)	f_{aper} (mJy)	$\sigma_{\text{aper,corr}}$ (mJy)	$\frac{S}{N}$
181597	5.2	3.3	2.6	1.3
15008	4.4	2.8	3.2	0.9

3.7. Confusion by neighboring sources and cirrus

The fainter the star, the higher the probability, in particular at 100 and 160 μm , that nearby sources confuse the source flux inside the measurement aperture.

A clear case of confusion by neighboring sources is shown in Fig. 5 for the star HD 159330. While at 70 μm the star is more or less the only visible source inside the field, at 100 μm a small

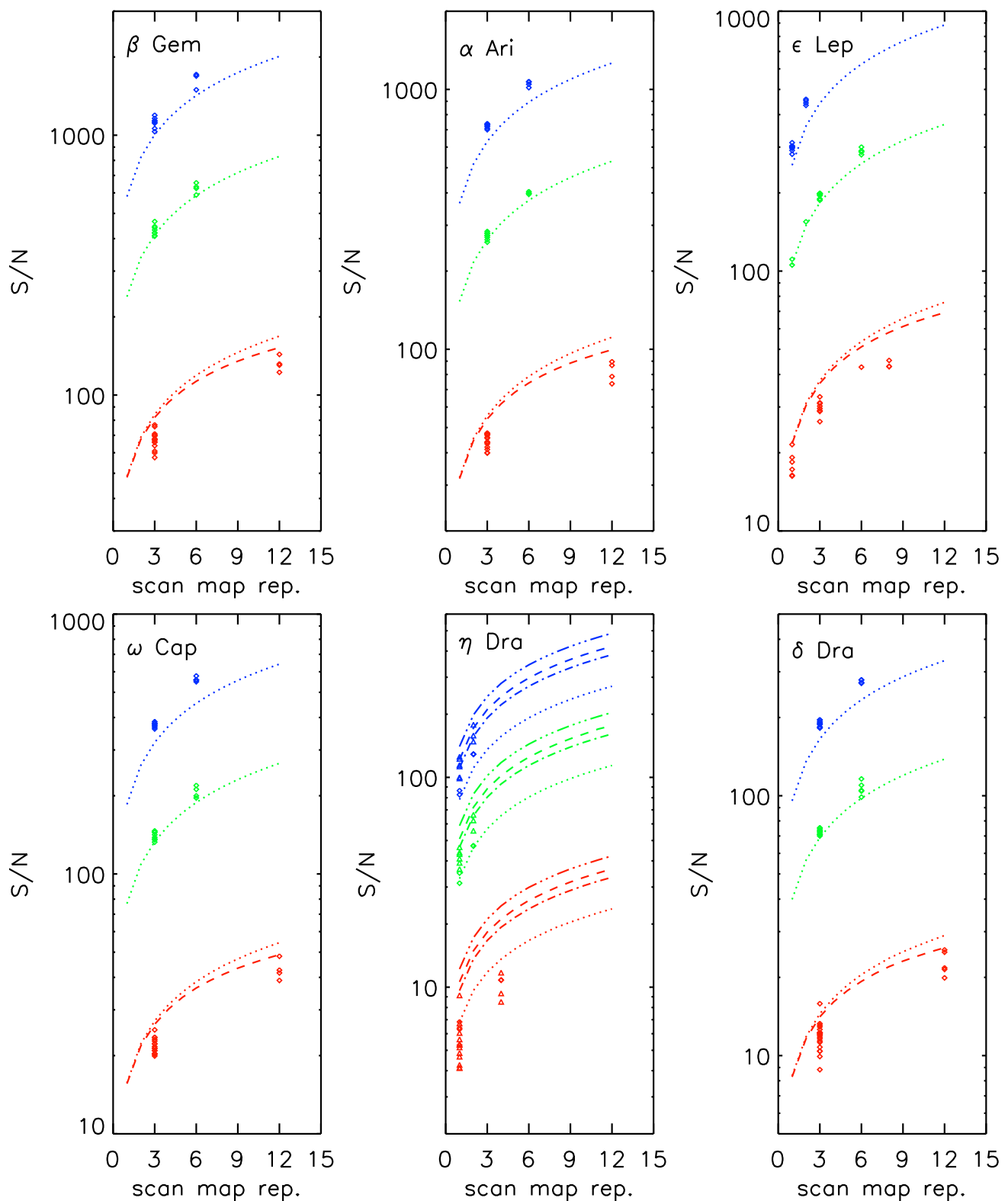


Fig. 2. Measured S/Ns for mini-scan-map photometry depending on the number of repetitions. Blue, green, and red symbols represent measurements in the three filters, 70, 100, and 160 μm , respectively. Diamond symbols indicate a scan speed of 20"/s, triangles a scan speed of 10"/s. The dotted lines in the respective colours show the S/N prediction by the PACS exposure time calculator of the *Herschel* observation planning tool HSpot for the measured colour corrected stellar flux. Long dashed red lines indicate the S/N prediction including confusion noise. An exception is the panel of η Dra, where the sets of four dotted, dashed, and dashed-dotted lines represent the sensitivity predictions for four different map parameter combinations; the upper three are with 10"/s scan speed, the lowest one is with 20"/s scan speed. For more details, see text.

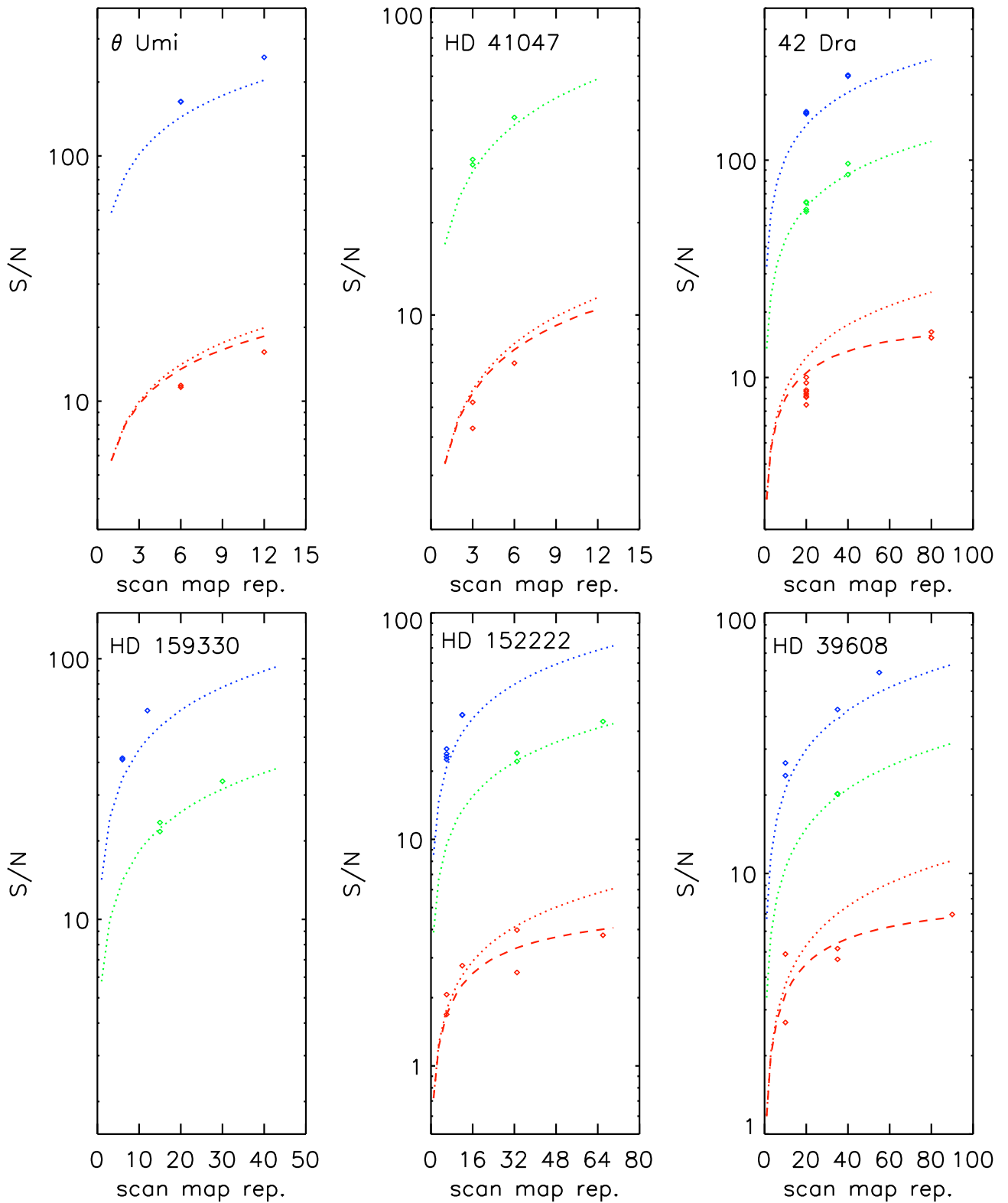


Fig. 2. continued. Measured S/Ns for mini scan map photometry depending on the number of repetitions.

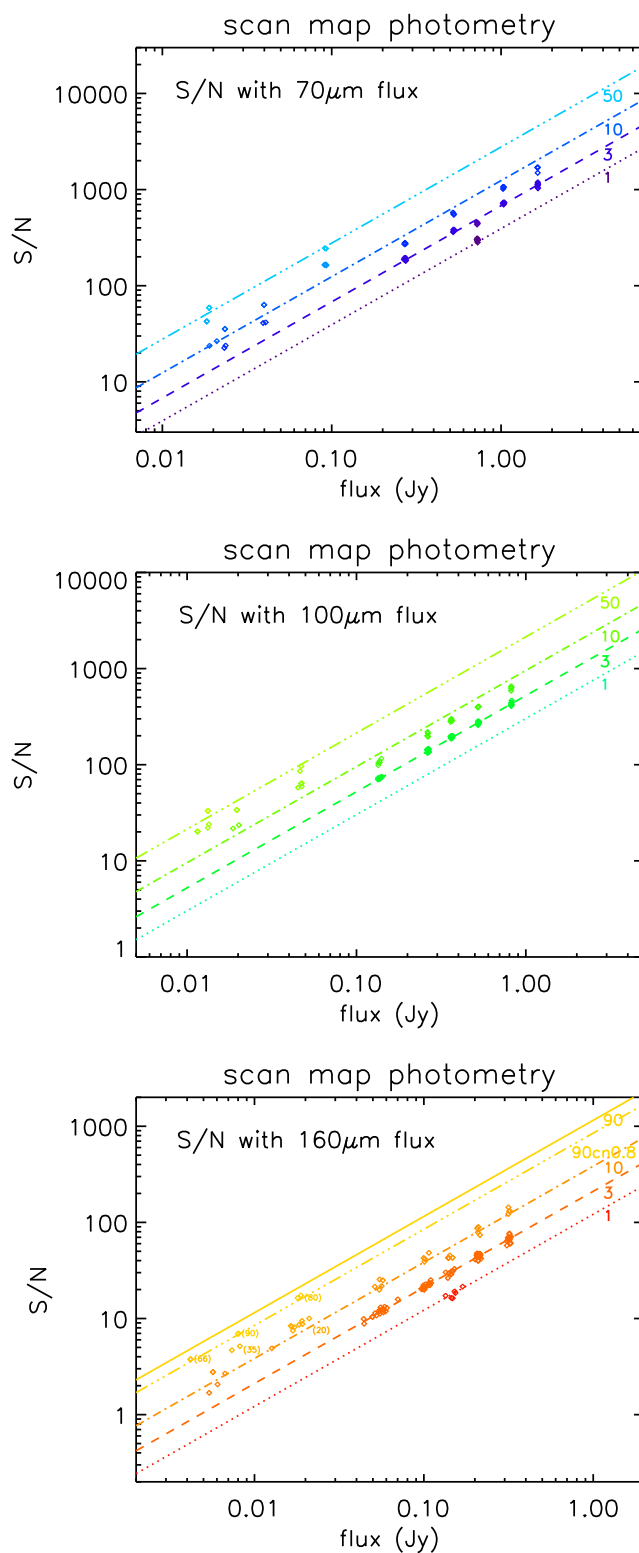


Fig. 3. Measured S/Ns for mini-scan-map photometry depending on the source flux (Note: fluxes measured inside the aperture are used here). For better comparability only measurements with an observational set-up identical with the final mini-map set-up (ten 180'' scan legs with 4'' separation and scan speed 20''/s) are considered. Lighter colour tones are measurements with higher scan map repetition factors. We note that here the dotted, dashed, and dashed dotted lines in different colour tones do not represent the S/N prediction by the PACS exposure time calculator of the *Herschel* observation planning tool HSpot, but are empirical adjustments to the average measured S/N for the respective scan map repetitions. In the 160 μ m panel, numbers in parentheses mark measurements with high repetition factors whose S/N is degraded by confusion noise. This is also indicated by two S/N with flux lines for repetition factor 90, where the lower one includes additional confusion noise (cn) of 0.8 mJy.

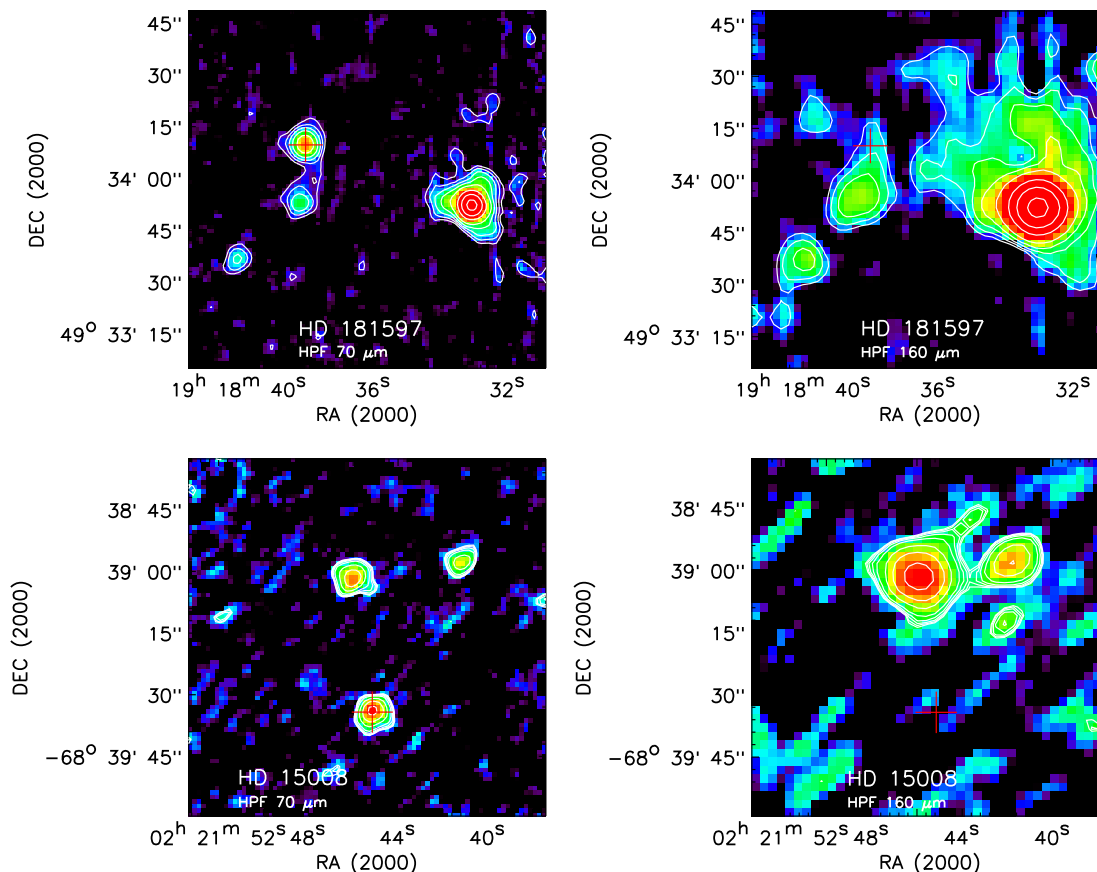


Fig. 4. Examples of detection at $70\ \mu\text{m}$ and non-detection at $160\ \mu\text{m}$. The red cross (arm length equal to $5''$) indicates the common *Herschel* position. We note that for both sources there exists only one scan map orientation which leads to some residual scan artefacts, in vertical and diagonal direction, respectively; see Table A.3 for details. Top: HD 181597, OBSID 1342185451 on OD 146. The bright point source at the right is KIC 11555225. Bottom: HD 15008 (δ Hyi), OBSID 1342189130 on OD 241.

cluster of sources around the star starts to pop up, but the star is still the dominant source inside the field. At $160\ \mu\text{m}$, all surrounding sources are brighter than the star, which appears only as an appendix of the source located north-west of it. Also the local brightness maximum is not as well located on the cross as is the case for the stellar images at 70 and $100\ \mu\text{m}$. It is therefore not possible to obtain reliable photometry for HD 159330 at $160\ \mu\text{m}$. The compactness of the surrounding sources both in the HPF and the JScanam image points to an extragalactic nature of the confusing sources. This is difficult to verify in the optical, since HD 159330 is a 6.2 mag (V band) bright star.

An example of likely cirrus confusion is shown in Fig. 6 around the star η Dra (HD 148387). There is relatively significant similarity between the HPF and JScanam processed map concerning the brighter spots and features, while on the low level there are differences, because the HPF algorithm is not designed to preserve faint extended emission. Nevertheless both maps indicate a filamentary emission around the star. Indeed, η Dra, with $l = 92.6^\circ$ and $b = +41.0^\circ$, is located at the edge of the Draco nebula (cf. e.g. Fig. 3 in Herbstmeier et al. 1998, w.r.t. its location), a pronounced cirrus cloud. The extract of the *AKARI* Wide-L ($140\ \mu\text{m}$) all sky map⁴ (Doi et al. 2015) reveals that η Dra is located at the southern edge of a cirrus knot with an extension of

it passing north-west into the PACS map area. The cirrus confusion affects the derived $160\ \mu\text{m}$ flux noticeably, as is discussed in Sect. 5.2. Other cases of suspected cirrus confusion are also discussed there.

3.8. Photometry results

Results of individual photometric measurements are given in Appendix A, Sect. A.3 in Tables A.3 to A.5. Here we report the combined aperture and colour-corrected photometry of all measurements in Table 7. This is identical with the phot_s photometry in Table A.1. The quoted uncertainties of the measurements in Table 7 include the absolute calibration uncertainty of 5%, due to the fiducial star model uncertainties, which is quadratically added to the rms of the mean flux value as quoted in Table A.1.

For 11 stars we obtain reliable photometry in all three PACS bands. There is no $70\ \mu\text{m}$ flux for HD 41047, since there are only measurements in the 100 and $160\ \mu\text{m}$ filters. There is no $160\ \mu\text{m}$ detection for HD 159330 because of confusion noise. For HD 181597 and HD 15008 we obtain reliable fluxes only at $70\ \mu\text{m}$, since there are no $100\ \mu\text{m}$ scan map measurements and at $160\ \mu\text{m}$ the stars are too faint for the applied repetition numbers. Faintest fluxes, for which the photometry has still good quality (accuracy $\leq 15\%$), are about 10 – 20 mJy.

⁴ *AKARI* Far-infrared All-Sky Survey maps query service http://www.ir.isas.jaxa.jp/AKARI/Archive/Images/FIS_AllSkyMap/search/
We use the *AKARI* WIDE-L ($140\ \mu\text{m}$) maps instead of the N160

($160\ \mu\text{m}$) maps, because the latter ones do not have sufficient S/N over the whole field for illustration of the background structure.

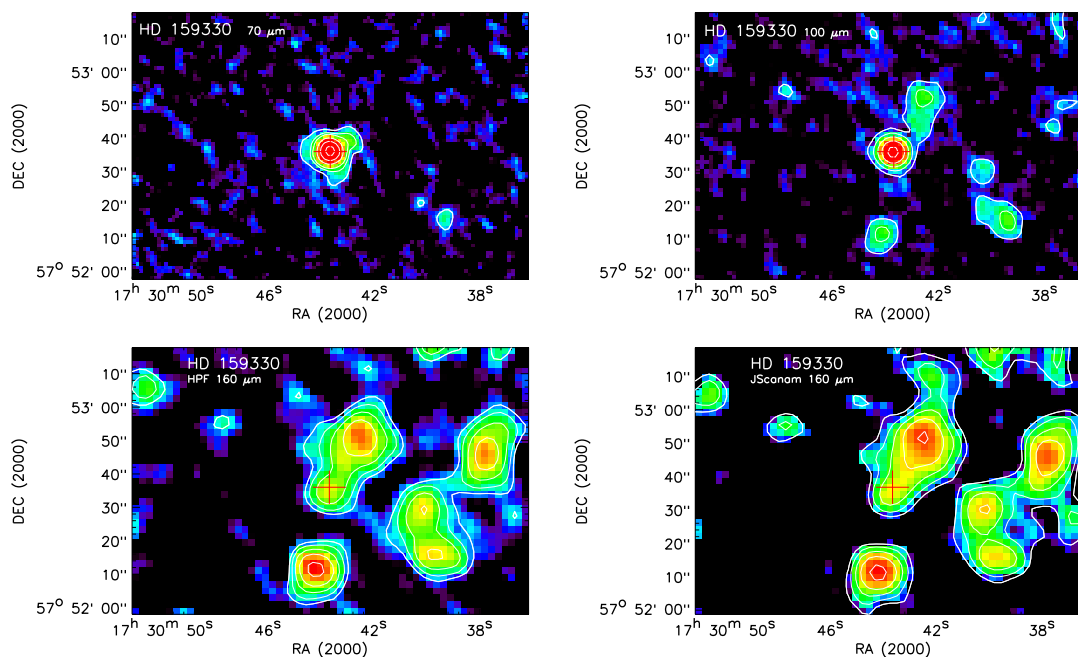


Fig. 5. Example of background confusion noise around the star HD 159330 (OBSIDs 1342213583-86 on OD 628, see Tables A.3 and A.4 for details) by comparing maps in the three filters 70, 100 and 160 μm . At 160 μm both the high-pass filtered (HPF) and the JScanam maps are shown to explore the nature of the background sources. The red cross (arm length equal to 5'') indicates the best common *Herschel* position of the star after frame centering at RA = 17:30:43.69 and DEC = +57:52:36.0.

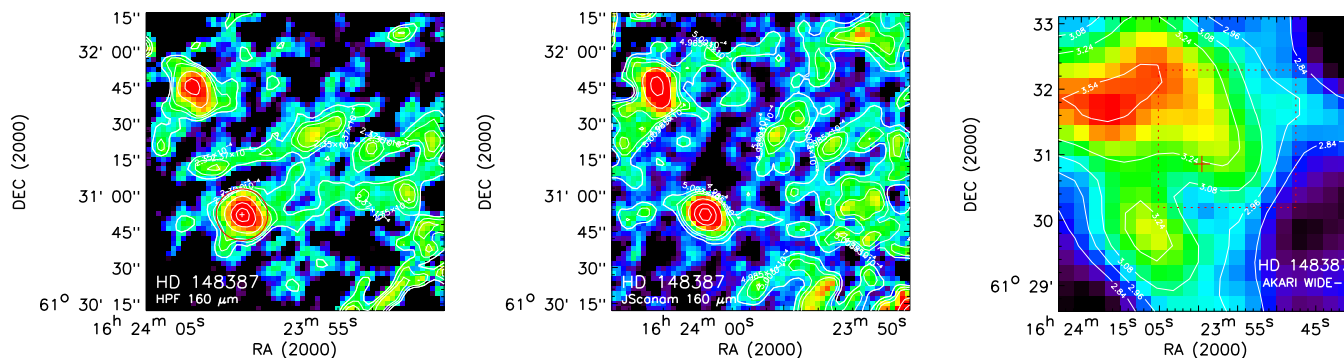


Fig. 6. Example of cirrus confusion noise around the star HD 148387 (η Dra, OBSIDs 1342186146, ..47, ..55, ..56 from OD 160). The left panel shows the high-pass filter processed map used for the photometry, the photometric aperture with 10.7 radius is indicated by the red circle and a small white cross at its centre. The middle panel shows the Jscanam processed map which reproduces extended emission more reliably. The right panel shows the *AKARI* WIDE-L (140 μm) background emission around the source (red cross), the *AKARI* map area is about four times as large as the PACS map area, which is indicated by the red dashed square.

In Appendix Section A.2, we conduct a qualitative inter-comparison of the high-pass filter (HPF) photometry with three other *Herschel* mapper softwares for HD 152222, the faintest star at 160 μm with reliable photometry in all three filters. Aspects like noise behaviour and shape of the intensity profiles are investigated and discussed. The main conclusion is that for the other mappers adapted aperture correction factors need to be established which will be determined on the basis of the high S/N fiducial standard star observational database in a forthcoming paper (Balog et al., 2018, in preparation).

The evaluation of the correspondence with the models is done in Sect. 5.

4. Chop-nod photometry

4.1. Observations

Thirteen out of the 17 sources were observed in the PACS chop-nod point source observing mode. This was the originally recommended PACS photometer observing mode for point and compact sources. This mode used the PACS chopper to move the source on-array by about 50'', corresponding to the size of about one blue/green bolometer matrix (16 pixels) or the size of about half a red matrix (8 pixels), with a chopper frequency of 1.25 Hz. The nodding was performed by a satellite movement of the same amplitude but perpendicular to the chopping direction. On each nod position the chopper executed 3 \times 25 chopper cycles. The three sets of chopper patterns were either on the same array position (no dithering) or on three different array positions (dither option). In the latter case the chopper pattern was displaced par-

Table 7. Combined mini-scan-map photometry. Model fluxes are listed in Table 1. The quoted uncertainties of the measurements include the absolute calibration uncertainty of 5%. In the case of only one observation for a specific source, the statistical error of this flux measurement is used in the uncertainty determination, and in the case of more than one observation for a source, as given in columns n_{70} , n_{100} , and n_{160} , the standard deviation of the weighted mean as given in Table A.1, column *phot_s*, is used in the uncertainty calculation.

HD	Name	n_{70}	$f_{\text{star}}(70\ \mu\text{m})$ (mJy)	$\frac{f_{\text{star}}(70\ \mu\text{m})}{f_{\text{model}}}$	n_{100}	$f_{\text{star}}(100\ \mu\text{m})$ (mJy)	$\frac{f_{\text{star}}(100\ \mu\text{m})}{f_{\text{model}}}$	n_{160}	$f_{\text{star}}(160\ \mu\text{m})$ (mJy)	$\frac{f_{\text{star}}(160\ \mu\text{m})}{f_{\text{model}}}$
62509	β Gem	8	2649±132	1.08±0.08	8	1284±64	1.08±0.08	16	497±25	1.09±0.08
12929	α Ari	8	1664±83	0.97±0.08	8	820±41	0.99±0.08	16	328±17	1.02±0.08
32887	ε Lep	8	1166±58	0.99±0.08	12	568±28	0.99±0.08	18 ^a	224±11	1.00±0.08
198542	ω Cap	8	845±42	0.99±0.08	8	413±21	0.99±0.08	16	161±8.2	0.99±0.08
148387	η Dra	8	506±25	1.06±0.06	8	250±13	1.07±0.06	16	98±7.1	1.10±0.08
180711	δ Dra	12	436±22	1.02±0.08	10	214±11	1.03±0.08	22	85±4.8	1.07±0.08
139669	θ Umi	4	284±14	0.99±0.08	2	144±8.8	1.03±0.08	2 ^b	62±4.0 ^f	1.16±0.10
41047	HR 2131		no measurement		2	97±4.9	1.01±0.08	2	36±5.9	0.97±0.17
170693	42 Dra	4	148±7.4	0.96±0.06	4	73±3.8	0.97±0.06	8	28±1.7	0.96±0.07
138265	HR 5755	4	113±5.7	0.97±0.06	6	57±2.9	0.99±0.06	5 ^c	31±1.8	1.40±0.10
159330	HR 6540	4	65±3.4	1.01±0.06	6	31±1.9	0.99±0.07	10	source confusion	
152222		4	39±2.1	0.99±0.07	2	21±1.0	1.08±0.07	4 ^d	7.4±0.9	0.99±0.13
39608		3	31±1.9	0.99±0.07	1	18±1.3	1.19±0.08	2 ^e	12±0.9	2.05±0.17
181597	HR 7341	2	29±2.5	1.04±0.09		no measurement		2	below detection limit	
15008	δ Hyi	1	22±1.6	0.96±0.08		no measurement		1	below detection limit	

(a) OBSIDs 1342205202 & 1342263904 excluded

(b) OBSIDs 1342184574, 1342184575, 1342184585, 1342184586 excluded

(c) OBSIDs 1342185446, 1342185448, 1342185447, 1342185449, 1342191986 excluded

(d) OBSIDs 1342240702, 1342240703, 1342227973 & 1342227974

(e) Only OBSIDs 1342198537 & 1342198538

(f) Due to cirrus confusion, a background subtraction uncertainty of 10% must be added: 62±7.1 mJy, see discussion in Sect. 5.2

Table 8. Combined chop-nod photometry. Model fluxes are listed in Table 1. Values in italics are uncertain. The quoted uncertainties of the measurements include the absolute calibration uncertainty of 5%. In the case of only one observation for a specific source, the statistical error of this flux measurement is used in the uncertainty determination, in case of more than one observation for a source, as given in columns n_{70} , n_{100} , and n_{160} , the standard deviation of the weighted mean from the individual chop/nod fluxes listed in Tables B.1 to B.3 is used in the uncertainty calculation.

HD	Name	n_{70}	$f_{\text{star}}(70\ \mu\text{m})$ (mJy)	$\frac{f_{\text{star}}(70\ \mu\text{m})}{f_{\text{model}}}$	n_{100}	$f_{\text{star}}(100\ \mu\text{m})$ (mJy)	$\frac{f_{\text{star}}(100\ \mu\text{m})}{f_{\text{model}}}$	n_{160}	$f_{\text{star}}(160\ \mu\text{m})$ (mJy)	$\frac{f_{\text{star}}(160\ \mu\text{m})}{f_{\text{model}}}$
62509	β Gem	1	2570±129	1.05±0.08	1	1267±65	1.07±0.08	2	497±25	1.09±0.08
32887	ε Lep	2	1181±59	1.00±0.08	2	558±31	0.97±0.08	4	205±12	0.92±0.08
148387	η Dra	1	509±31	1.06±0.07	1	236±19	1.01±0.10	2	101±10	1.13±0.10
180711	δ Dra	5	440±22	1.03±0.08	3	214±12	1.03±0.08	8	83±5.0	1.05±0.08
139669	θ Umi	10	282±14	0.98±0.08	9	142±7.9	1.02±0.08	16 ^a	55±3.8	1.02±0.09
41047	HR 2131				1	88±5.6	0.92±0.09	1	29±15	0.77±0.54
138265	HR 5755	9	113±5.7	0.97±0.06	4	59±3.0	1.04±0.06	11 ^b	31±1.9	1.39±0.07
159330	HR 6540	1	60±7.6	0.94±0.13	3	31±2.2	0.98±0.08	4	source confusion	
152222		1	39±4.9	0.98±0.14		no measurement		1	below detection limit	
181597	HR 7341	1	below detection limit			no measurement		1	below detection limit	
15008	δ Hyi	4	20±1.4	0.87±0.08	2	below detection limit		6	below detection limit	
156729	e Her		no measurement		1	below detection limit		1	below detection limit	
168009	HR 6847		no measurement		1	below detection limit		1	below detection limit	

(a) 1342184583, 1342184584 & 1342184595 excluded

(b) OBSIDs 1342185441 & 1342185442 excluded

allel to the chopper deflection by 8'' (2 $\frac{2}{3}$ blue pixels or 1 $\frac{1}{3}$ red pixels). Most of the faint star observations were performed with the dither option on; Tables B.1 to B.3 indicate for each observation the selection of the respective dither/no-dither mode.

Each chopper plateau lasted for 0.4 s (16 readouts on-board) producing four frames per plateau in the telemetry down-link. The full 3×25 chopper cycles per nod position were completed in less than 1 minute. In the case of repetition factors larger than

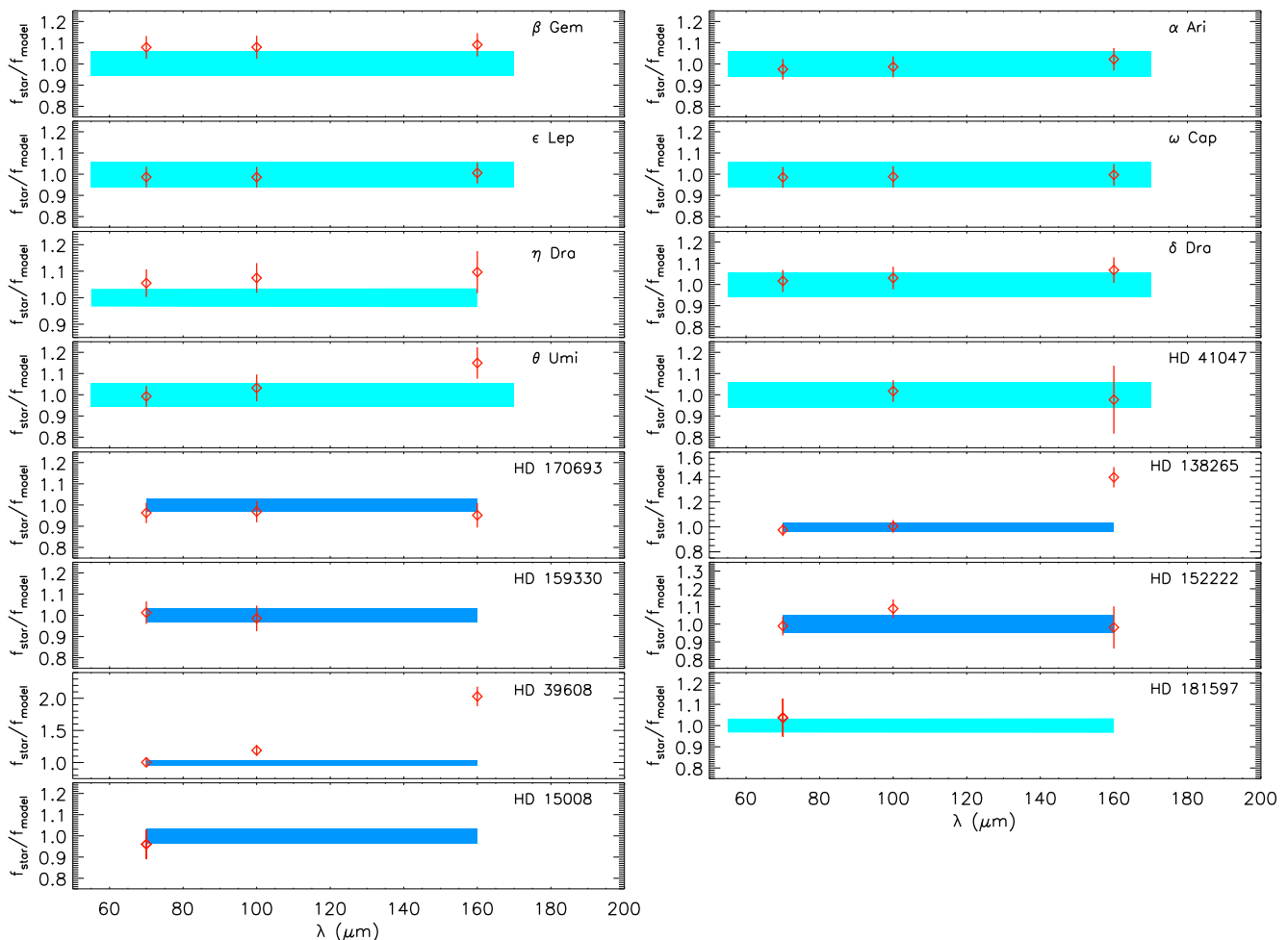


Fig. 7. Ratio of the observed and colour-corrected (cc) scan map photometry fluxes with either the photometric standard model flux or the Gordon et al. (2007) $70\mu\text{m}$ flux prediction and Rayleigh-Jeans extrapolation (red diamonds). The uncertainty of the models is shown by the light blue range, the uncertainty of the flux prediction and the Rayleigh-Jeans extrapolation by the dark blue range. The uncertainty of the flux ratio includes the absolute photometric error of the measurement.

1, in particular for our faintest targets, the nod-cycles were repeated in the following way (example for 4 repetitions): *nodA-nodB-nodB-nodA-nodA-nodB-nodB-nodA* to minimize satellite slew times. Selected repetition factors are given in Tables B.1 to B.3. We note that a repetition factor may have been optimized for the short-wave filter measurement and is hence less optimal for the $160\mu\text{m}$ filter, where the star is fainter. The observations were usually done in high gain mode, but there were a few exceptions taken for comparative performance checks.

4.2. Data analysis and calibration

The data reduction and calibration performed in HIPE (Ott 2010) followed the description in Nielbock et al. (2013). For the reduction of our faint star targets we adjusted a few aspects and used very recent software developments for PACS photometer observations (gyro correction and updated pointing products and refined focal plane geometry calibration). These new corrections are meanwhile part of the Standard Product Generation (SPG) pipelines version 13.0 and higher. For the stellar flux derivation the same procedures and parameters as for scan map photometry, and as summarized in Eq. 1 and Table 2, are applied.

The photometric uncertainty was estimated with the histogram method with a coverage threshold as described in detail

in Sect. 3.3 for the scan maps. Correlated noise is corrected for via an empirical function to obtain a conservative upper limit for the measurement uncertainties. The applied correction factors f_{corr} are 6.33, 4.22, and 7.81 for the 70 , 100 , and $160\mu\text{m}$ filters, respectively.

4.3. Photometry results

Results of individual measurements are given in Appendix B in Tables B.1 to B.3. We note that there are observations of HD 138265 on OD 146 for which the noise does not seem to scale with the number of repetitions. The reason is that for these measurements the basic length of the nod period was varied and compensated by the corresponding number of nod cycle repetitions.

Here we report the combined photometry of all measurements in Table 8. The quoted uncertainties of the measurements include the absolute calibration uncertainty of 5%, due to the fiducial star model uncertainties, which is quadratically added to the rms of the mean flux value.

For six stars we obtain reliable photometry in all three PACS bands. There is no $70\mu\text{m}$ flux for HD 41047, since there are only measurements in the 100 and $160\mu\text{m}$ filters. There is no $160\mu\text{m}$ detection for HD 159330 because of confusion noise.

Table 9. Evaluation of correspondence of PACS photometry with models or flux predictions (C = Cohen, H = Hammersley, G = Gordon). Column "mode" specifies the PACS observing mode (s = scan map, c = chop/nod). Column "Reason for deviation" gives a short summary of the discussion in the reference sections.

HD	Other name	Model	Mode	Correspondence with model	Reason for deviation	Sect.
62509	β Gem	C	s,c	no, excess of $\approx +8\%$	dust disk in planetary system	5.2.1
12929	α Ari	C	s	yes, better than $\pm 3\%$		
32887	ε Lep	C	s,c	yes, better than $\pm 1\%$		
198542	ω Cap	C	s	yes, better than $\pm 1\%$		
148387	η Dra	H	s,c	no, excess of $\approx +8\%$	dust in binary system	5.2.1
180711	δ Dra	C	s,c	partially, $\approx +3\%$ offset for $\lambda \leq 100 \mu\text{m}$ $+7\%$ @ $160 \mu\text{m}$	cirrus confusion	5.2.2
139669	θ Umi	C	s,c	partially, $\approx +3\%$ offset for $\lambda \leq 100 \mu\text{m}$ $+16\%$ @ $160 \mu\text{m}$	cirrus confusion	5.2.2
41047	HR 2131	C	s,c	yes, better than $\pm 3\%$		
170693	42 Dra	G	s	yes, $\approx -4\%$ offset		
138265	HR 5755	G	s,c	partially, $\approx -2\%$ offset for $\lambda \leq 100 \mu\text{m}$ $+40\%$ @ $160 \mu\text{m}$	cirrus confusion	5.2.2
159330	HR 6540	G	s,c	partially, better than $\pm 1\%$ for $\lambda \leq 100 \mu\text{m}$ no flux determination @ $160 \mu\text{m}$	source confusion	3.7
152222	SAO 17226	G	s,c	yes, better than $\pm 5\%$		
39608	SAO 249364	G	s	yes, better than 1% @ $70 \mu\text{m}$ $+19\%$ @ $100 \mu\text{m}$, $+105\%$ @ $160 \mu\text{m}$	background confusion	5.2.2
181597	HR 7341	H	s,c	yes, better than 4% @ $70 \mu\text{m}$ no flux determination @ $160 \mu\text{m}$	below detection limit	3.6
15008	δ Hyi	G	s,c	yes, better than 4% @ $70 \mu\text{m}$ no flux determination @ $160 \mu\text{m}$	below detection limit	3.6
156729	e Her	H	c	no	below detection limit	
168009	HR 6847	H	c	no	below detection limit	

For HD 15008 we only obtain a reliable flux at $70 \mu\text{m}$, since at 100 and $160 \mu\text{m}$ the star is too faint for the applied repetition numbers. HD 181597, HD 156729 and HD 168009 have non-detections despite a high repetition factor of 50. The non-detection is likely due to a not-yet-perfect knowledge of the optimum observing strategy early in the mission (the observations were Astronomical Observation Template (AOT) test cases). Faintest fluxes, for which the photometry has still good quality (accuracy $\leq 15\%$), are approximately 30 mJy .

In Appendix C we conduct a detailed comparison between the chop/nod and scan map stellar photometry. In summary the results are very consistent and confirm each other. A few cases with larger discrepancy are due to only a small number of measurements or low S/N in chop/nod mode.

5. Comparison with model fluxes or flux predictions

5.1. Overview of findings

Since all detected stars are observed in scan map mode and we have more and better S/N measurements in this mode, we restrict the following inter-comparison with the models to scan map photometry. For each star a quantitative comparison per filter is given in Table 7. Figure 7 shows a graphical comparison of the measured fluxes with the model and Table 9 provides a summary of the correspondence evaluation.

We find an excellent correspondence with the model or flux prediction over the full PACS wavelength range for α Ari, ε Lep, ω Cap, HD 41047, 42 Dra and HD 152222. We find a partial correspondence up to $100 \mu\text{m}$ for δ Dra, θ Umi, HD 138265 and HD 159330, while the $160 \mu\text{m}$ flux exceeds the model flux or, as in the latter case, cannot be determined due to confusion by nearby sources. For HD 39608, the $70 \mu\text{m}$ flux still corresponds

excellently with the flux prediction, but at 100 and $160 \mu\text{m}$ a noticeable flux excess is discovered. β Gem and η Dra both exhibit a significant offset above the model for all wavelengths. For HD 181597 and HD 15008 we can prove a good correspondence at $70 \mu\text{m}$, but have no means to do so at longer wavelengths, since our measurements are not above the detection limit.

We discuss now the origin of the excess emission for δ Dra, θ Umi, HD 138265, HD 39608, β Gem and η Dra.

5.2. Stars with FIR excess

A FIR excess can be an intrinsic source property or be caused by confusing background sources, as already addressed in Sect. 3.7. Cohen et al. (2005) and Dehaes et al. (2011) discuss possible chromospheric emission or thermal emission from an ionized wind which gives noticeable excess at sub-mm wavelengths, but may already set in at FIR wavelengths, as intrinsic emission mechanisms. Groenewegen (2012) investigated the phenomenon of infrared excess around red giant branch stars assuming mass loss arising from chromospheric activity.

One other aspect to consider in this context is possible source variability; we investigate this for the case of β Gem: The Cohen et al. (1996) FIR model SED is an extension of an absolutely calibrated $1.2 - 35 \mu\text{m}$ model⁵ Cohen et al. (1995). In Fig. 8 we show both model parts represented by the orange and red lines. No inconsistency between both parts can be recognised. Besides the PACS photometry we show the colour-corrected *IRAS* FSC (Moshir et al. 1989) and *SPIRE* PSC⁶ (Schulz et al. 2017)

⁵ http://general-tools.cosmos.esa.int/iso/users/expl_lib/ISO/wwwcal/isyoprep/cohen/composites/

photometry spanning the wavelength range from 12 to 500 μm . All measured photometry was taken between 1983 and 2009 – 2013 and is clearly above the model, meaning that variability of the source is an unlikely explanation, since a major part of the photometric input for the Cohen model was obtained in-between (but *IRAS* 12 and 25 μm photometry was not considered).

Another explanation for an intrinsic FIR excess can be a residual dust disk from a stellar- or planetary-system-formation process. One of the first giant stars, for which an infrared excess was reported, is the K3 giant δ And (Judge et al. 1987). The giant is the brightest star in a triple or quadruple system and is itself a spectroscopic binary with a companion that is most likely a main sequence K-type star (Bottom et al. 2015). Judge et al. (1987) argued that the infrared excess appears to be caused by a detached primordial dust shell around the giant. Plets et al. (1997) concluded for a larger sample of giants with infrared excess, that this phenomenon is most likely related to the Vega phenomenon around first-ascent giants.

5.2.1. Intrinsic FIR excess

β Gem is another good candidate for having a residual debris disk, since it is the host star of a confirmed (Hatzes et al. 2006) Jupiter-sized planet (HD 62509 b, $M = 2.9 \pm 0.1 M_J$, $a = 1.69 \pm 0.03 \text{ AU}$). A rough estimate (assuming a Jupiter diameter and $T = 300 \text{ K}$) gives a contrast of $> 10^5$ between star and planet, meaning that the planet cannot account for the FIR excess of $\approx 8\%$.

The Cohen models of β Gem are based on $T_{\text{eff}} \approx 4850 \text{ K}$ (see file headers of models with reference to Blackwell et al. (1991)). The effective temperature T_{eff} of giant stars are determined in the ultraviolet to near-infrared wavelength range, either from photometric indices (e.g. Lyubimkov & Poklad 2014), colours and metallicities (e.g. Alonso et al. 1999), or integrated fluxes and interferometric measurements of the stellar diameters (e.g. Dyck et al. 1996). Other references give $T_{\text{eff}} = 4850 \text{ K}$ (Gray et al. 2003) and $4946 \pm 18 \text{ K}$ (Jofré et al. 2015) and thus confirm the value used by Cohen. We have scaled a continuum model⁸ of the PACS fiducial standard star α Boo, a K2III star, by calculating the Selby et al. (1988) K_n narrow band photometry ratio $10^{-0.4 \cdot (-1.14 - (-3.07))} = 0.169$. The intention here is not to accurately model the β Gem FIR photometry, but to demonstrate that the SED of the cooler source with $T_{\text{eff}} = 4320 \text{ K}$ provides a better fit. This indicates that there is an additional cooler FIR component beside the photospheric emission of the star. The shape of the SED $> 10 \mu\text{m}$ given by the *IRAS*, PACS, and SPIRE photometry argues for a flat blackbody dust disk (see e.g. Chiang & Goldreich 1997; Beckwith 1999, for a discussion of the dust disk SED shape depending on its geometry).

α Ari and 42 Dra are also host stars of confirmed Jupiter-sized planets (alf Ari b, $M = 1.8 \pm 0.2 M_J$, $a = 1.2 \text{ AU}$ (Lee et al. 2011)⁹; 42 Dra b, $M = 3.88 \pm 0.85 M_J$, $a = 1.19 \text{ AU}$ (Döllinger et al. 2009)¹⁰), but for these stars any possible debris disk emis-

photometry & models for β Gem

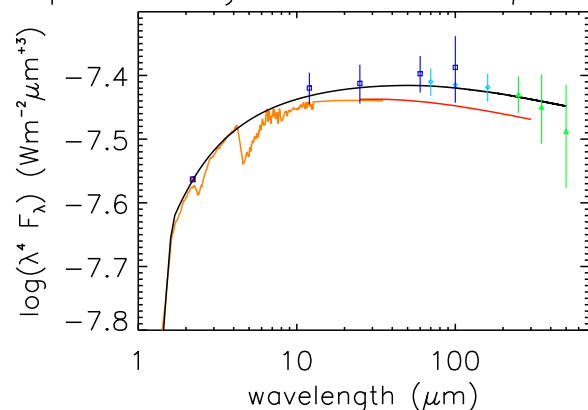


Fig. 8. Investigation of the discrepancy of the β Gem Cohen et al. (1996) model and measured FIR photometry. For a better zoom-in over a large wavelength range, $\log_{10}(\lambda^4 \cdot f_\lambda)$ is displayed. The orange and red lines are the Cohen et al. (1995) absolutely calibrated 1.2 – 35 μm spectral model and the Cohen et al. (1996) FIR extension, respectively. The black line represents a scaled ($\times 0.169$) fiducial star continuum model of α Boo (Dehaes et al. 2011). The scaling factor has been derived from the Selby et al. (1988) K_n narrow band photometry ratio $10^{-0.4 \cdot (-1.14 + 3.07)}$ and the position of the scaling wavelength (2.205 μm) is indicated by the violet square symbol. We note that the K_n zero point is $\approx 3\%$ higher than that for the Cohen models (cf. file header of α Boo model (reference, see text) vs. Table 1 in Cohen et al. (1992)). Dark-blue squares, light-blue diamonds and green triangles represent *IRAS* FSC, PACS and SPIRE photometry and their respective uncertainties. This photometry has been colour-corrected for a 4500 K blackbody spectrum.

sion is much fainter than for β Gem. The observed SED shape of α Ari is a little bit shallower than the model prediction (cf. Table 7), but the measurement and model uncertainties do not allow any detection. For 42 Dra, no deviation from a pure photospheric emission SED can be found from our photometry. We therefore keep both stars in our standard star list.

In Sect. 3.7 we have shown the 160 μm map of η Dra (Fig. 6) as a representative example for cirrus confusion. Indeed, from Table 10, $\frac{f_{160,\text{corr}}^{10''7}}{f_{160,\text{corr}}^{5''35}} = 1.17$, which could fully explain $\frac{f_{160}}{f_{\text{model}}} = 1.16$ in Table 7 as an excess due to cirrus emission in the standard 10''7-radius aperture. On the other hand, from Fig. 7, we see that already the 70 and 100 μm fluxes are off by +6 and +7%, respectively, with regard to the model. We investigate this discrepancy in Fig. 9 by complementing the PACS photometry with additional *IRAS* FSC (Moshir et al. 1989) photometry and ISOPHOT (Lemke et al. 1996) HPDP (Highly Processed Data Products photometry (c.f. Appendix. D, Table D.1)). It is obvious that all photometric measurements are consistently above the model, irrespective of whether the observations were obtained during the *IRAS*, *ISO*, or *Herschel* missions (1983 – 2013). The excess is a clear hint of an additional emission component besides the photospheric emission of the star, whereby the rise in flux beyond 100 μm is likely caused by cirrus emission. The G8 giant η Dra (also identified as CCDM J16239+6130 A) has a K1V companion, CCDM J16239+6130 B (Dommangen & Nys 2002), at a distance of 2''5 and at a position angle of 71.6° NE. The origin of the excess emission could then be dust inside this binary system.

⁶ [http://irsa.ipac.caltech.edu/cgi-bin/Gator/nph-scan?submit=Select&projshort=HERSCHEL](http://irsa.ipac.caltech.edu/cgi-bin/Gator/nph-scan?submit=Select&projshort=HERSCHEL;); for SPIRE colour correction, see SPIRE Handbook, Table 5.7 http://herschel.esac.esa.int/Docs/SPIRE/spire_handbook.pdf

⁷ The Extrasolar Planet Encyclopedia http://exoplanet.eu/catalog/HD_62509_b/

⁸ This model can be found under <http://archives.esac.esa.int/hsa/legacy/ADP/StellarModels/>

⁹ The Extrasolar Planet Encyclopedia http://exoplanet.eu/catalog/alf_Ari_b/

¹⁰ http://exoplanet.eu/catalog/42_Dra_b/

Table 10. Input data for the investigation of $160\mu\text{m}$ photometric flux contamination of faint stars by background confusion. The determination of B_{160}^{ISM} is described in the text. The OBSID combinations of the deepest maps are used for this investigation. $f_{160,\text{excess}}$ is estimated as the difference of the measured f_{160} minus model f_{model} flux from Table 7. Listed fluxes $f_{160,\text{corr}}^{\text{aperture radius}}$ are not colour corrected. Uncertainties of the flux estimates include a 1% uncertainty of the aperture correction to obtain the total flux, which is quadratically added to σ_{aper} (c.f. Eq. 2).

HD	l	b	B_{160}^{ISM}	OBSIDs	$f_{160,\text{excess}}$	$f_{160,\text{corr}}^{5''/35}$	$f_{160,\text{corr}}^{10''/7}$	$f_{160,\text{corr}}^{14''/0}$	$\frac{f_{160,\text{corr}}^{10''/7}}{f_{160,\text{corr}}^{5''/35}}$
	($^{\circ}$)	($^{\circ}$)	(MJy sr^{-1})		(mJy)	(mJy)	(mJy)	(mJy)	
148387	92.6	+41.0	2.44 ± 0.13	1342186146+..47+..55+..56	8.5	106.7 ± 1.4	124.9 ± 2.1	130.7 ± 2.6	1.17
180711	98.7	+23.0	6.04 ± 0.02	1342212497+.498+.499+.500 1342222147+..48+..49+..50 1342233571+..72+..73+..74 1342250093+..94+..95+..96 1342257987+..88+..89+..90	5.5	87.4 ± 0.9 90.8 ± 1.0 92.0 ± 1.0 87.2 ± 0.9 86.2 ± 0.9	91.8 ± 1.1 94.4 ± 1.1 95.9 ± 1.1 85.9 ± 1.0 91.4 ± 1.1	94.8 ± 1.2 95.3 ± 1.3 99.0 ± 1.2 84.2 ± 1.1 95.2 ± 1.3	1.05 1.04 1.04 0.99 1.06
139669	112.9	+36.5	2.67 ± 0.07	1342191982+..83	8.0	61.3 ± 0.7	66.5 ± 0.9	68.4 ± 1.0	1.08
138265	95.8	+47.4	1.27 ± 0.03	1342188841+42	9.0	30.1 ± 0.4	33.3 ± 0.5	34.9 ± 0.6	1.11
39608	269.6	-30.9	5.22 ± 0.17	1342198535+..36+..37+..38	6.0	10.7 ± 0.2	13.5 ± 0.3	15.9 ± 0.4	1.26
152222	98.5	+36.7	2.57 ± 0.15	1342227973+..74	–	8.2 ± 0.2	7.0 ± 0.3	5.9 ± 0.4	0.85

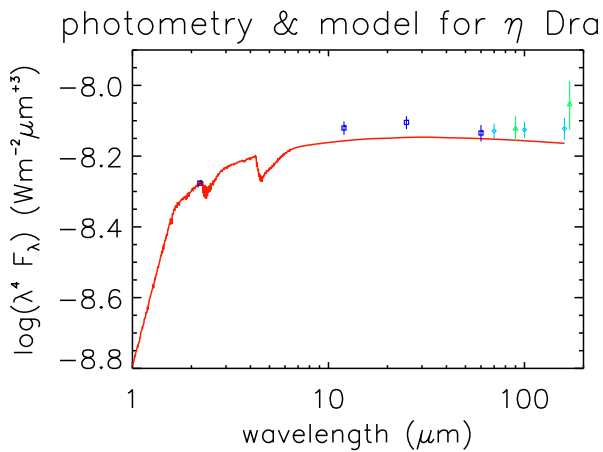


Fig. 9. Investigation of the discrepancy of the η Dra Hammersley et al. (1998) model and measured FIR photometry. For a better zoom-in over a large wavelength range, $\log_{10}(\lambda^4 \cdot f_{\lambda})$ is displayed. The red line is the model, absolutely calibrated at $2.208\mu\text{m}$ (K_n magnitude = 0.62 ± 0.005 mag, c.f. Cohen et al. (1999), Selby et al. (1988)) as represented by the violet square symbol. Dark-blue squares, light-blue diamonds, and green triangles represent *IRAS* FSC, PACS, and ISOPHOT HPDP photometry and their respective uncertainties. This photometry has been colour-corrected for a 5000 K blackbody spectrum.

5.2.2. FIR background confusion

In Table 10 we have compiled crucial information for those sources whose $160\mu\text{m}$ fluxes may be contaminated by background confusion. All sources are at relatively high galactic latitudes in the range $23^{\circ} \leq |b| \leq 47^{\circ}$. The $160\mu\text{m}$ brightness of the ISM, B_{160}^{ISM} , was derived from *AKARI*-FIS WIDE-L ($140\mu\text{m}$) all-sky survey maps⁴ (Doi et al. 2015) in the following way:

$$B_{160}^{ISM} = \frac{B_{\text{WIDE-L}}^{\text{AKARI}} - B_{\text{CFIRB}}^{CC_{\nu^0}}}{CC_{\nu^{1.5}}^{BB(T=20K)} K_{\nu^{1.5}}^{FIS\ 140-PACS\ 160}}, \quad (8)$$

with $B_{\text{WIDE-L}}^{\text{AKARI}}$ being the measured *AKARI* $140\mu\text{m}$ flux (we highlight that we have transformed the original $6\text{ deg} \times 6\text{ deg}$ maps in ecliptic coordinates to the equatorial coordinate system and centred to the central coordinates of the PACS maps), $B_{\text{CFIRB}} =$

1.08 MJy/sr being the cosmic far-infrared background level (cf. Juvela et al. 2009), $cc_{\nu^0} = 0.964$ and $cc_{\nu^{1.5}}^{BB(T=20K)} = 0.95$ are *AKARI*-FIS WIDE-L colour-correction factors (Shirahata et al. 2009) for the indexed SEDs and $K_{\nu^{1.5}}^{FIS\ 140-PACS\ 160} = 0.954$ is the reference wavelength-correction factor between *AKARI*-FIS WIDE-L and the PACS $160\mu\text{m}$ filter (Müller et al. 2011) for the modified blackbody SED $\nu^{1.5} BB(T=20\text{ K})$, which is typical for IR cirrus emission according to latest results (Planck Collaboration et al. 2014; Bianchi et al. 2017). The listed surface brightness of B_{160}^{ISM} is associated with the $15'' \times 15''$ pixel covering the star position, the uncertainty was computed as the standard deviation of the eight neighboring pixel values with regard to the central one. B_{160}^{ISM} are between 1.3 and 6.0 MJy sr^{-1} , with a gradient with $|b|$.

Kiss et al. (2005) parameterized the sky confusion noise (1σ) for FIR measurements with ISOPHOT depending on wavelength and background reference configuration geometry as

$$\frac{N_{\text{conf}}^{\text{PHT}}(\theta, k, \lambda)}{1\text{ mJy}} = C_0(\theta, k, \lambda) + C_1(\theta, k, \lambda) \left(\frac{B(\lambda) - B_{\text{CFIRB}}(\lambda)}{1\text{ MJy sr}^{-1}} \right)^{\eta(\theta, k, \lambda)}. \quad (9)$$

The ISOPHOT C200 measurement configuration P/C/184'' in Table 4 of Kiss et al. (2005) is closest to our PACS mini-scan-map measurement configuration, except that aperture size and background ring radius have to be scaled down by a factor of ≈ 0.22 ($92''$ ISOPHOT C200 pixel size vs. $19''$ PACS "pixel" size corresponding to a circular aperture with $10''/7$ radius and $184''$ vs. $40''$ background ring radius). This means that the PACS sky confusion noise, $N_{\text{conf}}^{\text{PACS}}$, has to be scaled down by a factor of $0.22^{2.5}$ (Kiss et al. 2005) due to the better spatial resolution of PACS. For computation of a point-source representative sky confusion noise we multiply with the aperture correction factor $c_{\text{aper}}(160\mu\text{m}) = 1.56$.

$$\frac{N_{\text{conf,PS}}^{\text{PACS}}}{1\text{ mJy}} = 3.54 \cdot 10^{-2} \times [C_0 + C_1 \left(\frac{B(\lambda) - B_{\text{CFIRB}}(\lambda)}{1\text{ MJy sr}^{-1}} \right)^{\eta}]. \quad (10)$$

Applied parameters are $C_0 = 9.3\pm 6.7\text{ mJy}$, $C_1 = 3.37\pm 1.01\text{ mJy}$, and $\eta = 1.46\pm 0.17$.

The C_0 term represents the confusion noise due to cosmic infrared background fluctuations and amounts to $0.33\pm 0.24\text{ mJy}$. Berta et al. (2011) give a confusion noise $\sigma_c = 0.92\text{ mJy}$ from

cosmological fields in the *Herschel*-PEP survey (obtained for $q = \frac{f_{\text{lim}}}{\sigma_c} = 5$), which corresponds to a C_0 value equal to 26.0 mJy.

The $C_1 (B_{160}^{ISM})^\eta$ term represents the cirrus confusion noise, which depends on the surface brightness of the emitting cirrus material. With the range $1.3 \leq B_{160}^{ISM} \leq 6.0$ MJy sr⁻¹, we predict a cirrus confusion noise $0.18 \pm 0.06 \leq N_{\text{circonf,PS}}^{\text{PACS}} \leq 1.63 \pm 1.02$ mJy.

If we attribute the 160 μm excess $f_{160,\text{excess}}$ in Table 10 fully to sky confusion and compare with our confusion noise prediction, we note the following: For our small sample of 160 μm excess stars we do not see any dependence on B_{160}^{ISM} , in particular for HD 138265 with the lowest $B_{160}^{ISM} = 1.27$ MJy sr⁻¹, the highest $f_{160,\text{excess}} = 9$ mJy is found; and the 1σ sky confusion noise derived via Eq. 10 underestimates the actually measured noise by factors 3 – 25 (1.9 – 21 accounting for the maximum positive uncertainty).

The confusion noise predictions are average numbers based on a statistical analysis. Peaks and depressions in the sky noise can significantly deviate from the average. The spatial resolution of the *AKARI* 140 μm all-sky survey maps is $\approx 88''$ (Takita et al. 2015). The PACS maps reveal much finer structures. Their weight to the noise is much higher than to the average surface brightness. Therefore, calculating the cirrus noise from the surface brightness of a larger area will always underestimate the local cirrus noise. Another possibility is that the PSF of a discrete few-mJy source coincides - accidentally to a large percentage - with the PSF of the star. Differential number counts in cosmological fields, as in Fig. 7 of Berta et al. (2011), suggest that there are 9.2×10^3 background sources/deg² for $f_{\text{lim}} \geq 3.5$ mJy, which gives 0.25 sources per photometric aperture of $10''.7$, hence an already high likelihood that such a source can blend the photometry of our faint stars. We cannot exclude either that in some maps some amount of the 160 μm excess is produced by the data reduction scheme itself by reducing the background level in some of the background reference areas (this can vary from map to map depending on the actual detector drift behaviour along the time-line and the level of reduction).

To some extent a contribution by an underlying source can be disentangled via multi-aperture photometry which includes aperture sizes as small as the PSF FWHM. From multi-aperture photometry of the deepest maps (OBSIDs combinations are indicated in Table 10) with aperture radii $5''.35$, $10''.7$ (the default one for our photometric analysis), and $14''.0$, we see that the flux increase is usually greater than the associated uncertainties, which is a hint of flux contribution by another source. As a reference, we also include the multi-aperture photometry of HD 152222 which does not show any flux increase (rather a flux decrease due to increasing uncertainties in the background subtraction with larger aperture size).

In Fig. 10 we investigate the nature of the 160 μm sky background structure, both on an absolute level and larger scale with the help of the *AKARI*-FIS WIDE-L (140 μm) all-sky survey maps⁴ (Doi et al. 2015) and on the PACS scale by parallel JScanam processing of the maps which tends to preserve more reliably small-scale structured extended emission, while the larger-scale background is subtracted. In the following, we discuss the sources δ Dra, θ Umi, HD 138265, HD 39608 and HD 152222 individually with regard to level and nature of their background confusion.

For δ Dra the scan map photometry in Table 10 gives on average $\frac{f_{160,\text{corr}}^{10''.7}}{f_{160,\text{corr}}^{5''.35}} = 1.04$, which is relatively consistent with $\frac{f_{160}}{f_{\text{model}}} = 1.07$ in Table 7, given that also the 70 and 100 μm fluxes are 2 – 3% above the model. The *AKARI*-map in Fig. 10 shows that

the source is located at the wing of a cirrus knot. The JScanam map reveals filamentary structure around the source, which indicates that the small excess in the order of 4% is likely by IR cirrus contamination. One out of the five cases investigated in Table 10 does not indicate any excess and the measured $10''.7$ aperture flux is close to the model flux. This is an example of the ability of the scan map orientation to influence the structure of the source environment due to the high-pass filter running along the scan direction.

For θ Umi the scan map photometry gives $\frac{f_{160,\text{corr}}^{10''.7}}{f_{160,\text{corr}}^{5''.35}} = 1.08$,

which is relatively consistent with $\frac{f_{160}}{f_{\text{model}}} = 1.13$ in Table 7, meaning that the 160 μm photometry in the small aperture is quite close to the model flux. The *AKARI*-map in Fig. 10 shows that the source is located on a cirrus filament. The JScanam map reveals filamentary structure, too, coinciding in direction with the *AKARI*-map feature, which supports that the excess found for the default photometric aperture of $10''.7$ is fully accounted for by IR cirrus contamination.

HD 138265 exhibits a noticeable FIR excess at 160 μm only, which makes it a potential background-contaminated source, too. The *AKARI*-map in Fig. 10 shows that it is located on the wing of a small faint cirrus knot. The JScanam processed map indicates filamentary knotty structure mostly east, south, and west of the source, which fits to its location on the knot. The morphology of the filamentary structure resembles cirrus emission rather than compact sources. We derive $\frac{f_{160,\text{corr}}^{10''.7}}{f_{160,\text{corr}}^{5''.35}} = 1.11$, which only partially explains $\frac{f_{160}}{f_{\text{model}}} = 1.36$. In this case the background contribution may be more centered in the beam, meaning that it cannot be fully separated by the multi-aperture method.

HD 39608 shows the by far strongest 160 μm excess, with $\frac{f_{160}}{f_{\text{model}}} = 2.20$. Our multi-aperture photometry gives only $\frac{f_{160,\text{corr}}^{10''.7}}{f_{160,\text{corr}}^{5''.35}} = 1.26$. The *AKARI*-map in Fig. 10 shows that it is located on the wings of two brighter cirrus knots with a depression south of it. The JScanam map reveals that there is extended filamentary structure mainly north of the source, in agreement with the larger-scale feature of the *AKARI*-map. This also affects the area where the background is determined. Given that the source is one of the faintest in our sample, with an expected photospheric flux of only about 6 mJy, any inaccuracy in the background determination has a severe impact on the resulting source flux. Furthermore, the source looks elongated in the north-south direction, which indicates contaminating emission inside the measurement aperture. From Fig. 7, we see that there is already a noticeable excess of 19% at 100 μm . Unfortunately we cannot investigate this properly on a JScanam processed map, since there exists only one map in one scan direction (the cross-scan map was erroneously executed in the 70 μm filter). HD 39608 has the second strongest ISM sky background B_{160}^{ISM} (c.f. Table 10), meaning that it is very likely that already at 100 μm there can be significant sky background contamination. The deep combined 70 μm map shows an elongated emission feature underneath the source, too.

For comparison we also show the environment of HD 152222 in Fig. 10, which is only slightly brighter than HD 39608. The *AKARI*-map shows that it is located outside a cirrus ridge close to a depression in the cirrus emission. The JScanam map reveals that the area around it is also crowded, but the sources are discrete compact sources, which argues for an extragalactic nature, and besides the star itself appears isolated inside the measurement aperture. The derived flux is quite consistent with

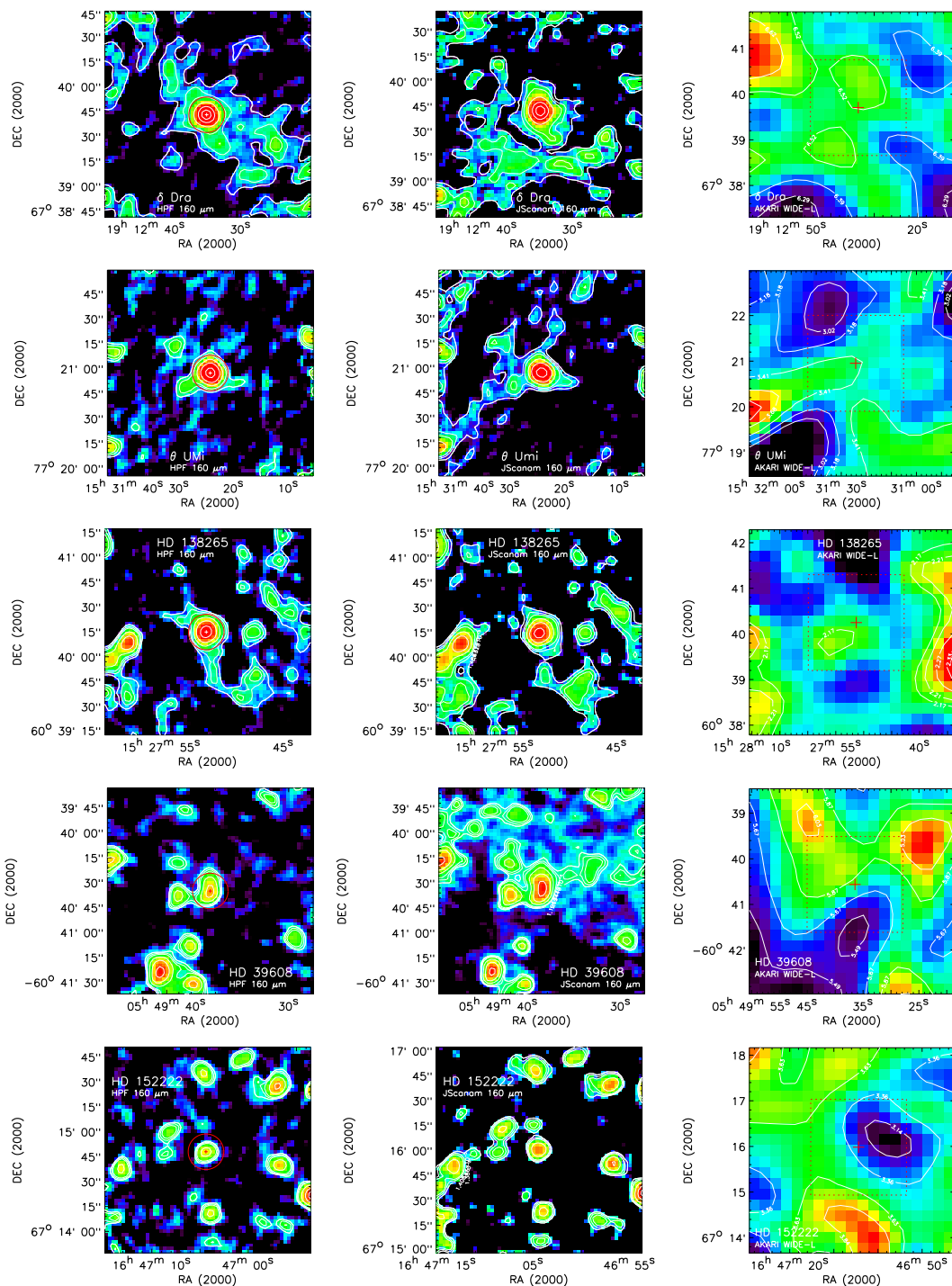


Fig. 10. Investigation of the $160\mu\text{m}$ sky background structure around the sources δ Dra (OD 934), θ UMi (OD 160), HD 138265 (OD 233), HD 39608 (OD 400) and HD 152222 (OD 843) from top to bottom. The deepest available maps were used, see Table 10 for the OBSID combination and Table A.5 for the observation details. The left panel shows the high-pass filter processed map used for the photometry, the photometric aperture with $10\prime.7$ radius is indicated by the red circle and a small red or white cross in its centre. The middle panel shows the JScanom processed map which should reproduce extended emission more reliably. The JScanom map of δ Dra shows the superposition of all five sets of OBSIDs in Table 10 (ODs 607, 751, 934, 1198 and 1328) as the deepest image of this field. The right panel shows the AKARI WIDE-L ($140\mu\text{m}$) background emission around the source (red cross), the AKARI map area is about four times as large as the PACS map area, which is indicated by the red dashed square.

the model flux which argues against a systematic background underestimate in this source flux range.

HD 39608 is hence no longer qualified as a potential calibration standard. θ UMi and HD 138265 can be considered as suitable standards up to $100\mu\text{m}$.

6. Establishment of new faint FIR primary standards

Primary flux standards are used for absolute flux calibration. Their SED is assumed to be known and stable or predictable. Absolute calibration of these sources is achieved either by a di-

Table 11. K-band and PACS 100 μm photometry and a selection of stellar parameter information for the PACS fiducial primary standards (status: "f") and PACS faint star primary standard candidates (status: "c") with nearly identical spectral type. Fiducial primary standards and related candidates are grouped together. V-band photometry is given for completeness and for the conversion of the K magnitude between the (Selby et al. 1988) K_n narrow band photometric system and the Johnson K-band photometric system.

Name	Status	SpType	V (mag)	K (mag)	K_n^{p3} (mag)	$K_{s,2MASS}^{p4}$ (mag)	f_{100}^{p5} (mJy)	T_{eff} (K)	Θ_d m''
α Boo	f	K2III	-0.04		-3.07 \pm 0.01		7509 \pm 375	4320 \pm 140 ^{s1}	20.74 \pm 0.10 ^{s1}
α Ari	c	K1IIIb	2.01	-0.63 \pm 0.03 ^{p1}			820 \pm 41	4636 \pm 13 ^{s2}	6.90 \pm 0.07 ^{s5}
42 Dra	c	K1.5III	4.82	1.95 \pm 0.05 ^{p2}			73.1 \pm 3.8	4446 \pm 12 ^{s2}	2.03 \pm 0.03 ^{s5}
HD 159330 ^l	c	K2III	6.21			2.787 \pm 0.206	31.0 \pm 1.9		
HD 152222	c	K2III	7.03			3.654 \pm 0.238	20.8 \pm 1.0		
α Tau	f	K5III	0.85		-2.94 \pm 0.01		6909 \pm 345	3850 \pm 140 ^{s1}	20.89 \pm 0.10 ^{s1}
γ Dra	f	K5III	2.23		-1.38 \pm 0.01		1604 \pm 80	3960 \pm 140 ^{s1}	9.94 \pm 0.05 ^{s1}
ε Lep	c	K4III	3.18	-0.20 \pm 0.03 ^{p1}			568 \pm 28	4243 \pm 25 ^{s2}	6.08 \pm 0.06 ^{s5}
HD 41047	c	K5III	5.52			1.740 \pm 0.218	96.7 \pm 4.9		2.47 \pm 0.03 ^{s4}
θ Umi ^l	c	K5III	4.98	1.33 \pm 0.05 ^{p2}			144 \pm 8.8		2.97 \pm 0.04 ^{s5}
HD 138265 ^l	c	K5III	5.90	2.38 \pm 0.04 ^{p2}			56.5 \pm 2.9	3758 \pm 166 ^{s3}	2.06 \pm 0.04 ^{s3}
β And	f	M0III	2.06		-1.93 \pm 0.01		2737 \pm 137	3880 \pm 140 ^{s1}	13.03 \pm 0.06 ^{s1}
ω Cap	c	M0III	4.12	0.21 \pm 0.03 ^{p1}			413 \pm 21	3760 \pm 150 ^{s4}	5.16 \pm 0.06 ^{s5}

^(l) Star is a proven reliable standard only up to 100 μm due to background confusion

^(p1) Ducati (2002, catalogue of stellar photometry in Johnson's 11-colour system)

^(p2) Neugebauer & Leighton (1969, two-micron sky survey)

^(p3) Selby et al. (1988)

^(p4) Cutri et al. (2003, 2MASS all-sky catalogue of point sources) Note: For $K_{s,2MASS} < 4$ mag photometric uncertainties are high, because fluxes were estimated from a fit to the wings of the saturated stellar profile (Skrutskie et al. 2006).

^(p5) For the fiducial standards we use the continuum model⁸ flux with an uncertainty of 5%; for the candidate stars we use the flux from scan map photometry.

^(s1) Dehaes et al. (2011)

^(s2) Jofré et al. (2015)

^(s3) Baines et al. (2010)

^(s4) Tsuji (1981)

^(s5) Cohen et al. (1999)

rect method, like comparison against a blackbody source, or by an indirect method, for example stellar or planetary atmosphere models. Deustua et al. (2013) give a detailed description of absolute calibration of astronomical flux standards. Primary flux standards in the far-infrared wavelength range are, with decreasing brightness, planets (Müller et al. 2016), asteroids (Müller et al. 2014), and stars (Dehaes et al. 2011), which are all calibrated via the indirect method and verified by independently calibrated multi-wavelength flux measurements. The best achievable uncertainties are currently 5 – 7%.

The Cohen et al. (1996) models of α Ari, ε Lep, ω Cap, δ Dra and HD 41047 are well confirmed by our PACS photometry and are thus adequate representations of the stellar FIR photospheric emission. These stars together with 42 Dra and HD 152222 are good candidates to establish fainter FIR primary standards. This list is complemented by θ Umi, HD 159330, and HD 138265 for which we can confirm a reliable FIR spectrum only up to 100 μm due to neighbouring source- or cirrus confusion at longer wavelengths.

As already discussed earlier, the Cohen et al. (1996) models are FIR extensions of absolutely calibrated 1.2 – 35 μm template spectra Cohen et al. (1995, 1999). Another set of models ranging from 0.7 μm to 7 cm was developed by Dehaes et al. (2011) for the *Herschel*-PACS fiducial primary standards. Several of our

faint primary standard candidates have the same or similar spectral type as one of the PACS primary standard stars. As a first model approximation we can scale these fiducial standard star models to the flux levels of our primary standard candidates. For an accurate model one would have to run a flux model code taking into account the stellar parameter information of each star, a project which is beyond the scope of this paper.

δ Dra with spectral type G9III has no suitable counterpart among the *Herschel*-PACS fiducial primary standards, since the earliest spectral type is K2III. But we note that it was modelled earlier by (Decin et al. 2003) as *ISO*-SWS calibrator. We do not include δ Dra in Table 11, but refer to Table 3 in Decin et al. (2003) which gives its stellar properties.

In Table 11 we have compiled photometry and stellar properties of the fiducial primary standards and our primary standard candidates which match in spectral type. Jofré et al. (2015) provide essential stellar parameters for α Ari, ε Lep, and 42 Dra, therefore a dedicated flux model code could be run.

In Table 12 we compile the K-magnitude ratio and the 100 μm flux ratio for matching pairs of fiducial primary standards and primary standard candidates. From both ratios we compute the scale factor for the fiducial star model as a weighted mean. We apply the following transformations between the different K-band photometric systems: (1) V-K = -0.020 + 0.989 \times

($V-K_n$) (Selby et al. 1988) and (2) $K = K_{s,2MASS} + 0.044$ (Bessel 2005). Scale factors are between 0.356 and 0.0026, that is, the faintest primary standard candidate, HD 152222, is about 360 times fainter than the related fiducial primary standard α Boo and still about 80 times fainter than the faintest fiducial primary standard, γ Dra. Table 12 also gives the percentage of the uncertainty of the scaling. We estimate the uncertainty due to variation in stellar parameters, such as the effective temperature, by scaling the fiducial model of α Tau to the level of γ Dra, which are both K5III stars. The difference over the wavelength range 2 – 250 μ m is less than 0.8%. We therefore adopt an uncertainty of 1% due to variations in stellar parameters. Given, that the fiducial primary standards have an absolute accuracy of 5%, then the absolute uncertainty of the scaled model approximation, as listed in the last column of Table 12, can be determined as the sum of the three uncertainty terms described above.

Figure 11 shows the scaling of the fiducial standard star models to the flux levels of our primary standard candidates and a verification with available photometry. K-band and PACS photometry are supplemented by *IRAS* FSC photometry (Moshir et al. 1989) and in some cases by ISOPHOT HDPD photometry (Lemke et al. 1996, see Appendix D).

For α Ari, ε Lep, ω Cap, HD 41047 and 42 Dra the derived absolute photometric uncertainty is in the range 5–6%, hence they are well suited new FIR primary standards, which are about 2 – 20 times fainter than our faintest fiducial primary standard γ Dra. Only for the faintest star, HD 152222, does the higher uncertainty of the scaling factor result in a derived absolute uncertainty of 13%. A major driver for this high scaling uncertainty is the high uncertainty of the publicly available K-band photometry (cf. Table 11, footnote p4), meaning that the K-magnitude ratio and the 100 μ m flux ratio do not match well. From Fig. 11 it is obvious that a more accurate K-band photometry would certainly help to bring this star into a similar absolute photometric uncertainty range to the brighter ones.

For θ Umi, HD 138265 and HD 159330, which are substantially affected by neighbouring source- or cirrus confusion at 160 μ m (Sects. 3.7 and 5.2), clean photometry can be obtained up to 100 μ m with a telescope of angular resolution similar to *Herschel*, which leads to an equally good absolute photometric uncertainty in the range 5 – 7%. Also, for HD 159330, improved K-band photometry can further reduce its resulting absolute photometric uncertainty. We therefore keep these three sources as reliable standards up to 100 μ m, but with the strong caveat not to use them beyond this wavelength. Only with a considerably higher angular resolution than *Herschel* could the confusion issues of these sources be overcome at 160 μ m.

HD 138265, HD 159330, and HD 152222 will be observable with the *James Webb Space Telescope* MIRI Imager at 20 μ m in bright source mode with the 64 \times 64 sub-array (Bouchet et al. 2015).

7. Conclusions

The PACS faint star sample with 14 giant and 3 dwarf stars has allowed a comprehensive sensitivity assessment of the PACS photometer and provided accurate photometry for detailed SED investigation and establishment of a set of faint FIR primary standard candidates for use by future space missions.

For PACS scan maps, the recommended scientific observation mode for the PACS photometer, we have described a consistent method for how to derive S/Ns, based on a robust noise measurement with the help of a flux histogram restricted to the applicable map coverage value range. The comparison with the

S/N predictions of the exposure time calculation tool in the *Herschel* Observatory Planning Tool HSpot has resulted in very good consistency, proving the tools for PACS photometry observation planning as very reliable. We have demonstrated that the underlying assumptions of the tool, that the S/N scales linearly with flux and with the square root of the observing time, are valid over large ranges of flux and time. A restriction appears for the 160 μ m filter, where source confusion often limits the gain in S/N with increasing observing time. We could also show that scan maps obtained with the recommended scan speed of 20''/s yield a higher S/N than scan maps with 10''/s, the scan speed favoured pre-flight.

We have shown that in the case of faint sources, small aperture sizes (with a radius of the size of the PSF FWHM) reduces background noise inside the aperture and optimizes the accuracy of the flux determination.

We have obtained reliable photometry for 11 stars in all three PACS filters (at 70, 100, 160 μ m). For one further star we have obtained reliable 100 and 160 μ m photometry. For one more star we have obtained reliable 70 and 100 μ m photometry only, 160 μ m photometry being limited here by confusion of neighbouring sources. For two other stars we have obtained reliable photometry only at 70 μ m, a detection at longer wavelengths being limited by sensitivity limitations and confusion noise. The two faintest sources observed in chop/nod mode have not been detected at all despite high repetition factors of the basic chop/nod pattern. The non-detection is likely due to a not-yet-perfect knowledge of the optimum observing strategy early in the mission. Faintest fluxes, for which the photometry has still good quality, are about 10 – 20 mJy for the scan map observations and 30 mJy for the available chop/nod observations.

For the faintest star at 160 μ m with reliable photometry in all three filters, HD 152222, we have conducted an inter-comparison of the high-pass filter (HPF) photometry from the deepest map with the results of three additional *Herschel* mapper softwares, namely JScanam, Scanamorphos and Unimap. All four mappers allow us to obtain sound photometry in all three filters. We have identified the level of qualitative consistency as well as some systematic differences with regard to photometry, noise, and beam profiles among the four mappers. A more systematic and quantitative photometric performance comparison of the four mappers will be the subject of a dedicated publication.

For the 12 stars with reliable photometry out to 160 μ m we can prove that 7 stars are consistent with models or flux predictions for pure photospheric emission. δ Dra has a slight 160 μ m excess due to cirrus contamination of the order of 4%, but this is still within the overall uncertainty margin. Two stars show excess emission over the whole (>10 μ m) FIR range. For β Gem (Pollux), which is the host star of a confirmed Jupiter-sized exoplanet, we conclude from our photometry results that it has in addition a flat blackbody dust disk. The G8 giant η Dra has a K1 dwarf companion, therefore the origin of the excess emission likely arises from dust inside this binary system. For three stars with 160 μ m fluxes below 60 mJy we find 160 μ m excesses in the order 6 to 9 mJy. Investigation of the 160 μ m absolute sky brightness with the help of *AKARI*-maps, the filamentary emission structure in the environment of the source on the PACS maps, and multi-aperture PACS photometry strongly support an explanation of this excess as being due to sky background confusion. This is a combination of cirrus confusion affecting the background subtraction and faint underlying objects inside the photometric aperture around the star affecting the source profile. The faintest star at 70 μ m with reliable photometry in all three filters, HD 39608, is heavily affected by sky confusion noise from

Table 12. Determination of the scale factor to adjust the related fiducial primary standard star model to the flux level of the candidate primary standard. The last two columns list the uncertainty percentage of the scale factor and the absolute uncertainty of the scaled model approximation, the latter being the Gaussian error propagation of the scale uncertainty, 1% uncertainty in the stellar parameters and 5% uncertainty of the models.

Primary candidate	Primary standard	Kmag ratio	f_{100} ratio	Scale factor	% scale uncert.	% abs. uncert.
α Ari	α Boo	$1.11 \pm 0.04 \cdot 10^{-1}$	$1.09 \pm 0.11 \cdot 10^{-1}$	$1.11 \pm 0.01 \cdot 10^{-1}$	0.9	5.2
42 Dra	α Boo	$1.03 \pm 0.06 \cdot 10^{-2}$	$9.73 \pm 1.00 \cdot 10^{-3}$	$1.01 \pm 0.03 \cdot 10^{-2}$	3.0	5.9
HD 152222	α Boo	$2.07 \pm 0.46 \cdot 10^{-3}$	$2.77 \pm 0.27 \cdot 10^{-3}$	$2.59 \pm 0.31 \cdot 10^{-3}$	12.0	13.0
HD 159330 ^l	α Boo	$4.58 \pm 0.92 \cdot 10^{-3}$	$4.13 \pm 0.46 \cdot 10^{-3}$	$4.22 \pm 0.18 \cdot 10^{-3}$	4.3	6.7
ϵ Lep	α Tau	$8.49 \pm 0.31 \cdot 10^{-2}$	$8.22 \pm 0.82 \cdot 10^{-2}$	$8.46 \pm 0.09 \cdot 10^{-2}$	1.1	5.2
ϵ Lep	γ Dra	$3.56 \pm 0.13 \cdot 10^{-1}$	$3.54 \pm 0.35 \cdot 10^{-1}$	$3.56 \pm 0.007 \cdot 10^{-1}$	0.2	5.1
HD 41047	α Tau	$1.37 \pm 0.29 \cdot 10^{-2}$	$1.40 \pm 0.14 \cdot 10^{-2}$	$1.39 \pm 0.01 \cdot 10^{-2}$	0.7	5.1
HD 41047	γ Dra	$5.73 \pm 1.21 \cdot 10^{-2}$	$6.03 \pm 0.61 \cdot 10^{-2}$	$5.97 \pm 0.12 \cdot 10^{-2}$	2.0	5.5
θ Umi ^l	α Tau	$2.07 \pm 0.12 \cdot 10^{-2}$	$2.08 \pm 0.23 \cdot 10^{-2}$	$2.07 \pm 0.004 \cdot 10^{-2}$	0.2	5.1
θ Umi ^l	γ Dra	$8.71 \pm 0.48 \cdot 10^{-2}$	$8.98 \pm 1.00 \cdot 10^{-2}$	$8.76 \pm 0.11 \cdot 10^{-2}$	1.3	5.3
HD 138265 ^l	α Tau	$7.88 \pm 0.36 \cdot 10^{-3}$	$8.18 \pm 0.83 \cdot 10^{-3}$	$7.93 \pm 0.11 \cdot 10^{-3}$	1.4	5.3
HD 138265 ^l	γ Dra	$3.31 \pm 0.15 \cdot 10^{-2}$	$3.52 \pm 0.36 \cdot 10^{-2}$	$3.34 \pm 0.07 \cdot 10^{-2}$	2.2	5.6
ω Cap	β And	$1.48 \pm 0.06 \cdot 10^{-1}$	$1.51 \pm 0.15 \cdot 10^{-1}$	$1.48 \pm 0.01 \cdot 10^{-1}$	0.7	5.1

(^l) Star is a proven reliable standard only up to 100 μm due to background confusion.

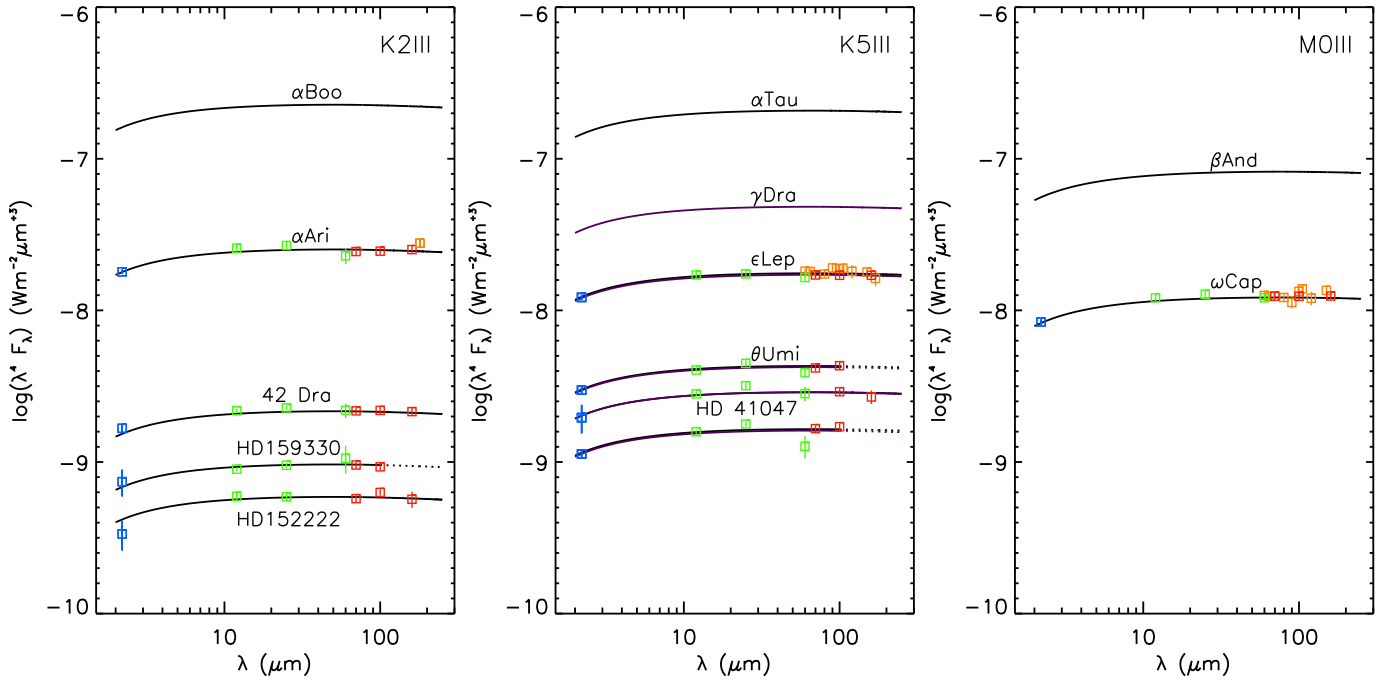


Fig. 11. Scaling of PACS fiducial star continuum models (black and purple lines) to the flux level of the primary standard candidates applying the scale factors of Table 12. For a better zoom-in over a large wavelength range, $\log_{10}(\lambda^4 \cdot f_\lambda)$ is displayed. Blue squares are the K-band photometry, green squares are colour-corrected *IRAS* FSC photometry (Moshir et al. 1989), orange squares are ISOPHOT HPDP photometry (Lemke et al. 1996, see Appendix D) and red squares are PACS photometry. In the middle panel the scaled models of both α Tau (black) and γ Dra (purple) are plotted. Dashed parts of the SEDs of HD 159330, θ Umi, and HD 138265 indicate that these stars are proven reliable standards only up to 100 μm due to background confusion.

100 μm onwards and has therefore to be excluded as a primary standard candidate.

The seven stars with pure photospheric emission over the full PACS wavelength range, α Ari, ϵ Lep, ω Cap, δ Dra, HD 41047, 42 Dra and HD 152222, are promising primary standard candidates. The stars θ Umi, HD 138265 and HD 159330 prove to be good primary standard candidates, too, but only up to 100 μm

due to significant source confusion at 160 μm at the spatial resolution of PACS. For three of the new primary standard candidates essential stellar parameters are known, meaning that a dedicated flux model code could be run. As a good model approximation for nine of our primary standard candidates we can scale the continuum flux models of four PACS fiducial standards with the same or quite similar spectral type. Only for δ Dra is

there no suitable counterpart among the fiducial standard stars. This allows us to establish a set of five FIR primary standard candidates up to $160\ \mu\text{m}$, which are 2 – 20 times fainter than the faintest PACS fiducial standard (γ Dra) with absolute accuracy of $<6\%$. The accuracy for the faintest primary standard candidate, HD152222 (80 times fainter than γ Dra), is currently limited to 13% by the accuracy of the existing K-band photometry. A set of three primary standard candidates up to $100\ \mu\text{m}$ with an absolute accuracy of $<7\%$ complements the list of proven flux standards.

Acknowledgements. PACS has been developed by a consortium of institutes led by MPE (Germany) and including UVIE (Austria); KUL, CSL, IMEC (Belgium); CEA, OAMP (France); MPA (Germany); IFSI, OAP/AOT, OAA/CAISMI, LENS, SISSA (Italy); IAC (Spain). This development has been supported by the funding agencies BMVIT (Austria), ESA-PRODEX (Belgium), CEA/CNES (France), DLR (Germany), ASI (Italy), and CICYT/MCYT (Spain). ZB acknowledges funding by DLR for this work. TM receives funding from the European Union's Horizon 2020 Research and Innovation Programme, under Grant Agreement no. 687378. This research has made use of the SIMBAD data base and the VizieR catalogue access tool, operated at CDS, Strasbourg, France. This research has made use of SAOImage DS9, developed by Smithsonian Astrophysical Observatory. This research has made use of the NASA/IPAC Infrared Science Archive, which is operated by the Jet Propulsion Laboratory, California Institute of Technology, under contract with the National Aeronautics and Space Administration. We thank the referee for constructive comments.

References

- Alonso, A., Arribas, S., & Martínez-Roger, C. 1999, *A&AS*, 140, 261
- Baines, E. K., Döllinger, M. P., Cusano, F., et al. 2010, *ApJ*, 710, 1365
- Balog, Z., Müller, T., Nielbock, M., et al. 2014, *Experimental Astronomy*, 37, 129
- Beckwith, S. V. W. 1999, *The origin of stars and planetary systems*. Edited by Charles J. Lada and Nikolaos D. Kylafis. Kluwer Academic Publishers, 579
- Berta, S., Magnelli, B., Nordon, R., et al. 2011, *A&A*, 532, A49
- Bessel, M. S. 2005, *ARA&A*, 43, 293
- Bianchi, S., Giovanardi, C., Smith, M. W. L., et al. 2017, *A&A*, 597, A130
- Blackwell, D. E., Lynas-Gray, A. E., & Petford, A. D. 1991, *A&A*, 245, 567
- Bottom, M., Kuhn, J., Mennesson, B., et al. 2015, *ApJ*, 809, 11B
- Bouchet, P., García-Marín, M., Lagage, P.-O., et al. 2015, *PASP*, 127, 612
- Chiang, E. I. & Goldreich, P. 1997, *ApJ*, 490, 368
- Cohen, M., Carbon, D. F., Welch, W. J., et al. 2005, *AJ*, 129, 2836
- Cohen, M., Walker, R. G., Barlow, M. J., & Deacon, J. R. 1992, *AJ*, 104, 1650
- Cohen, M., Walker, R. G., Carter, B., et al. 1999, *AJ*, 117, 1864
- Cohen, M., Witteborn, F. C., Carbon, D. F., et al. 1996, *AJ*, 112, 2274
- Cohen, M., Witteborn, F. C., Walker, R. G., Bregman, J. D., & Wooden, D. H. 1995, *AJ*, 110, 275
- Cutri, R. M., Skrutskie, M. F., van Dyk, S., et al. 2003, *VizieR 2MASS on-line data catalog*, II/246
- Decin, L., Vandenbussche, B., Waelkens, C., et al. 2003, *A&A*, 400, 709
- Dehaes, S., Bauwens, E., Decin, L., et al. 2011, *A&A*, 533, id.A107
- Deustua, S., Kent, S., & Smith, J. A. 2013, *Absolute Calibration of Astronomical Flux Standards*, ed. T. D. Oswalt & H. E. Bond (Springer), 375
- Doi, Y., Takita, S., Ootsubo, T., et al. 2015, *PASJ*, 67, 50
- Döllinger, M. P., Hatzes, A. P., Pasquini, L., et al. 2009, *A&A*, 499, 935
- Dommanget, J. & Nys, O. 2002, *VizieR on-line Catalog of the Components of Double & Multiple Stars (CCDM)*, I/274
- Ducati, J. R. 2002, *VizieR 11-color stellar photometry online data catalog*, II/237
- Dyck, H. M., Benson, J. A., Van Belle, G. T., & Ridgway, S. T. 1996, *AJ*, 111, 1705
- Fruchter, A. S. & Hook, R. N. 2002, *PASP*, 114, 144
- Gordon, K. D., Engelbracht, C. W., Fadda, D., et al. 2007, *PASP*, 119, 1019
- Graciá-Carpio, J., Wetzstein, M., & Roussel, H. 2015, to be published in *Astronomical Data Analysis Software and Systems XXV*. Editors N. P. F. Lorente and K. Shorridge. ASP Conference Series, arXiv:1512.03252v1 [astro-ph.IM]
- Gray, R. O., Corbally, C. J., Garrison, R. F., McFadden, M. T., & Robinson, P. E. 2003, *VizieR NStars online data catalog*, J/AJ/126/2048
- Groenewegen, M. 2012, *A&A*, 540, A32
- Hammersley, P. L., Jourdain de Muizon, M., Kessler, M. F., et al. 1998, *A&AS*, 128, 207
- Hatzes, A., Cochran, W., Endl, M., et al. 2006, *A&A*, 457, 335
- Herbstmeier, U., Abraham, P., Lemke, D., et al. 1998, *A&A*, 332, 739
- Herschel-Spot (HSpot) User's Guide: Herschel Observation Planning Tool*. 2013, *HERSCHEL-HSC-DOC-0788*, v 5.2 for HSpot v 7.0, <http://herschel.esac.esa.int/Docs/HSPOT/pdf/hspot>
- Jofré, E., Petrucci, R., Saffe, C., et al. 2015, *A&A*, 574, id.A50
- Judge, P. G., Jordan, C., & Rowan-Robinson, M. 1987, *MNRAS*, 224, 93
- Juvela, M., Mattila, K., Lemke, D., et al. 2009, *A&A*, 500, 763
- Kiss, C., Klaas, U., & Lemke, D. 2005, *A&A*, 430, 343
- Lee, B.-C., Mkrtichian, D., Han, A., Kim, K.-M., & Park, M.-G. 2011, *A&A*, 529, id.A134
- Lemke, D., Klaas, U., Abolins, J., et al. 1996, *A&A*, 315, L64
- Lutz, D. 2015, *Herschel Technical Report on PACS Photometer Point Spread Function*, PACC-ME-TN-033, http://herschel.esac.esa.int/twiki/pub/Public/PacsCalibrationWeb/bolopsf_22.pdf
- Lyubimkov, L. S. & Poklad, D. B. 2014, *Kinematics and physics of celestial bodies*, 30, No. 5, 244
- Meixner, M., Carter, R., Leisawitz, D., et al. 2017, *American Astronomical Society Meeting Abstracts*, 229, 238.20
- Moór, A., Müller, T. G., Kiss, C., et al. 2014, *Experimental Astronomy*, 37, 225
- Moshir, M., Copan, G., Conrow, T., et al. 1989, *VizieR IRAS FSC On-line Data Catalog*, II/156A
- Müller, T., Balog, Z., Nielbock, M., et al. 2014, *Experimental Astronomy*, 37, 253
- Müller, T., Balog, Z., Nielbock, M., et al. 2016, *A&A*, 588, id.A109
- Müller, T., Okumura, K., & Klaas, U. 2011, *Herschel Technical Report on PACS Photometer Passbands and Colour Correction Factors for Various Source SEDs*, PACC-ME-TN-038, http://herschel.esac.esa.int/twiki/pub/Public/PacsCalibrationWeb/cc_report.pdf
- Neugebauer, G. & Leighton, R. B. 1969, *VizieR two-micron sky survey on-line data catalog*, II/2B
- Nielbock, M., Müller, T., Klaas, U., et al. 2013, *Experimental Astronomy*, 36, 631
- Ott, S. 2010, *Astronomical Data Analysis Software and Systems XIX. Proceedings of a conference held October 4-8, 2009 in Sapporo, Japan*. Edited by Yoshihiko Mizumoto, Koh-Ichiro Morita, and Masatoshi Ohishi. ASP Conference Series, 434, 139
- Piazzo, L., Calzoletti, L., Faustini, F., et al. 2015, *MNRAS*, 447, 1471
- Pilbratt, G., Riedinger, J., Passvogel, T., et al. 2010, *A&A*, 518, id.L1
- Planck Collaboration, Abergel, A., Ade, P. A. R., et al. 2014, *A&A*, 571, A11
- Plets, H., Waelkens, C., Oudmaijer, R. D., & Waters, L. B. F. M. 1997, *A&A*, 323, 513
- Poglitsch, A., Waelkens, C., Geis, N., et al. 2010, *A&A*, 518, id.L2
- Popesso, D., Magnelli, B., Buttiglione, S., et al. 2012, arXiv:12114257v1 [astro-ph.IM], issue 1.0
- Roussel, H. 2013, *PASP*, 125, 1126
- Schulz, B., Marton, G., Valtchanov, I., et al. 2017, *SPIRE Point Source Catalog Explanatory Supplement*, arXiv:1706.00448
- Selby, M. J., Hepburn, I., Blackwell, D. E., et al. 1988, *A&AS*, 74, 127
- Shirahata, M., Hasegawa, S., Ootsubo, T., et al. 2009, *PASJ*, 61, 737
- Sibthorpe, B., Helmich, F., Roelfsema, P., Kaneda, H., & Shibai, H. 2015, *EAS Publication Series*, 75–76, 411
- Skrutskie, M. F., Cutri, R. M., Stiening, R., et al. 2006, *AJ*, 131, 1163
- Smirnov, A. V., Baryshev, A. M., Pilipenko, S. V., et al. 2012, *SPIE*, 84424C
- Takita, S., Doi, Y., Ootsubo, T., et al. 2015, *PASJ*, 67, 51
- Tsuji, T. 1981, *A&A*, 99, 48

Appendix A: Scan map photometry

Appendix A.1: Comparison of different aperture sizes for optimization of photometric aperture

Table A.1. Comparison of mini scan map photometry for different aperture sizes. *phot_l* is the photometry with the large aperture sizes 12"/12"/22", *phot_s* is the photometry with the small aperture sizes 5.6"/6.8"/10.7". Stellar fluxes f_{star} are determined as the colour-corrected weighted average of aperture corrected fluxes f_{tot} from # of individual scan maps. Model fluxes are from Table 1. Quoted uncertainties are the weighted standard deviations for $\# \geq 2$ and $\sigma_{\text{aper,corr}}$ (Eq. 4) for $\# = 1$.

Star	Filter (μm)	#	<i>phot_l</i> (mJy)	<i>phot_s</i> (mJy)	Model (mJy)
β Gem	70	8	2649.4 \pm 4.1	2648.7 \pm 1.2	2457.
	100	8	1287.1 \pm 2.4	1283.8 \pm 1.4	1190.
	160	16	497.4 \pm 5.8	496.9 \pm 2.1	455.9
α Ari	70	8	1668.3 \pm 3.7	1663.7 \pm 3.1	1707.
	100	8	831.6 \pm 4.3	820.2 \pm 1.8	831.4
	160	16	336.0 \pm 3.0	328.0 \pm 1.9	321.0
ϵ Lep	70	8	1157.1 \pm 6.5	1165.6 \pm 2.3	1182.
	100	12	568.8 \pm 2.7	568.4 \pm 1.6	576.2
	160	18	217.5 \pm 6.5	223.5 \pm 2.6	222.7
ω Cap	70	8	839.0 \pm 2.9	845.2 \pm 1.7	857.7
	100	8	414.3 \pm 1.8	412.8 \pm 1.4	418.0
	160	16	168.6 \pm 4.0	160.5 \pm 1.9	161.5
η Dra	70	8	517.8 \pm 13.0	506.0 \pm 2.6	479.5
	100	8	237.9 \pm 9.1	249.5 \pm 4.5	232.6
	160	16	116.4 \pm 7.3	98.4 \pm 5.1	89.4
δ Dra	70	12	433.6 \pm 2.1	436.0 \pm 1.1	428.9
	100	10	214.0 \pm 1.6	214.2 \pm 1.4	207.7
	160	22	89.0 \pm 5.1	85.4 \pm 2.2	79.6
θ Umi	70	4	278.7 \pm 5.7	284.2 \pm 1.5	286.2
	100	2	128.0 \pm 2.4	144.2 \pm 5.0	139.5
	160	2	72.8 \pm 10.4	62.3 \pm 2.5	53.9
HD 41047	100	2	99.4 \pm 2.3	96.7 \pm 0.7	95.4
	160	2	52.8 \pm 4.1	35.7 \pm 5.6	36.9
42 Dra	70	4	146.5 \pm 1.8	147.8 \pm 0.9	153.7
	100	4	75.1 \pm 1.7	73.1 \pm 0.9	75.3
	160	8	31.2 \pm 1.4	28.2 \pm 1.0	29.4
HD 138265	70	4	109.2 \pm 2.6	112.8 \pm 1.0	115.9
	100	6	57.2 \pm 1.6	56.5 \pm 0.5	56.8
	160	5	31.2 \pm 6.1	30.8 \pm 1.0	22.2
HD 159330	70	4	60.7 \pm 4.7	64.8 \pm 1.1	64.2
	100	6	32.9 \pm 2.3	31.0 \pm 1.1	31.5
HD 152222	70	4	35.1 \pm 1.0	39.0 \pm 0.9	39.4
	100	2	22.4 \pm 0.7	20.8 \pm 0.1	19.3
	160	4	6.2 \pm 2.2	7.4 \pm 0.8	7.5
HD 39608	70	3	29.8 \pm 3.4	30.5 \pm 1.1	30.9
	100	1	18.1 \pm 2.2	17.9 \pm 0.9	15.1
	160	2	18.2 \pm 2.6	12.1 \pm 0.7	5.9
HD 181597	70	2	25.9 \pm 3.3	29.1 \pm 2.0	28.0
	δ Hyi	70	1	7.7 \pm 2.4	22.2 \pm 1.5

Appendix A.2: Dependence on applied mapper software

For the faintest star at 160 μm with reliable photometry in all three filters, HD 152222, we conduct an inter-comparison of the high-pass filter (HPF) photometry from the deepest map with the results of three additional *Herschel* mapper softwares, namely

JScanam (Graciá-Carpio et al. 2015), Scanamorphos¹¹ (Roussel 2013) and Unimap¹¹ (Piazzo et al. 2015). The data analysis was done by applying the standard HIPE ipipe (interactive pipeline) scripts of these mappers¹² and selecting the same output pixel sizes as defined in Table 2.

For the Scanamorphos processing release version 25 of the software was applied, the "mini-map" option was selected, and the software was set to correct for the PACS distortion flat-field. For the JScanam processing version 14.2.0 (analogue to HIPE version) was applied and the "galactic" option was switched on. For the Unimap processing, version 6.5.3 was applied with the parameter *pixelNoise* (gain to apply to the estimated pixel noise in the GLS pixel noise compensation¹²) set to zero. For the comparison with the other mappers we used the weighted GLS (Generalized Least-Squares) L2.5 map product, corresponding to the FITS XTENSION "Image".

Table A.2. Comparison of the photometric results of HD 152222 from different mapper softwares: HPF (High Pass Filter, default reduction scheme of this work), JScanam (Graciá-Carpio et al. 2015), Scanamorphos (Roussel 2013) and Unimap (Piazzo et al. 2015). Used OBSIDs are the combinations of 1342240702+03 at 70 μm and 1342227973+74 at 100 and 160 μm . Listed fluxes are the colour-corrected total stellar fluxes f_{star} .

Mapper	Filter (μm)	r_{aper} (")	f_{star} (mJy)	σ_{aper} (mJy)	$\frac{f_{\text{star}}^{\text{mapper}}}{f_{\text{star}}^{\text{HPF}}}$
HPF	70	5.6	37.7	\pm 0.21	–
	100	6.8	20.7	\pm 0.15	–
	160	10.7	6.5	\pm 0.27	–
JScanam	70	5.6	39.3	\pm 0.24	1.04 \pm 0.02
	100	6.8	20.5	\pm 0.16	0.99 \pm 0.02
	160	10.7	6.5	\pm 0.31	1.00 \pm 0.14
Scanamorphos	70	5.6	35.5	\pm 0.19	0.94 \pm 0.02
	100	6.8	17.6	\pm 0.13	0.85 \pm 0.02
	160	10.7	4.2	\pm 0.28	0.65 \pm 0.11
Unimap	70	5.6	39.9	\pm 0.45	1.06 \pm 0.03
	100	6.8	20.5	\pm 0.23	0.99 \pm 0.03
	160	10.7	7.5	\pm 0.49	1.15 \pm 0.19

Since our analysis is restricted to one map in each filter, we do not intend to give a full quantitative performance assessment of the four mapper softwares, but rather point out some qualitative findings for these faint star map products.

Fig. A.1 shows the inter-comparison of the maps produced by the default High Pass Filter (HPF) mapper software and the three other mapper softwares for the three PACS filters. The star can be clearly identified as the central source in all three filters for all four mappers.

Table A.2 lists the colour-corrected total stellar fluxes f_{star} derived from aperture photometry with 5"6, 6"8 and 10"7 aperture radius at 70, 100 and 160 μm , respectively.

We also list the noise inside the measurement aperture, σ_{aper} (cf. Eq. 2), which was determined from all maps with the histogram method described in Sect. 3.3. We note that here only this noise term can be used for inter-comparison, not the one corrected for correlated noise, $\sigma_{\text{aper,corr}}$, since correlated noise

¹¹ *Herschel* user contributed software

<https://www.cosmos.esa.int/web/herschel/user-contributed-software>

¹² *Herschel* data processing overview

<https://www.cosmos.esa.int/web/herschel/data-processing-overview> in particular PACS Data Reduction Guide Photometry

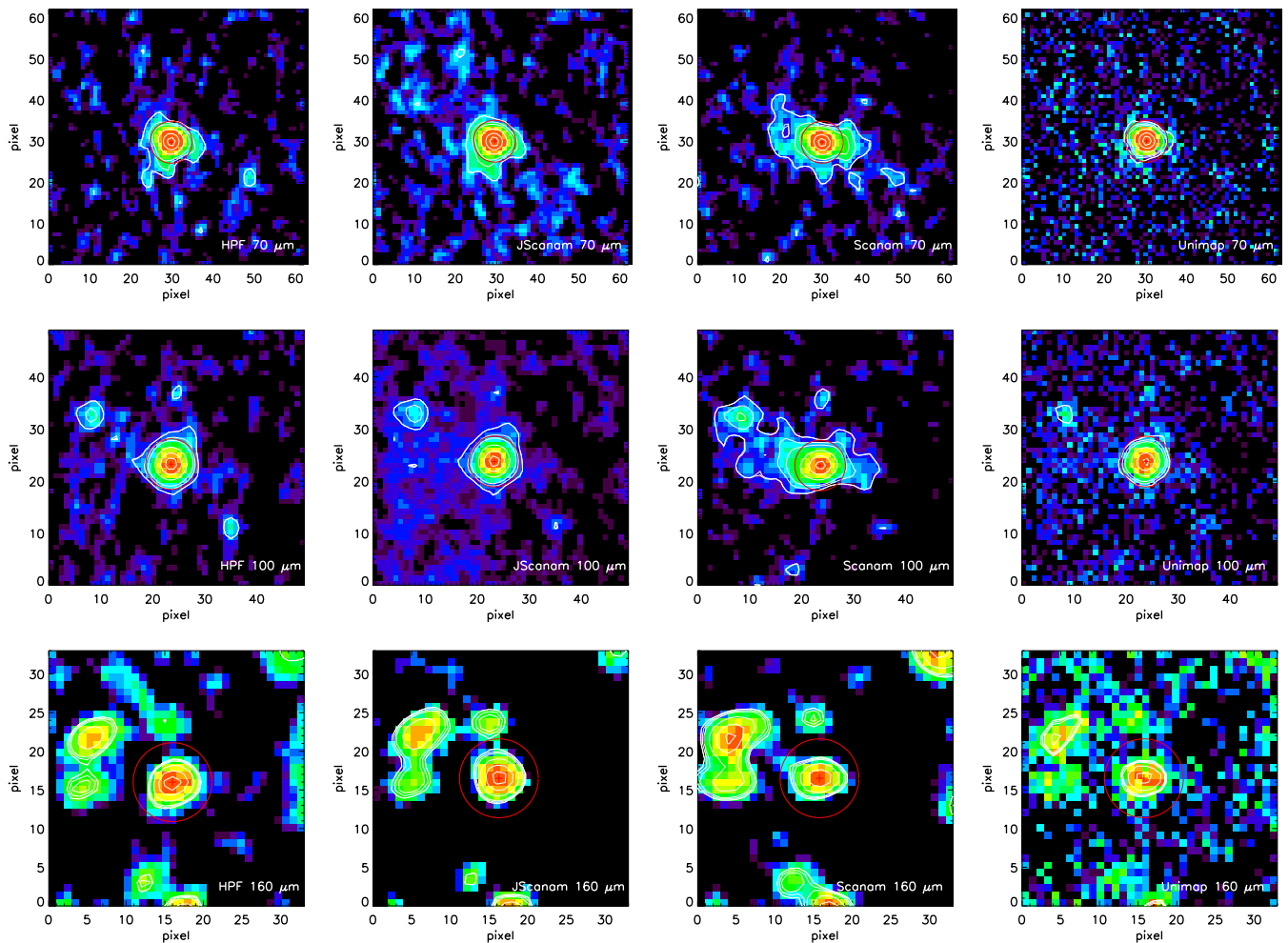


Fig. A.1. Inter-comparison of HD 152222 photometric maps for different mapper softwares for 70, 100, and 160 μm (top to bottom). First column: HPF (High Pass Filter, default reduction scheme of this work), second column: JScanam, third column: Scanamorphos and 4th column: Unimap. Used OBSIDs are the combinations of 1342240702+03 at 70 μm and 1342227973+74 at 100 and 160 μm . The red circle indicates the photometric aperture.

correction factors f_{corr} were only derived for the high-pass filtered data reduction (one may argue that the final corrected noise $\sigma_{\text{aper,corr}}$ should be about the same for all mappers, since it is mainly determined by the detector noise). A σ_{tot} for the total flux can be calculated as $\sigma_{\text{tot}} = c_{\text{aper}} \times \sigma_{\text{aper}}$.

The noise determined from the JScanam maps is slightly larger than that of the HPF maps. This finding indicates that the noise correlation is slightly less for the JScanam mapper. The noise determined from the Scanamorphos maps is slightly smaller than that of the HPF maps, indicating a slightly higher noise correlation. The noise determined from the Unimap maps is a factor of 1.5 – 2.1 higher than that of the HPF maps. This is explained by Unimap using the Generalized Least-Squares (GLS) algorithm to remove the correlated $\frac{1}{f}$ -noise (Piazzo et al. 2015). The Unimap noise is hence closer to the real noise level, and the above scaling factors do not exceed the correlated noise correction factors f_{corr} to be applied to the HPF noise (cf. Eq. 4 and Table 2) for calculation of the correlation-free noise level.

At 70 μm , with an expected source flux in the order of 40 mJy, the fluxes of all four mappers correspond to each other within 4 – 6%. At 100 μm , with an expected source flux in the order of 20 mJy, the correspondence is still better than 15%. At 160 μm , with an expected source flux of only ≈ 8 mJy and S/N

$\lesssim 10$, the scatter is naturally larger. Jscanam photometry shows the best correspondence with the HPF photometry, being within 4% for all filters. This can be expected, since both mappers use the same projection algorithm `photProject()`. Unimap photometry shows the second best correspondence with HPF photometry, with the tendency that the Unimap fluxes are larger (at 70 and 160 μm). Scanamorphos photometry gives systematically smaller fluxes than HPF photometry, with the deviation increasing with wavelength and a 160 μm flux which is noticeably off.

The PACS photometric calibration scheme (Balog et al. 2014) was established with HPF analysis, in particular also the derivation of the aperture photometry correction factors c_{aper} from the PACS Point Spread Function (Lutz 2015), by determining the Encircled Energy Fractions with radius. Therefore, one aspect affecting the aperture photometry depending on the selected mapper software was not considered in the evaluation scheme described above, namely the shape of the point spread function. From the inspection of the stellar intensity profiles and their close surrounding in Fig. A.1, in particular from the 70 and 100 μm images, it is obvious that there are systematic differences in the resulting profile shapes of the star depending on the applied mapper. The HPF processing shows the typical tri-lobe pattern of the PACS point spread function (Lutz

2015). The JScanam processing shows the closest appearance. The Unimap profiles look slightly sharper and show less pronounced lobes. The Scanamorphos profiles on the other hand appear somewhat less concentrated than the HPF profiles and with more pronounced lobes.

This means that for the other mappers adapted aperture correction factors should be applied, which alters the photometric results somewhat. The ratios $\frac{f_{\text{tot,cc}}^{\text{mapper}}}{f_{\text{tot,cc}}^{\text{HPF}}}$ in Table A.2 should not be used as general scaling factors between the various mappers, since they are based on the evaluation of a single map of a very faint star implying quite some uncertainty. Accurate scaling factors for photometry with the various mappers do not exist yet and will be determined on the basis of the high signal-to-noise fiducial standard observational database in a forthcoming paper (Balog et al., 2018, in preparation).

Appendix A.3: Photometry results of individual measurements

Individual photometric results for the 70, 100, and 160 μm filters are compiled in Tables A.3 to A.5. The applied radius for the photometric aperture was 5.6, 6.8 and 10.7'' for the 70, 100 and 160 μm filter, respectively. The number of output pixels (1''1, 1''4, and 2''1 size, respectively) inside this photometric aperture is $N_{\text{aper}} = 81.42, 74.12, \text{ and } 81.56$, respectively. The corresponding correction factors for correlated noise are $f_{\text{corr}} = 3.13, 2.76, \text{ and } 4.12$, respectively. Aperture correction factors are $c_{\text{aper}} = 1.61, 1.56 \text{ and } 1.56$ for the 70, 100 and 160 μm filter, respectively. Proper motion correction was applied throughout.

The tables contain the following information: Col. 1: Unique observational identifier (OBSID) of the PACS observation; Col. 2: Herschel Observational Day (OD); Col. 3: Target name; Col. 4: Applied gain (G) of the PACS bolometer electronics: h(igh)/l(ow); Col. 5: Scan speed: low = 10''/s, medium = 20''/s, high = 60''/s; Col. 6: Number of repetitions (rep.) of the basic scan map with the parameters given in next column; Col. 7: Parameters of the scan map: scan leg length('') / scan leg separation('') / number of scan legs; Col. 8: Scan angle of the map, in case of co-added maps all angles of the individual maps are given; Col. 9: Measured flux inside the photometric aperture of this filter, f_{aper} ; Col. 10: Noise per pixel, σ_{pix} ; Col. 11: Noise corrected for correlated noise inside the measurement aperture, $\sigma_{\text{aper,corr}}$, according to Eq. 4. Col. 12: Achieved signal-to-noise ratio according to Eq. 5; Col. 13: Stellar flux f_{star} according to Eq. 1; Cols. 14 - 16: Maximum and minimum Full Width (W) Half Maximum (in '') of the source PSF of the source PSF and its uncertainty determined by an elliptical fit to the intensity profile.

Table A.3. Scan map photometry measurements in the blue (70 μm filter). Processing proceeded from SPG v13.1.0 level 1 products with HIPE version 15 build 165.

OBSID	OD	Target	G	Speed ("/s)	Rep.	Map params ("/"/no.)	ScanAngles (deg)	f_{aper} (mJy)	σ_{pix} (mJy)	$\sigma_{\text{aper,corr}}$ (mJy)	S/N	f_{star} (mJy)	W_{max} (")	W_{min} (")	ΔW (")
1342217348	684	β Gem	h	20	3	180/4/10	70	1674.5	0.052	1.45	1152	2649.1	5.61	5.42	0.03
1342217349	684	β Gem	h	20	3	180/4/10	110	1672.7	0.052	1.48	1134	2646.3	5.74	5.19	0.03
1342217348+49	684	β Gem	h	20	6	180/4/10	70+110	1667.0	0.034	0.97	1728	2637.2	5.55	5.34	0.05
1342230120	872	β Gem	h	20	3	180/4/10	70	1676.4	0.052	1.47	1143	2652.1	5.53	5.44	0.03
1342230121	872	β Gem	h	20	3	180/4/10	110	1675.0	0.050	1.42	1183	2649.9	5.73	5.24	0.03
1342230120+21	872	β Gem	h	20	6	180/4/10	70+110	1669.4	0.034	0.97	1720	2641.1	5.58	5.31	0.04
1342242772	1051	β Gem	h	20	3	180/4/10	70	1678.4	0.057	1.60	1051	2655.2	5.52	5.41	0.03
1342242773	1051	β Gem	h	20	3	180/4/10	110	1671.3	0.055	1.55	1075	2644.1	5.71	5.17	0.03
1342242772+73	1051	β Gem	h	20	6	180/4/10	70+110	1671.2	0.039	1.10	1519	2644.0	5.55	5.25	0.04
1342252881	1244	β Gem	h	20	3	180/4/10	70	1672.6	0.051	1.45	1154	2646.1	5.52	5.48	0.03
1342252882	1244	β Gem	h	20	3	180/4/10	110	1673.6	0.049	1.38	1211	2647.7	5.72	5.32	0.03
1342252881+82	1244	β Gem	h	20	6	180/4/10	70+110	1670.3	0.034	0.96	1734	2642.4	5.48	5.34	0.05
1342212864	614	α Ari	h	20	3	180/4/10	70	1056.5	0.050	1.42	743	1671.5	5.59	5.25	0.03
1342212865	614	α Ari	h	20	3	180/4/10	110	1055.3	0.051	1.44	733	1669.5	5.51	5.40	0.04
1342212864+65	614	α Ari	h	20	6	180/4/10	70+110	1053.6	0.035	0.99	1067	1666.9	5.41	5.28	0.05
1342237398	974	α Ari	h	20	3	180/4/10	70	1048.2	0.050	1.41	742	1658.3	5.61	5.37	0.03
1342237399	974	α Ari	h	20	3	180/4/10	110	1049.1	0.050	1.41	744	1659.7	5.51	5.44	0.04
1342237398+99	974	α Ari	h	20	6	180/4/10	70+110	1045.9	0.034	0.96	1087	1654.7	5.47	5.35	0.05
1342248029	1157	α Ari	h	20	3	180/4/10	70	1058.3	0.050	1.41	749	1674.2	5.61	5.27	0.03
1342248030	1157	α Ari	h	20	3	180/4/10	110	1052.9	0.052	1.48	714	1665.7	5.54	5.52	0.04
1342248029+30	1157	α Ari	h	20	6	180/4/10	70+110	1052.7	0.034	0.97	1082	1665.4	5.48	5.30	0.05
1342259801	1344	α Ari	h	20	3	180/4/10	70	1051.3	0.052	1.46	719	1663.1	5.61	5.30	0.03
1342259802	1344	α Ari	h	20	3	180/4/10	110	1041.5	0.050	1.42	735	1647.7	5.51	5.50	0.04
1342259801+02	1344	α Ari	h	20	6	180/4/10	70+110	1043.3	0.036	1.01	1031	1650.4	5.49	5.38	0.05
1342205202	502	ϵ Lep	h	20	1	180/4/10	70	738.9	0.091	2.58	287	1169.0	5.55	5.42	0.03
1342205203	502	ϵ Lep	h	20	1	180/4/10	110	743.1	0.086	2.43	306	1175.5	5.73	5.24	0.03
1342205202+03	502	ϵ Lep	h	20	2	180/4/10	70+110	738.9	0.058	1.64	451	1168.9	5.53	5.34	0.05
1342227297	833	ϵ Lep	h	20	1	180/4/10	70	734.9	0.085	2.39	307	1162.6	5.64	5.30	0.03
1342227298	833	ϵ Lep	h	20	1	180/4/10	110	740.9	0.087	2.44	303	1172.1	5.52	5.38	0.03
1342227297+98	833	ϵ Lep	h	20	2	180/4/10	70+110	735.5	0.057	1.60	459	1163.6	5.51	5.34	0.05
1342241333	1034	ϵ Lep	h	20	1	180/4/10	70	736.6	0.086	2.44	302	1165.4	5.57	5.42	0.03
1342241334	1034	ϵ Lep	h	20	1	180/4/10	110	734.2	0.088	2.48	296	1161.4	5.68	5.28	0.03
1342241333+34	1034	ϵ Lep	h	20	2	180/4/10	70+110	732.8	0.059	1.66	442	1159.3	5.54	5.38	0.05
1342263904	1377	ϵ Lep	h	20	1	180/4/10	70	730.4	0.084	2.37	308	1155.5	5.60	5.28	0.03
1342263905	1377	ϵ Lep	h	20	1	180/4/10	110	735.6	0.082	2.32	317	1163.7	5.54	5.30	0.03
1342263904+05	1377	ϵ Lep	h	20	2	180/4/10	70+110	731.2	0.056	1.57	465	1156.7	5.43	5.28	0.05

Table A.3. Scan map photometry measurements in the blue (70 μ m filter) continued.

OBSID	OD	Target	G	Speed (''/s)	Rep.	Map params (''/no.)	ScanAngles (deg)	f_{aper} (mJy)	σ_{pix} (mJy)	$\sigma_{\text{aper,corr}}$ (mJy)	S/N	f_{star} (mJy)	W_{max} ('')	W_{min} ('')	ΔW ('')
1342218544	697	ω Cap	h	20	3	180/4/10	70	535.8	0.050	1.42	376	847.6	5.70	5.36	0.03
1342218545	697	ω Cap	h	20	3	180/4/10	110	532.8	0.048	1.36	392	842.9	5.48	5.34	0.03
1342218544+45	697	ω Cap	h	20	6	180/4/10	70+110	532.4	0.033	0.94	569	842.2	5.55	5.42	0.04
1342231259	889	ω Cap	h	20	3	180/4/10	70	535.7	0.050	1.41	380	847.5	5.61	5.25	0.03
1342231260	889	ω Cap	h	20	3	180/4/10	110	532.8	0.049	1.38	387	842.9	5.51	5.35	0.04
1342231259+60	889	ω Cap	h	20	6	180/4/10	70+110	532.3	0.033	0.94	564	842.0	5.50	5.29	0.04
1342243780	1058	ω Cap	h	20	3	180/4/10	70	536.1	0.049	1.39	386	848.1	5.68	5.33	0.03
1342243781	1058	ω Cap	h	20	3	180/4/10	110	538.8	0.050	1.40	384	852.4	5.52	5.50	0.04
1342243780+81	1058	ω Cap	h	20	6	180/4/10	70+110	535.7	0.034	0.96	558	847.5	5.54	5.40	0.05
1342254209	1266	ω Cap	h	20	3	180/4/10	70	529.0	0.051	1.44	367	836.9	5.65	5.27	0.03
1342254210	1266	ω Cap	h	20	3	180/4/10	110	532.5	0.051	1.43	374	842.5	5.48	5.37	0.03
1342254209+10	1266	ω Cap	h	20	6	180/4/10	70+110	528.6	0.032	0.90	586	836.3	5.51	5.30	0.04
1342186142	160	η Dra	h	10	1	120/5/9	80	327.5	0.101	2.86	115	518.1	5.43	5.18	0.04
1342186143	160	η Dra	h	10	1	120/5/9	100	318.8	0.097	2.74	117	504.3	5.35	5.30	0.04
1342186142+43	160	η Dra	h	10	2	120/5/9	80+100	323.1	0.071	2.01	161	511.2	5.28	5.14	0.05
1342186144	160	η Dra	h	10	1	90/5/9	60	320.5	0.113	3.19	101	507.0	5.37	5.10	0.05
1342186145	160	η Dra	h	10	1	90/5/9	120	316.5	0.110	3.11	102	500.7	5.33	5.17	0.04
1342186144+45	160	η Dra	h	10	2	90/5/9	60+120	317.6	0.075	2.11	151	502.5	5.20	5.11	0.05
1342186146	160	η Dra	h	20	1	90/5/9	70	311.7	0.132	3.71	83.9	493.1	5.48	5.24	0.05
1342186147	160	η Dra	h	20	1	90/5/9	110	314.4	0.127	3.58	87.7	497.4	5.54	5.40	0.04
1342186146+47	160	η Dra	h	20	2	90/5/9	70+110	311.6	0.084	2.38	131	492.9	5.38	5.33	0.05
1342186148	160	η Dra	h	10	1	150/4/9	85	321.1	0.091	2.58	125	508.0	5.23	5.05	0.05
1342186149	160	η Dra	h	10	1	150/4/9	95	322.1	0.090	2.53	127	509.5	5.26	5.26	0.04
1342186148+49	160	η Dra	h	10	2	150/4/9	85+95	320.3	0.063	1.77	181	506.8	5.21	5.09	0.05
1342189191	244	δ Dra	h	20	1	240/4/8	117	275.7	0.095	2.69	103	436.2	5.59	5.28	0.04
1342189192	244	δ Dra	h	20	1	240/4/8	63	270.4	0.096	2.71	99.9	427.8	5.49	5.22	0.03
1342189191+92	244	δ Dra	h	20	2	240/4/8	63+117	272.9	0.070	1.98	138	431.7	5.44	5.22	0.04
1342212499	607	δ Dra	h	20	3	180/4/10	70	278.4	0.052	1.45	191	440.4	5.58	5.31	0.04
1342212500	607	δ Dra	h	20	3	180/4/10	110	277.9	0.053	1.50	185	439.6	5.74	5.29	0.03
1342212499+500	244	δ Dra	h	20	6	180/4/10	70+110	277.3	0.035	1.00	278	438.8	5.59	5.31	0.05
1342222149	751	δ Dra	h	20	3	180/4/10	70	278.2	0.053	1.50	185	440.1	5.71	5.27	0.03
1342222150	751	δ Dra	h	20	3	180/4/10	110	274.4	0.049	1.38	199	434.1	5.38	5.30	0.04
1342222149+50	751	δ Dra	h	20	6	180/4/10	70+110	275.3	0.035	0.97	283	435.5	5.46	5.35	0.05
1342233571	934	δ Dra	h	20	3	180/4/10	70	277.2	0.050	1.42	195	438.6	6.06	5.23	0.03
1342233572	934	δ Dra	h	20	3	180/4/10	110	275.4	0.051	1.43	192	435.7	5.46	5.34	0.03
1342233571+72	934	δ Dra	h	20	6	180/4/10	70+110	275.7	0.036	1.00	275	436.2	5.64	5.35	0.05
1342250095	1198	δ Dra	h	20	3	180/4/10	70	275.2	0.052	1.47	187	435.3	5.55	5.45	0.04
1342250096	1198	δ Dra	h	20	3	180/4/10	110	271.3	0.050	1.42	191	429.1	5.66	5.06	0.03
1342250095+96	1198	δ Dra	h	20	6	180/4/10	70+110	272.8	0.035	0.99	275	431.5	5.53	5.29	0.04
1342257989	1328	δ Dra	h	20	3	180/4/10	70	276.6	0.049	1.39	198	437.6	5.60	5.39	0.03
1342257990	1328	δ Dra	h	20	3	180/4/10	110	273.8	0.050	1.40	195	433.1	5.63	5.34	0.03
1342257989+90	1328	δ Dra	h	20	6	180/4/10	70+110	274.6	0.035	0.97	282	434.4	5.49	5.34	0.05

Table A.3. Scan map photometry measurements in the blue (70 μm filter) continued.

OBSID	OD	Target	G	Speed ($''/\text{s}$)	Rep.	Map params ($''/\text{no.}$)	ScanAngles (deg)	f_{aper} (mJy)	σ_{pix} (mJy)	$\sigma_{\text{aper,corr}}$ (mJy)	S/N	f_{star} (mJy)	W_{max} ($''$)	W_{min} ($''$)	ΔW ($''$)
1342184574	139	θ Umi	h	10	1	210/15/4	90	173.4	0.126	3.57	48.6	274.4	5.09	4.97	0.07
1342184575	139	θ UMi	h	20	1	210/15/4	90	174.7	0.152	4.30	40.6	276.5	5.33	5.21	0.06
1342191982	300	θ Umi	h	20	6	150/4/10	70	179.6	0.038	1.06	170	284.2	5.67	5.29	0.03
1342191983	300	θ Umi	h	20	6	150/4/10	110	180.5	0.038	1.07	169	285.5	5.47	5.45	0.04
1342191982+83	300	θ Umi	h	20	12	150/4/10	70+110	179.5	0.025	0.70	255	284.0	5.48	5.42	0.05
1342203111	460	42Dra	h	20	20	180/4/10	70	94.6	0.020	0.57	166	149.6	5.50	5.50	0.04
1342203112	460	42Dra	h	20	20	180/4/10	110	93.4	0.020	0.55	170	147.7	5.76	5.12	0.03
1342203111+12	460	42Dra	h	20	40	180/4/10	70+110	94.0	0.013	0.38	249	148.8	5.58	5.27	0.05
1342243730	1057	42Dra	h	20	20	180/4/10	70	92.0	0.019	0.55	167	145.6	5.60	5.31	0.03
1342243731	1057	42Dra	h	20	20	180/4/10	110	93.8	0.020	0.56	168	148.3	5.57	5.40	0.03
1342243730+31	1057	42Dra	h	20	40	180/4/10	70+110	92.6	0.013	0.37	248	146.5	5.46	5.37	0.04
1342185446	146	HD 138265	h	20	1	210/4/20	90	74.2	0.071	1.99	37.3	117.4	5.54	5.37	0.06
1342185447	146	HD 138265	h	10	1	210/4/20	90	70.9	0.057	1.60	44.2	112.2	5.28	5.12	0.07
1342188841	233	HD 138265	h	20	21	240/4/8	63	72.3	0.023	0.64	113	114.3	5.50	5.46	0.04
1342188842	233	HD 138265	h	20	21	240/4/8	117	70.3	0.021	0.59	119	111.2	5.76	5.05	0.03
1342188841+42	233	HD 138265	h	20	42	240/4/8	63+117	71.0	0.016	0.44	160	112.3	5.59	5.27	0.04
1342186163	160	HD 159330	h	10	1	120/3/21	80	40.1	0.066	1.77	22.7	63.4	5.62	5.07	0.14
1342186164	160	HD 159330	h	10	1	120/3/21	100	43.5	0.066	1.76	24.7	68.9	5.80	5.50	0.11
1342186163+64	160	HD 159330	h	10	2	120/3/21	80+100	41.2	0.044	1.18	34.8	65.2	5.70	5.32	0.08
1342213585	628	HD 159330	h	20	6	180/4/10	70	40.0	0.036	0.96	41.7	63.2	5.41	5.37	0.06
1342213586	628	HD 159330	h	20	6	180/4/10	110	41.4	0.037	0.98	42.2	65.4	5.86	5.21	0.05
1342213585+86	628	HD 159330	h	20	12	180/4/10	70+110	40.5	0.024	0.63	64.0	64.1	5.58	5.27	0.06
1342191964	300	HD 152222	h	20	6	150/4/10	70	26.0	0.036	1.02	25.4	41.1	5.56	5.24	0.08
1342191965	300	HD 152222	h	20	6	150/4/10	110	25.2	0.038	1.07	23.6	39.9	5.55	5.50	0.09
1342191964+65	300	HD 152222	h	20	12	150/4/10	70+110	25.5	0.025	0.71	36.0	40.3	5.45	5.30	0.07
1342240702	1028	HD 152222	h	20	6	180/4/10	70	23.6	0.037	1.03	22.9	37.3	5.17	5.13	0.08
1342240703	1028	HD 152222	h	20	6	180/4/10	110	24.0	0.035	0.99	24.3	38.0	5.84	5.02	0.08
1342240702+03	1028	HD 152222	h	20	12	180/4/10	70+110	23.8	0.023	0.66	36.3	37.7	5.34	5.07	0.07
1342198535	400	HD 39608	h	20	10	180/4/10	70	21.3	0.028	0.79	26.9	33.6	6.01	5.26	0.08
1342198536	400	HD 39608	h	20	10	180/4/10	110	19.3	0.028	0.80	24.0	30.6	5.84	5.53	0.08
1342198538	400	HD 39608	h	20	35	180/4/10	110	18.6	0.015	0.43	43.1	29.5	5.40	5.18	0.06
1342198535+36+38	400	HD 39608	h	20	55	180/4/10	70+110	19.2	0.011	0.32	59.5	30.4	5.54	5.27	0.06
1342185450	146	HD 181597	h	10	9	210/4/20	90	17.4	0.019	0.53	32.6	27.5	5.25	4.74	0.08
1342185451	146	HD 181597	h	20	10	210/4/20	90	19.9	0.023	0.64	30.9	31.5	5.51	5.34	0.09
1342189130	241	δ Hyi	h	20	9	240/4/8	63	14.0	0.033	0.92	15.3	22.2	6.01	5.39	0.15

Table A.4. Scan map photometry measurements in the green (100 μm filter). Processing proceeded from SPG v13.1.0 level 1 products with HIPE version 15 build 165.

OBSID	OD	Target	G	Speed ("/s)	Rep.	Map params ("/"/no.)	ScanAngles (deg)	f_{aper} (mJy)	σ_{pix} (mJy)	$\sigma_{\text{aper,corr}}$ (mJy)	S/N	f_{star} (mJy)	W_{max} (")	W_{min} (")	ΔW (")
1342217351	684	β Gem	h	20	3	180/4/10	70	848.6	0.085	2.01	422	1282.9	6.76	6.52	0.04
1342217352	684	β Gem	h	20	3	180/4/10	110	847.4	0.082	1.95	435	1281.0	6.91	6.44	0.03
1342217351+52	684	β Gem	h	20	6	180/4/10	70+110	845.7	0.059	1.39	609	1278.4	6.79	6.44	0.05
1342230122	872	β Gem	h	20	3	180/4/10	70	851.3	0.078	1.85	459	1287.0	6.72	6.52	0.03
1342230123	872	β Gem	h	20	3	180/4/10	110	847.2	0.080	1.90	446	1280.8	6.95	6.42	0.03
1342230122+23	872	β Gem	h	20	6	180/4/10	70+110	846.9	0.052	1.25	680	1280.3	6.79	6.41	0.05
1342242770	1051	β Gem	h	20	3	180/4/10	70	844.8	0.084	1.99	424	1277.1	6.74	6.54	0.04
1342242771	1051	β Gem	h	20	3	180/4/10	110	850.7	0.079	1.87	455	1286.0	6.88	6.49	0.04
1342242770+71	1051	β Gem	h	20	6	180/4/10	70+110	845.0	0.055	1.31	647	1277.5	6.74	6.49	0.05
1342252879	1244	β Gem	h	20	3	180/4/10	70	851.7	0.083	1.96	434	1287.5	6.78	6.52	0.03
1342252880	1244	β Gem	h	20	3	180/4/10	110	851.4	0.075	1.77	481	1287.1	6.92	6.43	0.03
1342252879+80	1244	β Gem	h	20	6	180/4/10	70+110	850.2	0.055	1.30	655	1285.3	6.75	6.41	0.05
1342212862	614	α Ari	h	20	3	180/4/10	70	538.9	0.079	1.87	288	814.7	6.84	6.52	0.04
1342212863	614	α Ari	h	20	3	180/4/10	110	545.9	0.081	1.93	282	825.3	6.78	6.63	0.04
1342212862+63	614	α Ari	h	20	6	180/4/10	70+110	540.5	0.055	1.31	413	817.1	6.73	6.56	0.05
1342237396	974	α Ari	h	20	3	180/4/10	70	547.5	0.080	1.89	289	827.7	6.87	6.50	0.04
1342237397	974	α Ari	h	20	3	180/4/10	110	540.2	0.078	1.84	293	816.6	6.80	6.57	0.03
1342237396+97	974	α Ari	h	20	6	180/4/10	70+110	543.2	0.055	1.30	418	821.1	6.72	6.46	0.05
1342248027	1157	α Ari	h	20	3	180/4/10	70	540.1	0.084	1.98	272	816.6	6.82	6.50	0.03
1342248028	1157	α Ari	h	20	3	180/4/10	110	539.5	0.085	2.02	267	815.6	6.73	6.59	0.04
1342248027+28	1157	α Ari	h	20	6	180/4/10	70+110	538.4	0.056	1.32	407	813.9	6.77	6.54	0.05
1342259799	1344	α Ari	h	20	3	180/4/10	70	544.6	0.081	1.92	283	823.4	6.83	6.52	0.04
1342259800	1344	α Ari	h	20	3	180/4/10	110	543.4	0.082	1.95	278	821.5	6.71	6.68	0.04
134259799+800	1344	α Ari	h	20	6	180/4/10	70+110	539.0	0.055	1.31	413	814.8	6.71	6.54	0.05
1342190969	284	ϵ Lep	h	20	1	150/4/10	70	377.5	0.139	3.29	115	570.6	6.72	6.48	0.05
1342190970	284	ϵ Lep	h	20	1	150/4/10	110	372.9	0.144	3.42	109	563.7	6.70	6.63	0.04
1342190969+70	284	ϵ Lep	h	20	2	150/4/10	70+110	374.3	0.099	2.34	160	565.8	6.63	6.49	0.05
1342205204	502	ϵ Lep	h	20	3	180/4/10	70	379.2	0.078	1.85	205	573.2	6.76	6.55	0.04
1342205205	502	ϵ Lep	h	20	3	180/4/10	110	373.6	0.081	1.93	193	564.8	6.90	6.44	0.04
1342205204+05	502	ϵ Lep	h	20	6	180/4/10	70+110	375.2	0.053	1.25	299	567.3	6.76	6.44	0.05
1342214208	640	ϵ Lep	h	20	3	180/4/10	70	371.6	0.077	1.82	204	561.8	6.79	6.47	0.04
1342214209	640	ϵ Lep	h	20	3	180/4/10	110	373.4	0.081	1.91	195	564.6	6.76	6.58	0.04
1342214208+09	640	ϵ Lep	h	20	6	180/4/10	70+110	370.9	0.054	1.28	290	560.7	6.73	6.54	0.05
1342227299	833	ϵ Lep	h	20	3	180/4/10	70	377.8	0.077	1.84	206	571.1	6.90	6.50	0.04
1342227300	833	ϵ Lep	h	20	3	180/4/10	110	374.5	0.077	1.83	205	566.1	6.78	6.54	0.04
1342227299+300	833	ϵ Lep	h	20	6	180/4/10	70+110	375.0	0.051	1.21	310	566.8	6.80	6.50	0.05
1342241335	1034	ϵ Lep	h	20	3	180/4/10	70	383.0	0.078	1.86	206	579.0	6.85	6.68	0.04
1342241336	1034	ϵ Lep	h	20	3	180/4/10	110	379.9	0.082	1.94	196	574.3	6.82	6.44	0.04
1342241335+36	1034	ϵ Lep	h	20	6	180/4/10	70+110	379.7	0.054	1.28	296	574.0	6.81	6.62	0.05
1342263902	1377	ϵ Lep	h	20	3	180/4/10	70	375.2	0.078	1.86	202	567.3	6.84	6.53	0.04
1342263903	1377	ϵ Lep	h	20	3	180/4/10	110	372.6	0.077	1.83	203	563.2	6.67	6.57	0.04
1342263902+03	1377	ϵ Lep	h	20	6	180/4/10	70+110	373.1	0.053	1.25	298	564.0	6.68	6.47	0.05

Table A.4. Scan map photometry measurements in the green (100 μ m filter) continued.

OBSID	OD	Target	G	Speed ("/s)	Rep.	Map params ("/"/no.)	ScanAngles (deg)	f_{aper} (mJy)	σ_{pix} (mJy)	$\sigma_{\text{aper,corr}}$ (mJy)	S/N	f_{star} (mJy)	W_{max} (")	W_{min} (")	ΔW (")
1342218546	697	ω Cap	h	20	3	180/4/10	70	271.3	0.084	1.98	137	410.1	6.75	6.44	0.04
1342218547	697	ω Cap	h	20	3	180/4/10	110	270.5	0.078	1.85	146	409.0	6.69	6.65	0.04
1342218546+47	697	ω Cap	h	20	6	180/4/10	70+110	270.4	0.055	1.31	207	408.7	6.60	6.54	0.05
1342231261	889	ω Cap	h	20	3	180/4/10	70	276.7	0.084	1.98	139	418.3	6.82	6.53	0.04
1342231262	889	ω Cap	h	20	3	180/4/10	110	272.0	0.081	1.93	141	411.2	6.77	6.50	0.04
1342231261+62	889	ω Cap	h	20	6	180/4/10	70+110	273.5	0.057	1.35	203	413.4	6.75	6.46	0.05
1342243778	1058	ω Cap	h	20	3	180/4/10	70	272.9	0.077	1.82	150	412.5	6.78	6.54	0.04
1342243779	1058	ω Cap	h	20	3	180/4/10	110	275.8	0.081	1.93	143	416.9	6.86	6.59	0.04
1342243778+79	1058	ω Cap	h	20	6	180/4/10	70+110	273.4	0.053	1.25	219	413.3	6.74	6.54	0.05
1342254207	1266	ω Cap	h	20	3	180/4/10	70	275.4	0.077	1.82	151	416.4	6.79	6.44	0.04
1342254208	1266	ω Cap	h	20	3	180/4/10	110	270.0	0.076	1.81	149	408.1	6.65	6.49	0.04
1342254207+08	1266	ω Cap	h	20	6	180/4/10	70+110	271.5	0.050	1.20	227	410.4	6.68	6.44	0.05
1342186151	160	η Dra	h	10	1	120/5/9	80	160.4	0.160	3.79	42.3	242.6	6.72	6.30	0.08
1342186152	160	η Dra	h	10	1	120/5/9	100	171.3	0.159	3.78	45.3	258.9	6.79	6.54	0.09
1342186151+52	160	η Dra	h	10	2	120/5/9	80+100	165.5	0.108	2.57	64.5	250.2	6.79	6.43	0.08
1342186153	160	η Dra	h	10	1	90/5/9	60	180.3	0.188	4.46	40.4	272.6	7.28	6.22	0.08
1342186154	160	η Dra	h	10	1	90/5/9	120	158.9	0.177	4.21	37.8	240.2	6.60	6.57	0.09
1342186153+54	160	η Dra	h	10	2	90/5/9	60+120	169.0	0.124	2.94	57.4	255.6	6.85	6.35	0.08
1342186155	160	η Dra	h	20	1	90/5/9	70	164.0	0.214	5.07	32.3	247.9	6.91	6.51	0.08
1342186156	160	η Dra	h	20	1	90/5/9	110	169.2	0.197	4.68	36.1	255.9	6.99	6.83	0.09
1342186155+56	160	η Dra	h	20	2	90/5/9	70+110	167.0	0.145	3.43	48.6	252.5	6.77	6.57	0.08
1342186157	160	η Dra	h	10	1	150/4/9	85	167.5	0.147	3.49	48.0	253.3	6.70	6.59	0.11
1342186158	160	η Dra	h	10	1	150/4/9	95	154.1	0.146	3.46	44.5	232.9	6.31	6.24	0.07
1342186157+58	160	η Dra	h	10	2	150/4/9	85+95	160.2	0.099	2.34	68.4	242.2	6.49	6.46	0.09
1342212497	607	δ Dra	h	20	3	180/4/10	70	141.7	0.081	1.94	73.4	214.2	6.74	6.46	0.05
1342212498	607	δ Dra	h	20	3	180/4/10	110	143.2	0.081	1.92	74.4	216.5	6.75	6.53	0.05
1342212497+98	607	δ Dra	h	20	6	180/4/10	70+110	141.7	0.053	1.25	113	214.3	6.72	6.48	0.05
1342222147	751	δ Dra	h	20	3	180/4/10	70	140.6	0.081	1.92	73.1	212.5	6.76	6.43	0.05
1342222148	751	δ Dra	h	20	3	180/4/10	110	138.1	0.081	1.91	72.2	208.8	6.56	6.51	0.05
1342222147+48	751	δ Dra	h	20	6	180/4/10	70+110	138.8	0.057	1.36	102	209.8	6.67	6.44	0.05
1342233573	934	δ Dra	h	20	3	180/4/10	70	139.2	0.080	1.89	73.6	210.4	6.92	6.38	0.05
1342233574	934	δ Dra	h	20	3	180/4/10	110	138.3	0.077	1.84	75.2	209.0	6.57	6.54	0.05
1342233573+74	934	δ Dra	h	20	6	180/4/10	70+110	138.8	0.054	1.29	108	209.8	6.73	6.41	0.05
1342250093	1198	δ Dra	h	20	3	180/4/10	70	143.1	0.079	1.88	76.3	216.4	6.72	6.64	0.05
1342250094	1198	δ Dra	h	20	3	180/4/10	110	141.4	0.078	1.86	76.0	213.7	6.76	6.47	0.05
1342250093+94	1198	δ Dra	h	20	6	180/4/10	70+110	142.0	0.055	1.31	109	214.6	6.63	6.52	0.06
1342257987	1328	δ Dra	h	20	3	180/4/10	70	144.7	0.079	1.86	77.6	218.7	6.84	6.47	0.05
1342257988	1328	δ Dra	h	20	3	180/4/10	110	146.6	0.080	1.90	77.0	221.6	6.90	6.79	0.05
1342257987+88	1328	δ Dra	h	20	6	180/4/10	70+110	145.1	0.051	1.21	119	219.3	6.82	6.60	0.05

Table A.4. Scan map photometry measurements in the green (100 μm filter) continued.

OBSID	OD	Target	G	Speed ($''/\text{s}$)	Rep.	Map params ($''/\text{no.}$)	ScanAngles (deg)	f_{aper} (mJy)	σ_{pix} (mJy)	$\sigma_{\text{aper,corr}}$ (mJy)	S/N	f_{star} (mJy)	W_{max} ($''$)	W_{min} ($''$)	ΔW ($''$)
1342184585	139	θUmi	h	10	1	210/15/4	90	98.1	0.204	4.84	20.3	148.3	6.74	6.38	0.19
1342184586	139	θUmi	h	20	1	210/15/4	90	91.6	0.246	5.84	15.7	138.4	7.48	6.15	0.16
1342190972	284	HD 41047	h	20	3	150/4/10	70	64.4	0.082	1.94	33.3	97.4	6.77	6.37	0.09
1342190973	284	HD 41047	h	20	3	150/4/10	110	63.5	0.084	1.99	31.8	95.9	6.81	6.59	0.10
1342190972+73	284	HD 41047	h	20	6	150/4/10	70+110	63.7	0.059	1.40	45.5	96.2	6.70	6.42	0.07
1342203113	460	42 Dra	h	20	20	180/4/10	70	49.0	0.034	0.80	61.1	74.1	6.77	6.59	0.07
1342203114	460	42 Dra	h	20	20	180/4/10	110	46.7	0.033	0.78	59.9	70.6	6.84	6.33	0.06
1342203113+14	460	42 Dra	h	20	40	180/4/10	70+110	47.9	0.023	0.54	89.4	72.4	6.68	6.53	0.07
1342243732	1057	42 Dra	h	20	20	180/4/10	70	48.7	0.031	0.74	65.6	73.6	6.78	6.57	0.06
1342243733	1057	42 Dra	h	20	20	180/4/10	110	49.1	0.031	0.74	65.9	74.2	6.75	6.54	0.05
1342243732+33	1057	42 Dra	h	20	40	180/4/10	70+110	48.8	0.021	0.49	99.5	73.7	6.72	6.49	0.06
1342184302	132	HD 138265	h	10	3	210/4/25	90	37.6	0.048	1.15	32.8	56.8	6.91	6.51	0.10
1342184303	132	HD 138265	h	20	3	210/4/25	90	37.3	0.058	1.38	27.1	56.4	6.86	6.46	0.10
1342185448	146	HD 138265	h	20	1	210/4/20	90	39.8	0.106	2.51	15.8	60.2	7.00	6.94	0.19
1342185449	146	HD 138265	h	10	1	210/4/20	90	38.1	0.095	2.25	17.0	57.6	6.70	6.27	0.14
1342191986	300	HD 138265	h	20	6	150/4/10	70	36.7	0.064	1.52	24.2	55.4	6.83	6.24	0.09
1342191987	300	HD 138265	h	20	6	150/4/10	110	36.9	0.056	1.34	27.6	55.8	6.74	6.73	0.11
1342191986+87	300	HD 138265	h	20	12	150/4/10	70+110	36.4	0.044	1.04	35.0	55.0	6.68	6.40	0.08
1342186160	160	HD 159330	h	10	1	120/3/21	80	18.0	0.104	2.46	7.3	27.3	6.83	5.93	0.31
1342186161	160	HD 159330	h	10	1	120/3/21	100	17.0	0.109	2.60	6.5	25.7	5.19	5.01	0.39
1342186160+61	160	HD 159330	h	10	2	120/3/21	80+100	17.3	0.072	1.72	10.1	26.2	6.22	6.03	0.26
1342188839	233	HD 159330	h	20	10	240/4/8	63	20.3	0.050	1.18	17.3	30.7	6.66	6.78	0.21
1342188840	233	HD 159330	h	20	10	240/4/8	117	23.4	0.049	1.16	20.1	35.3	7.23	6.33	0.15
1342188839+40	233	HD 159330	h	20	20	240/4/8	63+117	21.7	0.034	0.81	26.9	32.8	6.90	6.60	0.14
1342213583	628	HD 159330	h	20	15	180/4/10	70	20.9	0.036	0.86	24.4	31.6	6.69	6.67	0.16
1342213584	628	HD 159330	h	20	15	180/4/10	110	19.3	0.036	0.86	22.4	29.1	6.46	5.60	0.13
1342213583+84	628	HD 159330	h	20	30	180/4/10	70+110	20.3	0.024	0.58	35.2	30.7	6.57	6.15	0.12
1342227973	843	HD 152222	h	20	33	180/4/10	70	13.7	0.025	0.60	23.0	20.7	6.59	6.40	0.13
1342227974	843	HD 152222	h	20	33	180/4/10	110	13.9	0.024	0.56	24.9	20.9	7.01	6.55	0.13
1342227973+74	843	HD 152222	h	20	66	180/4/10	70+110	13.7	0.017	0.40	34.3	20.7	6.76	6.56	0.09
1342198537	400	HD 39608	h	20	35	180/4/10	70	11.9	0.024	0.57	20.9	17.9	7.57	7.21	0.17

Table A.5. Scan map photometry measurements in the red (160 μm filter). Processing proceeded from SPG v14.2.0 level 1 products with HIPE version 15 build 1480.

OBSID	OD	Target	G	Speed ("'/s)	Rep.	Map params ("'/no.)	ScanAngles (deg)	f_{aper} (mJy)	σ_{pix} (mJy)	$\sigma_{\text{aper,corr}}$ (mJy)	S/N	f_{star} (mJy)	W_{max} (")	W_{min} (")	ΔW (")
1342217348	684	β Gem	h	20	3	180/4/10	70	345.7	0.123	4.59	75.3	502.0	11.37	9.95	0.16
1342217349	684	β Gem	h	20	3	180/4/10	110	351.8	0.124	4.62	76.2	510.9	11.67	9.78	0.18
1342217351	684	β Gem	h	20	3	180/4/10	70	346.8	0.145	5.39	64.4	503.6	11.35	9.83	0.17
1342217352	684	β Gem	h	20	3	180/4/10	110	341.4	0.127	4.72	72.2	495.8	11.51	9.67	0.16
..48+49+51+52	684	β Gem	h	20	12	180/4/10	70+110	345.2	0.066	2.44	141	501.2	11.40	9.80	0.28
1342230120	872	β Gem	h	20	3	180/4/10	70	336.7	0.121	4.51	74.7	489.0	10.97	9.78	0.18
1342230121	872	β Gem	h	20	3	180/4/10	110	345.7	0.127	4.74	72.9	502.0	11.08	9.76	0.18
1342230122	872	β Gem	h	20	3	180/4/10	70	350.2	0.144	5.36	65.4	508.5	10.87	9.86	0.19
1342230123	872	β Gem	h	20	3	180/4/10	110	343.9	0.112	4.17	82.6	499.3	11.05	9.74	0.18
..20+21+22+23	872	β Gem	h	20	12	180/4/10	70+110	343.1	0.066	2.45	141	498.2	11.06	9.78	0.31
1342242770	1051	β Gem	h	20	3	180/4/10	70	332.2	0.144	5.38	61.7	482.4	11.16	9.54	0.17
1342242771	1051	β Gem	h	20	3	180/4/10	110	340.9	0.122	4.53	75.2	495.0	11.46	9.77	0.20
1342242772	1051	β Gem	h	20	3	180/4/10	70	332.0	0.130	4.84	68.7	482.1	11.32	9.80	0.17
1342242773	1051	β Gem	h	20	3	180/4/10	110	344.6	0.131	4.88	70.6	500.5	11.45	9.55	0.21
..70+71+72+73	1051	β Gem	h	20	12	180/4/10	70+110	339.0	0.069	2.58	131	492.3	11.37	9.68	0.26
1342252879	1244	β Gem	h	20	3	180/4/10	70	336.9	0.127	4.74	71.1	489.2	11.34	9.89	0.16
1342252880	1244	β Gem	h	20	3	180/4/10	110	343.3	0.128	4.76	72.1	498.5	10.93	9.62	0.16
1342252881	1244	β Gem	h	20	3	180/4/10	70	339.1	0.125	4.67	72.7	492.4	11.01	9.75	0.18
1342252882	1244	β Gem	h	20	3	180/4/10	110	343.5	0.114	4.23	81.2	498.7	11.11	9.66	0.17
..79+80+81+82	1244	β Gem	h	20	12	180/4/10	70+110	338.9	0.059	2.20	153	492.1	11.30	10.02	0.32
1342212862	614	α Ari	h	20	3	180/4/10	70	230.1	0.133	4.95	46.4	334.1	11.42	10.11	0.21
1342212863	614	α Ari	h	20	3	180/4/10	110	220.1	0.121	4.51	48.8	319.6	10.89	9.88	0.22
1342212864	614	α Ari	h	20	3	180/4/10	70	228.9	0.121	4.50	50.9	332.4	10.81	9.66	0.21
1342212865	614	α Ari	h	30	3	180/4/10	110	227.0	0.120	4.48	50.6	329.6	11.27	9.80	0.22
..62+63+64+65	614	α Ari	h	20	12	180/4/10	70+110	225.2	0.063	2.34	96.0	327.1	11.01	9.87	0.43
1342237396	974	α Ari	h	20	3	180/4/10	70	221.1	0.118	4.41	50.2	321.0	11.27	10.04	0.23
1342237397	974	α Ari	h	20	3	180/4/10	110	227.7	0.121	4.49	50.7	330.7	11.01	10.01	0.21
1342237398	974	α Ari	h	20	3	180/4/10	70	223.8	0.140	5.21	42.9	325.0	10.85	9.69	0.20
1342237399	974	α Ari	h	20	3	180/4/10	110	225.4	0.141	5.26	42.9	327.3	10.82	9.66	0.22
..96+97+98+99	974	α Ari	h	20	12	180/4/10	70+110	223.7	0.071	2.65	84.5	324.8	11.10	9.81	0.35
1342248027	1157	α Ari	h	20	3	180/4/10	70	228.9	0.131	4.87	47.0	332.4	10.94	9.97	0.19
1342248028	1157	α Ari	h	20	3	180/4/10	110	230.4	0.122	4.55	50.6	334.6	10.69	10.13	0.18
1342248029	1157	α Ari	h	20	3	180/4/10	70	233.9	0.139	5.18	45.2	339.7	11.43	10.03	0.19
1342248030	1157	α Ari	h	20	3	180/4/10	110	232.3	0.127	4.72	49.1	337.3	10.91	9.99	0.22
..27+28+29+30	1157	α Ari	h	20	12	180/4/10	70+110	230.4	0.078	2.91	79.2	334.5	11.03	9.98	0.34
1342259799	1344	α Ari	h	20	3	180/4/10	70	215.8	0.131	4.88	44.2	313.3	11.54	9.97	0.18
1342259800	1344	α Ari	h	20	3	180/4/10	110	221.0	0.116	4.32	51.2	320.9	10.78	9.97	0.19
1342259801	1344	α Ari	h	20	3	180/4/10	70	228.2	0.129	4.82	47.3	331.4	11.58	9.95	0.15
1342259802	1344	α Ari	h	20	3	180/4/10	110	221.3	0.127	4.71	47.0	321.3	10.79	9.95	0.22
..799+800+01+02	1344	α Ari	h	20	12	180/4/10	70+110	221.8	0.064	2.38	93.3	322.0	11.05	9.89	0.33

Table A.5. Scan map photometry measurements in the red (160 μm filter) continued.

OBSID	OD	Target	G	Speed ($''/s$)	Rep.	Map params ($''/''/\text{no.}$)	ScanAngles (deg)	f_{aper} (mJy)	σ_{pix} (mJy)	$\sigma_{\text{aper,corr}}$ (mJy)	S/N	f_{star} (mJy)	W_{max} ($''$)	W_{min} ($''$)	ΔW ($''$)
1342190969	284	ϵ Lep	h	20	1	150/4/10	70	160.3	0.265	9.85	16.3	232.8	10.60	9.84	0.27
1342190970	284	ϵ Lep	h	20	1	150/4/10	110	164.2	0.236	8.77	18.7	238.5	11.64	10.58	0.29
1342190969+70	284	ϵ Lep	h	20	2	150/4/10	70+110	161.6	0.188	7.01	23.1	234.6	10.78	9.83	0.41
1342205202	502	ϵ Lep	h	20	1	180/4/10	70	182.0	0.212	7.88	23.1	264.3	10.59	10.48	0.34
1342205203	502	ϵ Lep	h	20	1	180/4/10	110	163.1	0.213	7.92	20.6	236.8	10.79	9.87	0.31
1342205204	502	ϵ Lep	h	20	3	180/4/10	70	148.9	0.141	5.26	28.3	216.2	10.96	9.80	0.19
1342205205	502	ϵ Lep	h	20	3	180/4/10	110	159.6	0.128	4.77	33.4	231.7	11.30	9.94	0.19
..02+03+04+05	502	ϵ Lep	h	20	8	180/4/10	70+110	158.5	0.093	3.44	46.0	230.2	11.01	9.94	0.36
1342214208	640	ϵ Lep	h	20	3	180/4/10	70	155.5	0.135	5.02	31.0	225.9	11.37	9.88	0.19
1342214209	640	ϵ Lep	h	20	3	180/4/10	110	144.5	0.120	4.45	32.5	209.8	10.90	9.72	0.18
1342214208+09	640	ϵ Lep	h	20	6	180/4/10	70+110	150.0	0.088	3.27	45.9	217.9	11.25	9.82	0.24
1342227297	833	ϵ Lep	h	20	1	180/4/10	70	144.3	0.209	7.79	18.5	209.5	11.17	9.65	0.20
1342227298	833	ϵ Lep	h	20	1	180/4/10	110	165.0	0.224	8.34	19.7	239.5	10.90	10.49	0.24
1342227299	833	ϵ Lep	h	20	3	180/4/10	70	150.7	0.127	4.74	31.7	218.8	11.04	9.95	0.19
1342227300	833	ϵ Lep	h	20	3	180/4/10	110	155.8	0.126	4.69	33.2	226.3	10.92	10.15	0.18
297+98+99+300	833	ϵ Lep	h	20	8	180/4/10	70+110	152.8	0.084	3.14	48.7	221.9	10.90	10.08	0.27
1342241333	1034	ϵ Lep	h	20	1	180/4/10	70	156.0	0.238	8.87	17.6	226.5	11.79	9.75	0.23
1342241334	1034	ϵ Lep	h	20	1	180/4/10	110	159.0	0.245	9.10	17.5	230.9	11.24	10.86	0.29
1342241335	1034	ϵ Lep	h	20	3	180/4/10	70	162.9	0.124	4.62	35.3	236.6	11.84	9.93	0.26
1342241336	1034	ϵ Lep	h	20	3	180/4/10	110	156.0	0.134	5.00	31.2	226.6	11.58	9.85	0.24
..33+34+35+36	1034	ϵ Lep	h	20	8	180/4/10	70+110	158.8	0.093	3.44	46.2	230.7	11.78	10.13	0.28
1342263902	1377	ϵ Lep	h	20	3	180/4/10	70	143.9	0.157 ¹	5.84 ¹	24.6 ¹	209.0	10.37	9.60	0.20
1342263903	1377	ϵ Lep	h	20	3	180/4/10	110	143.7	0.157 ¹	5.85 ¹	24.6 ¹	208.6	10.51	9.56	0.22
1342263904	1377	ϵ Lep	h	20	1	180/4/10	70	200.6	0.255 ¹	9.48 ¹	21.2 ¹	291.3	10.67	9.47	0.36
1342263905	1377	ϵ Lep	h	20	1	180/4/10	110	158.6	0.292 ¹	10.85 ¹	14.6 ¹	230.3	11.58	10.67	0.29
..02+03+04+05	1377	ϵ Lep	h	20	8	180/4/10	70+110	151.8	0.100 ¹	3.71 ¹	40.9 ¹	220.4	10.28	9.33	0.44

¹ After OD 1375 half of the red photometer array was lost, resulting in increased noise and reduced S/N wrt. pre-OD 1375 observations

Table A.5. Scan map photometry measurements in the red (160 μm filter) continued.

OBSID	OD	Target	G	Speed ($''/s$)	Rep.	Map params ($''/''/no.$)	ScanAngles (deg)	f_{aper} (mJy)	σ_{pix} (mJy)	$\sigma_{\text{aper,corr}}$ (mJy)	S/N	f_{star} (mJy)	W_{max} ($''$)	W_{min} ($''$)	ΔW ($''$)
1342218544	697	ωCap	h	20	3	180/4/10	70	106.1	0.131	4.89	21.7	154.0	11.65	10.17	0.16
1342218545	697	ωCap	h	20	3	180/4/10	110	115.0	0.122	4.55	25.3	166.9	10.62	9.20	0.16
1342218546	697	ωCap	h	20	3	180/4/10	70	104.4	0.129	4.79	21.8	151.5	10.81	9.45	0.17
1342218547	697	ωCap	h	20	3	180/4/10	110	107.9	0.126	4.70	23.0	156.7	11.13	10.09	0.19
..44+45+46+47	697	ωCap	h	20	12	180/4/10	70+110	107.2	0.063	2.34	45.8	155.7	11.08	10.02	0.25
1342231259	889	ωCap	h	20	3	180/4/10	70	109.9	0.121	4.50	24.4	159.6	10.98	9.85	0.22
1342231260	889	ωCap	h	20	3	180/4/10	110	108.6	0.130	4.83	22.5	157.6	11.05	9.59	0.21
1342231261	889	ωCap	h	20	3	180/4/10	70	110.9	0.130	4.85	22.9	161.1	11.11	9.45	0.21
1342231262	889	ωCap	h	20	3	180/4/10	110	106.8	0.120	4.48	23.8	155.1	10.80	9.95	0.21
..59+60+61+62	889	ωCap	h	20	12	180/4/10	70+110	108.6	0.065	2.43	44.7	157.7	10.62	9.54	0.38
1342243778	1058	ωCap	h	20	3	180/4/10	70	107.9	0.129	4.81	22.4	156.7	10.88	9.60	0.18
1342243779	1058	ωCap	h	20	3	180/4/10	110	116.4	0.126	4.70	24.8	169.0	10.24	9.71	0.21
1342243780	1058	ωCap	h	20	3	180/4/10	70	118.6	0.127	4.71	25.2	172.3	11.66	9.50	0.24
1342243781	1058	ωCap	h	20	3	180/4/10	110	117.9	0.118	4.37	27.0	171.2	11.10	9.99	0.20
..78+79+80+81	1058	ωCap	h	20	12	180/4/10	70+110	115.0	0.060	2.22	51.8	167.0	10.94	9.67	0.33
1342254207	1266	ωCap	h	20	3	180/4/10	70	116.6	0.132	4.89	23.8	169.2	11.77	9.55	0.22
1342254208	1266	ωCap	h	20	3	180/4/10	110	108.6	0.125	4.67	23.3	157.7	10.35	10.20	0.21
1342254209	1266	ωCap	h	20	3	180/4/10	70	108.1	0.136	5.05	21.4	157.0	12.12	9.76	0.23
1342254210	1266	ωCap	h	20	3	180/4/10	110	103.7	0.127	4.74	21.9	150.5	10.84	9.74	0.20
..07+08+09+10	1266	ωCap	h	20	12	180/4/10	70+110	108.3	0.070	2.59	41.8	157.3	11.25	9.82	0.33
1342186142	160	ηDra	h	10	1	120/5/9	80	50.5	0.305	11.37	4.4	73.4	9.86	8.88	0.57
1342186143	160	ηDra	h	10	1	120/5/9	100	58.8	0.285	10.60	5.5	85.4	10.46	9.31	0.46
1342186151	160	ηDra	h	10	1	120/5/9	80	67.9	0.281	10.45	6.5	98.5	11.03	9.87	0.52
1342186152	160	ηDra	h	10	1	120/5/9	100	68.3	0.303	11.28	6.1	99.2	12.95	10.70	0.68
..42+43+51+52	160	ηDra	h	10	4	120/5/9	80+100	60.5	0.162	6.03	10.0	87.9	10.90	9.73	0.44
1342186144	160	ηDra	h	10	1	90/5/9	60	58.4	0.313	11.66	5.0	84.8	11.04	9.84	0.87
1342186145	160	ηDra	h	10	1	90/5/9	120	69.7	0.328	12.22	5.7	101.2	12.57	10.77	0.61
1342186153	160	ηDra	h	10	1	90/5/9	60	55.8	0.339	12.63	4.4	81.0	10.42	6.75	1.00
1342186154	160	ηDra	h	10	1	90/5/9	120	58.4	0.343	12.77	4.6	84.9	12.06	10.81	0.97
..44+45+53+54	160	ηDra	h	10	4	90/5/9	60+120	58.6	0.172	6.41	9.1	85.0	10.94	9.61	0.65
1342186146	160	ηDra	h	20	1	90/5/9	70	93.8	0.367	13.67	6.9	136.2	15.47	11.05	0.70
1342186147	160	ηDra	h	20	1	90/5/9	110	80.4	0.319	11.89	6.8	116.7	10.92	10.14	0.54
1342186155	160	ηDra	h	20	1	90/5/9	70	69.5	0.329	12.22	5.7	100.9	13.48	10.65	0.58
1342186156	160	ηDra	h	20	1	90/5/9	110	80.1	0.294	10.92	7.3	116.4	9.66	8.67	0.77
..46+47+55+56	160	ηDra	h	20	4	90/5/9	70+110	80.1	0.185	6.90	11.6	116.3	11.56	9.90	0.59
1342186148	160	ηDra	h	10	1	150/4/9	85	52.0	0.268	9.98	5.2	75.5	9.93	8.31	0.71
1342186149	160	ηDra	h	10	1	150/4/9	95	60.6	0.284	10.56	5.7	88.0	16.55	11.55	0.61
1342186157	160	ηDra	h	10	1	150/4/9	85	90.5	0.248	9.22	9.8	131.4	10.86	9.43	0.57
1342186158	160	ηDra	h	10	1	150/4/9	95	68.6	0.257	9.54	7.2	99.6	10.62	10.16	0.63
..48+49+57+58	160	ηDra	h	10	4	150/4/9	85+95	67.5	0.144	5.36	12.6	98.0	11.91	9.90	0.52

Table A.5. Scan map photometry measurements in the red (160 μm filter) continued.

OBSID	OD	Target	G	Speed ("/s)	Rep.	Map params ("/"/no.)	ScanAngles (deg)	f_{aper} (mJy)	σ_{pix} (mJy)	$\sigma_{\text{aper,corr}}$ (mJy)	S/N	f_{star} (mJy)	W_{max} (")	W_{min} (")	ΔW (")
1342189191	244	δ Dra	h	20	1	240/4/8	117	36.7	0.266	9.91	3.7	53.2	10.01	9.43	0.48
1342189192	244	δ Dra	h	20	1	240/4/8	63	53.9	0.253	9.41	5.7	78.3	11.57	9.81	0.51
1342189191+92	244	δ Dra	h	20	2	240/4/8	63+117	47.3	0.188	7.01	6.7	68.7	9.76	9.18	0.65
1342212497	607	δ Dra	h	20	3	180/4/10	70	47.4	0.120	4.45	10.7	68.8	10.20	9.89	0.39
1342212498	607	δ Dra	h	20	3	180/4/10	110	65.0	0.126	4.69	13.9	94.4	10.64	10.35	0.34
1342212499	607	δ Dra	h	20	3	180/4/10	70	62.1	0.127	4.71	13.2	90.2	9.87	9.83	0.29
1342212500	607	δ Dra	h	20	3	180/4/10	110	59.0	0.121	4.49	13.1	85.7	10.73	9.99	0.30
..497+98+99+500	607	δ Dra	h	20	12	180/4/10	70+110	58.9	0.058	2.15	27.4	85.5	10.44	10.12	0.41
1342222147	751	δ Dra	h	20	3	180/4/10	70	56.5	0.131	4.88	11.6	82.0	10.38	9.72	0.29
1342222148	751	δ Dra	h	20	3	180/4/10	110	64.0	0.134	4.99	12.8	92.9	11.63	9.74	0.40
1342222149	751	δ Dra	h	20	3	180/4/10	70	58.1	0.124	4.60	12.6	84.3	9.90	9.22	0.30
1342222150	751	δ Dra	h	20	3	180/4/10	110	62.9	0.119	4.41	14.3	91.4	10.92	10.66	0.29
..47+48+49+50	751	δ Dra	h	20	12	180/4/10	70+110	60.5	0.070	2.59	23.4	87.9	10.58	10.08	0.41
1342233571	934	δ Dra	h	20	3	180/4/10	70	58.8	0.120	4.48	13.1	85.4	11.75	9.67	0.27
1342233572	934	δ Dra	h	20	3	180/4/10	110	53.3	0.128	4.77	11.2	77.4	10.84	9.75	0.27
1342233573	934	δ Dra	h	20	3	180/4/10	70	75.4	0.119	4.43	17.0	109.5	10.70	10.33	0.39
1342233574	934	δ Dra	h	20	3	180/4/10	110	59.2	0.132	4.90	12.1	85.9	10.04	9.91	0.31
..71+72+73+74	934	δ Dra	h	20	12	180/4/10	70+110	61.5	0.061	2.29	26.9	89.3	10.66	9.87	0.39
1342250093	1198	δ Dra	h	20	3	180/4/10	70	59.1	0.123	4.57	12.9	85.8	9.50	9.39	0.27
1342250094	1198	δ Dra	h	20	3	180/4/10	110	47.7	0.135	5.03	9.5	69.2	10.49	9.57	0.42
1342250095	1198	δ Dra	h	20	3	180/4/10	70	59.6	0.123	4.58	13.0	86.5	9.83	9.37	0.33
1342250096	1198	δ Dra	h	20	3	180/4/10	110	55.4	0.122	4.53	12.2	80.4	11.12	10.10	0.37
..93+94+95+96	1198	δ Dra	h	20	12	180/4/10	70+110	55.1	0.064	2.39	23.1	80.0	10.45	9.79	0.34
1342257987	1328	δ Dra	h	20	3	180/4/10	70	62.1	0.134	4.98	12.5	90.2	10.82	10.17	0.44
1342257988	1328	δ Dra	h	20	3	180/4/10	110	53.5	0.129	4.79	11.2	77.7	10.25	9.94	0.29
1342257989	1328	δ Dra	h	20	3	180/4/10	70	61.6	0.122	4.55	13.5	89.4	11.16	10.74	0.56
1342257990	1328	δ Dra	h	20	3	180/4/10	110	59.6	0.114	4.24	14.1	86.5	10.06	9.64	0.32
..87+88+89+90	1328	δ Dra	h	20	12	180/4/10	70+110	58.6	0.074	2.74	21.4	85.1	10.69	10.18	0.38
1342184574	139	θ Umi	h	10	1	210/15/4	90	37.3	0.412	15.32	2.4	54.1	10.55	8.47	0.86
1342184585	139	θ Umi	h	10	1	210/15/4	90	79.3	0.351	13.07	6.1	115.1	11.45	8.32	1.05
1342184574+85	139	θ Umi	h	10	2	210/15/4	90	56.1	0.311	11.59	4.8	81.4	9.89	7.88	0.80
1342184575	139	θ UMi	h	20	1	210/15/4	90	50.5	0.454	16.89	3.0	73.3	9.69	6.51	0.51
1342184586	139	θ Umi	h	20	1	210/15/4	90	47.2	0.412	15.33	3.1	68.5	12.96	10.53	1.12
1342184575+86	139	θ Umi	h	20	2	210/15/4	90	48.7	0.353	13.13	3.7	70.8	10.42	8.37	0.49
1342191982	300	θ Umi	h	20	6	150/4/10	70	41.4	0.091	3.38	12.2	60.1	10.95	9.94	0.38
1342191983	300	θ Umi	h	20	6	150/4/10	110	44.6	0.096	3.58	12.5	64.8	10.65	9.61	0.36
1342191982+83	300	θ Umi	h	20	12	150/4/10	70+110	42.6	0.067	2.50	17.0	61.9	10.72	9.77	0.40

Table A.5. Scan map photometry measurements in the red (160 μm filter) continued.

OBSID	OD	Target	G	Speed ("/s)	Rep.	Map params ("/no.)	ScanAngles (deg)	f_{aper} (mJy)	σ_{pix} (mJy)	$\sigma_{\text{aper,cor}}$ (mJy)	S/N	f_{star} (mJy)	W_{max} (")	W_{min} (")	ΔW (")
1342190972	284	HD 41047	h	20	3	150/4/10	70	28.4	0.137	5.09	5.6	41.3	12.15	9.94	0.80
1342190973	284	HD 41047	h	20	3	150/4/10	110	21.3	0.125	4.64	4.6	30.9	10.40	8.22	0.45
1342190972+73	284	HD 41047	h	20	6	150/4/10	70+110	24.1	0.086	3.22	7.5	35.0	10.63	8.95	0.64
1342203111	460	42 Dra	h	20	20	180/4/10	70	18.1	0.061	2.25	8.0	26.4	11.89	10.30	0.41
1342203112	460	42 Dra	h	20	20	180/4/10	110	20.6	0.059	2.19	9.4	29.9	10.47	9.64	0.42
1342203113	460	42 Dra	h	20	20	180/4/10	70	18.5	0.057	2.12	8.7	26.9	11.08	9.42	0.32
1342203114	460	42 Dra	h	20	20	180/4/10	110	20.5	0.054	2.02	10.1	29.8	9.99	9.82	0.31
..11+12+13+14	460	42 Dra	h	20	80	180/4/10	70+110	20.2	0.031	1.16	17.4	29.4	10.38	9.64	0.44
1342243730	1057	42 Dra	h	20	20	180/4/10	70	22.6	0.056	2.10	10.8	32.8	11.08	9.93	0.34
1342243731	1057	42 Dra	h	20	20	180/4/10	110	17.8	0.054	2.02	8.8	25.8	10.86	10.06	0.32
1342243732	1057	42 Dra	h	20	20	180/4/10	70	19.7	0.057	2.13	9.2	28.6	11.34	10.23	0.24
1342243733	1057	42 Dra	h	20	20	180/4/10	110	17.6	0.052	1.95	9.0	25.6	10.59	9.56	0.36
..30+31+32+33	1057	42 Dra	h	20	80	180/4/10	70+110	19.3	0.032	1.18	16.4	28.1	10.87	9.94	0.30
1342184302	132	HD 138265	h	10	3	210/4/25	90	24.7	0.085	3.16	7.8	35.9	9.92	8.68	0.54
1342184303	132	HD 138265	h	20	3	210/4/25	90	18.2	0.091	3.38	5.4	26.4	11.34	10.88	0.54
1342188841	233	HD 138265	h	20	21	240/4/8	63	21.1	0.068	2.55	8.3	30.6	11.44	10.85	0.45
1342188842	233	HD 138265	h	20	21	240/4/8	117	20.4	0.059	2.21	9.2	29.6	11.44	11.40	0.57
1342188841+42	233	HD 138265	h	20	42	240/4/8	63+117	21.3	0.044	1.65	12.9	31.0	11.39	11.04	0.53
1342191986	300	HD 138265	h	20	6	150/4/10	70	9.8	0.102	3.81	2.6	14.2	9.99	8.64	0.93
1342191987	300	HD 138265	h	20	6	150/4/10	110	22.5	0.095	3.52	6.4	32.7	11.59	8.76	0.54
1342191986+87	300	HD 138265	h	20	12	150/4/10	70+110	16.6	0.067	2.51	6.6	24.2	11.16	9.79	0.87
1342227973	843	HD 152222	h	20	33	180/4/10	70	5.6	0.035	1.31	4.3	8.1	12.98	10.77	0.69
1342227974	843	HD 152222	h	20	33	180/4/10	110	4.0	0.039	1.44	2.8	5.8	12.42	9.86	0.78
1342227973+74	843	HD 152222	h	20	66	180/4/10	70+110	4.5	0.030	1.11	4.1	6.5	12.89	10.50	0.54
1342240702	1028	HD 152222	h	20	6	180/4/10	70	6.5	0.079	2.93	2.2	9.5	10.20	8.42	1.69
1342240703	1028	HD 152222	h	20	6	180/4/10	110	5.8	0.086	3.20	1.8	8.5	9.77	9.45	1.13
1342240702+03	1028	HD 152222	h	20	12	180/4/10	70+110	6.1	0.055	2.05	3.0	8.9	9.48	8.89	1.07
1342198535	400	HD 39608	h	20	10	180/4/10	70	7.2	0.067	2.50	2.9	10.4	14.24	8.77	0.89
1342198536	400	HD 39608	h	20	10	180/4/10	110	13.6	0.069	2.58	5.3	19.7	13.19	11.59	1.71
1342198537	400	HD 39608	h	20	35	180/4/10	70	7.9	0.042	1.57	5.0	11.5	11.58	8.24	0.93
1342198538	400	HD 39608	h	20	35	180/4/10	110	8.8	0.043	1.59	5.5	12.7	11.55	7.63	0.80
..35+36+37+38	400	HD 39608	h	20	90	180/4/10	70+110	8.6	0.031	1.15	7.5	12.5	11.05	9.23	1.24

Appendix B: Chopped photometry

Appendix B.1: Photometry results of individual measurements

Individual photometric results for the 70, 100, and 160 μm filters are compiled in Tables B.1 to B.3. The applied radius for the photometric aperture was 5.6, 6.8 and 10.7'' for the 70, 100 and 160 μm filter, respectively. The number of output pixels (1''1, 1''4, and 2''1 size, respectively) inside this photometric aperture is $N_{\text{aper}} = 81.42, 74.12, \text{ and } 81.56$, respectively. The corresponding correction factor for correlated noise are $f_{\text{corr}} = 6.33, 4.22, \text{ and } 7.81$, respectively. Aperture correction factors are $c_{\text{aper}} = 1.61, 1.56 \text{ and } 1.56$ for the 70, 100 and 160 μm filter, respectively. Proper motion correction was applied throughout.

The tables contain the following information: Col. 1: Unique observational identifier (OBSID) of the PACS observation; Col. 2: Herschel Observational Day (OD), including its phase; Col. 3: Target name; Col. 4: Applied gain (G) of the PACS bolometer electronics: h(igh)/l(ow); Col. 5: Chopper dither pattern: y(es)/n(o); Col. 6: Number of repetitions (rep.) of the basic chop/nod cycle; Col. 7: Fitted peak flux intensity of the source; Col. 8: Measured flux inside the photometric aperture of this filter, f_{aper} ; Col. 9: Noise per pixel, σ_{pix} ; Col. 10: Noise corrected for correlated noise inside the measurement aperture, f_{aper} , according to Eq. 4. Col. 11: Achieved signal-to-noise ratio according to Eq. 5; Col. 12: Stellar flux f_{star} according to Eq. 1; Cols. 13+14: Maximum and minimum Full Width (W) Half Maximum (in '') of the source PSF.

Table B.1. Chop-nod photometry measurements in the blue ($70\ \mu\text{m}$ filter). Processing proceeded from SPG v1.1.1.0 level 1 products with HIPE version 13 build 2768. Gyro correction was applied for most of the cases.

OBSID	OD	Target	G	Dith	Rep.	FitPeak (mJy)	f_{aper} (mJy)	σ_{pix} (mJy)	$\sigma_{\text{aper,corr}}$ (mJy)	S/N	f_{star} (mJy)	W_{max} ($''$)	W_{min} ($''$)
1342217347	684.191528	β Gem	h	y	3	53.535	1608.2	0.193	11.0	146	2569.7	6.48	5.78
1342184267	132.284763	ε Lep	l	y	1	27.686	734.0	0.335	19.1	38	1172.8	5.75	5.10
1342184268	132.287321	ε Lep	h	y	1	28.453	742.0	0.242	13.8	54	1185.6	5.81	5.00
1342186141	160.373009	η Dra	h	y	2	10.717	318.8	0.161	9.2	35	509.4	5.86	5.72
1342182975	108.553912	δ Dra	h	y	2	9.897	266.8	0.156	8.9	30	426.3	5.74	5.17
1342182976	108.558322	δ Dra	h	n	2	9.963	277.2	0.159	9.1	31	443.0	5.89	5.06
1342184293	132.472674	δ Dra	l	y	2	10.015	277.2	0.193	11.0	25	443.0	6.12	5.17
1342184496	138.176215	δ Dra	h	y	2	10.630	276.2	0.167	9.5	29	441.4	5.72	4.94
1342189190	244.175625	δ Dra	h	y	4	9.234	275.8	0.110	6.3	44	440.6	5.86	5.74
1342184576	139.165067	θ Umi	h	y	1	6.432	181.9	0.213	12.2	15	290.6	5.74	5.57
1342184577	139.167625	θ Umi	h	y	1	6.331	179.8	0.217	12.4	15	287.4	5.88	5.32
1342184578	139.170194	θ Umi	h	y	1	6.572	180.0	0.227	13.0	14	287.5	5.72	5.15
1342184579	139.173559	θ Umi	h	y	1	5.950	169.0	0.230	13.1	13	270.1	5.68	5.36
1342184580	139.175344	θ Umi	h	y	1	6.210	185.0	0.217	12.4	15	295.6	6.11	5.46
1342184581	139.177889	θ Umi	h	y	1	6.496	183.3	0.230	13.1	14	292.9	5.99	5.32
1342184582	139.180494	θ Umi	h	y	1	6.295	174.9	0.231	13.2	13	279.5	5.83	5.16
1342184583	139.183086	θ Umi	h	y	1	6.193	181.7	0.239	13.7	13	290.3	6.07	5.50
1342184584	139.185678	θ Umi	h	y	1	6.477	180.8	0.250	14.3	13	288.8	5.74	5.54
1342191981	300.807361	θ Umi	h	y	20	5.745	175.0	0.052	3.0	59	279.6	6.18	5.65
1342184296	132.725098	HD 138265	h	y	43	2.530	70.8	0.033	1.9	38	113.2	5.69	5.33
1342184297	132.775573	HD 138265	h	y	10	2.457	71.0	0.067	3.8	19	113.5	5.66	5.61
1342184298	132.797749	HD 138265	h	y	10	2.588	69.7	0.063	3.6	19	111.4	5.63	5.21
1342185441	146.197794	HD 138265	h	y	1	2.424	72.0	0.122	7.0	10	115.0	5.77	5.40
1342185442	146.211433	HD 138265	h	y	2	2.360	66.6	0.087	5.0	13	106.4	5.95	5.17
1342185443	146.224583	HD 138265	h	y	4	2.504	72.4	0.077	4.4	16	115.6	5.95	5.40
1342185444	146.238106	HD 138265	h	y	7	2.230	66.4	0.083	4.7	14	106.1	6.09	5.45
1342185445	146.251663	HD 138265	h	y	12	2.272	70.9	0.085	4.9	15	113.2	6.11	5.73
1342191984	300.874850	HD 138265	h	y	10	2.354	72.0	0.067	3.8	19	115.0	5.96	5.71
1342186162	160.492905	HD 159330	h	y	10	1.486	37.7	0.067	3.8	9.9	60.3	5.45	5.04
1342191963	300.492037	HD 152222	h	y	20	0.890	24.2	0.045	2.6	9.4	38.7	5.62	5.37
1342182953	108.195255	HD 15008	h	n	10	0.537	14.3	0.060	3.4	4.2	22.8	6.30	4.81
1342182956	108.254317	HD 15008	h	y	10	0.482	13.7	0.074	4.2	3.2	21.9	5.72	5.33
1342183928	125.490660	HD 15008	h	y	16	0.483	14.0	0.057	3.3	4.3	22.4	6.11	5.44
1342192766	316.230382	HD 15008	h	y	45	0.411	11.7	0.035	2.0	5.9	18.7	6.04	5.11

Table B.2. Chop-nod photometry measurements in the green (100 μm filter). Processing proceeded from SPG v11.1.0 level 1 products with HIPE version 13 build 2768. Gyro correction was applied for most of the cases.

OBSID	OD	Target	G	Dith	Rep.	FitPeak (mJy)	f_{aper} (mJy)	σ_{pix} (mJy)	$\sigma_{\text{aper,corr}}$ (mJy)	S/N	f_{star} (mJy)	W_{max} (")	W_{min} (")
1342217350	684.218345	β Gem	h	y	3	30.688	829.6	0.240	8.7	95	1266.7	7.47	7.01
1342184266	132.282205	ϵ Lep	h	y	1	15.193	379.8	0.352	12.8	30	579.9	7.08	6.39
1342190968	284.817118	ϵ Lep	h	y	2	13.141	360.1	0.250	9.1	40	549.8	7.82	6.63
1342186150	160.410127	η Dra	h	y	2	6.269	154.4	0.241	8.8	18	235.7	6.78	6.70
1342182977	108.562731	δ Dra	h	y	2	5.643	137.5	0.258	9.4	15	210.0	7.01	6.08
1342182978	108.567141	δ Dra	h	n	2	5.247	136.1	0.233	8.5	16	207.8	6.91	6.68
1342184294	132.477141	δ Dra	l	y	2	5.513	147.5	0.307	11.2	13	225.2	7.49	6.65
1342184587	139.193292	θ Umi	h	y	1	3.456	90.8	0.311	11.3	8.0	138.7	7.18	6.41
1342184588	139.195850	θ Umi	h	y	1	3.242	100.2	0.344	12.5	8.0	153.0	7.68	7.39
1342184589	139.198419	θ Umi	h	y	1	3.801	91.8	0.351	12.8	7.2	140.2	6.84	6.00
1342184590	139.200953	θ Umi	h	y	1	3.744	101.6	0.358	13.0	7.8	155.2	7.88	6.11
1342184591	139.203546	θ Umi	h	y	1	3.605	100.2	0.365	13.3	7.6	153.0	7.28	7.00
1342184592	139.206138	θ Umi	h	y	1	3.395	87.8	0.366	13.3	6.6	134.0	6.92	6.59
1342184593	139.209497	θ Umi	h	y	1	3.479	94.6	0.324	11.8	8.0	144.4	7.55	6.58
1342184594	139.211300	θ Umi	h	y	1	4.149	84.3	0.346	12.6	6.7	128.8	6.04	5.85
1342184595	139.213881	θ Umi	h	y	1	3.024	84.7	0.346	12.6	6.7	129.3	7.67	6.89
1342190971	284.837708	HD 41047	h	y	10	2.244	57.5	0.107	3.9	15	87.8	7.31	6.37
1342184299	132.819914	HD 138265	h	y	10	1.380	38.1	0.102	3.7	10	58.2	7.73	6.58
1342184300	132.842102	HD 138265	h	y	10	1.456	39.5	0.082	3.0	13	60.4	7.16	6.68
1342184301	132.874606	HD 138265	h	y	20	1.255	39.0	0.073	2.7	15	59.5	7.93	7.23
1342191985	300.901319	HD 138265	h	y	20	1.339	38.4	0.075	2.7	14	58.6	7.69	7.07
1342184503	138.314253	HD 159330	h	y	21	0.817	21.0	0.071	2.6	8.1	32.1	6.80	6.72
1342186159	160.456273	HD 159330	h	y	10	0.804	22.5	0.090	3.3	6.9	34.3	7.99	6.54
1342192782	316.508530	HD 159330	h	y	45	0.685	18.8	0.055	2.0	9.4	28.8	7.52	6.77

Table B.3. Chop-nod photometry measurements in the red ($160\ \mu\text{m}$ filter). Processing proceeded from SPG v1.1.0 level 1 products with HIPE version 13 build 2768. Gyro correction was applied for most of the cases.

OBSID	OD	Target	G	Dith	Rep.	FitPeak (mJy)	f_{aper} (mJy)	σ_{pix} (mJy)	$\sigma_{\text{aper,corr}}$ (mJy)	S/N	f_{star} (mJy)	W_{max} ($''$)	W_{min} ($''$)
1342217347	684.191528	β Gem	h	y	3	10.781	343.7	0.337	23.8	14	499.1	13.10	10.38
1342217350	684.218345	β Gem	h	y	3	10.574	340.7	0.325	22.9	15	494.7	13.22	10.64
1342184266	132.282205	ϵ Lep	h	y	1	5.147	142.5	0.504	35.5	4.0	206.9	11.07	9.83
1342184267	132.284763	ϵ Lep	l	y	1	5.435	158.3	0.557	39.3	4.0	229.9	10.66	10.64
1342184268	132.287321	ϵ Lep	h	y	1	5.109	136.5	0.542	38.2	3.6	198.2	12.01	8.99
1342190968	284.817118	ϵ Lep	h	y	2	4.458	136.1	0.365	25.7	5.3	197.7	13.16	9.62
1342186141	160.373009	η Dra	h	y	2	2.442	64.2	0.304	21.4	3.0	93.2	12.53	8.87
1342186150	160.410127	η Dra	h	y	2	2.297	75.0	0.308	21.7	3.5	109.0	13.05	10.62
1342182975	108.553912	δ Dra	h	y	2	1.652	46.6	0.315	22.2	2.1	67.7	14.38	8.78
1342182976	108.558322	δ Dra	h	n	2	2.125	58.4	0.395	27.9	2.1	84.8	12.78	8.86
1342182977	108.562731	δ Dra	h	y	2	1.935	52.3	0.341	24.1	2.2	75.9	11.93	9.24
1342182978	108.567141	δ Dra	h	n	2	2.034	69.5	0.363	25.6	2.7	100.9	13.40	10.73
1342184293	132.472674	δ Dra	l	y	2	1.791	57.5	0.344	24.3	2.4	83.4	13.26	8.97
1342184294	132.477141	δ Dra	l	y	2	1.848	60.8	0.365	25.7	2.4	88.2	13.65	10.34
1342184496	138.176215	δ Dra	h	y	2	1.950	59.8	0.367	25.9	2.3	86.8	13.38	9.68
1342189190	244.175625	δ Dra	h	y	4	1.882	57.5	0.216	15.2	3.8	83.6	12.21	10.06
1342184576	139.165067	θ Umi	h	y	1	1.727	55.3	0.387	27.3	2.0	80.4	12.84	8.89
1342184577	139.167625	θ Umi	h	y	1	1.602	44.5	0.448	31.6	1.4	64.7	10.84	9.92
1342184578	139.170194	θ Umi	h	y	1	1.711	33.8	0.460	32.4	1.0	49.1	11.09	6.68
1342184579	139.173559	θ Umi	h	y	1	1.289	24.4	0.456	32.2	0.8	35.5	16.28	6.06
1342184580	139.175344	θ Umi	h	y	1	2.036	39.0	0.490	34.6	1.1	56.6	10.66	6.32
1342184581	139.177889	θ Umi	h	y	1	1.125	37.4	0.518	36.5	1.0	54.3	11.85	10.21
1342184582	139.180494	θ Umi	h	y	1	1.284	46.6	0.521	36.7	1.3	67.6	19.99	8.28
1342184587	139.193292	θ Umi	h	y	1	2.785	43.8	0.332	23.4	1.9	63.7	8.80	7.25
1342184588	139.195850	θ Umi	h	y	1	1.454	34.2	0.465	32.8	1.0	49.6	9.90	9.37
1342184589	139.198419	θ Umi	h	y	1	1.704	41.1	0.505	35.6	1.2	59.6	12.59	7.97
1342184590	139.200953	θ Umi	h	y	1	1.516	45.3	0.483	34.1	1.3	65.8	16.06	8.04
1342184591	139.203546	θ Umi	h	y	1	1.499	42.2	0.520	36.7	1.2	61.3	12.55	8.36
1342184592	139.206138	θ Umi	h	y	1	2.357	63.1	0.549	38.7	1.6	91.6	12.02	9.29
1342184593	139.209497	θ Umi	h	y	1	1.547	37.3	0.409	28.8	1.3	54.2	14.40	6.77
1342184594	139.211300	θ Umi	h	y	1	2.035	30.5	0.527	37.2	0.8	44.2	9.37	7.05
1342191981	300.807361	θ Umi	h	y	20	1.139	36.3	0.108	7.6	4.8	52.8	13.36	10.17

Table B.3. continued. Chop-nod photometry measurements in the red (160 μm filter).

OBSID	OD	Target	G	Dith	Rep.	FitPeak (mJy)	f_{aper} (mJy)	σ_{pix} (mJy)	$\sigma_{\text{aper,corr}}$ (mJy)	S/N	f_{star} (mJy)	W_{max} ($''$)	W_{min} ($''$)
1342190971	284.837708	HD 41047	h	y	10	0.684	19.7	0.164	11.6	1.7	28.6	11.03	9.64
1342184296	132.725098	HD 138265	h	y	43	0.604	20.2	0.104	7.3	2.8	29.4	12.31	11.22
1342184297	132.775573	HD 138265	h	y	10	0.672	25.2	0.150	10.6	2.4	36.5	13.82	11.12
1342184298	132.797749	HD 138265	h	y	10	0.657	26.5	0.142	10.0	2.6	38.4	14.26	11.84
1342184299	132.819914	HD 138265	h	y	10	0.705	21.7	0.144	10.2	2.1	31.5	13.72	9.04
1342184300	132.842102	HD 138265	h	y	10	0.755	22.1	0.139	9.8	2.3	32.1	12.87	8.97
1342184301	132.874606	HD 138265	h	y	20	0.618	20.9	0.129	9.1	2.3	30.3	13.21	10.56
1342185443	146.224583	HD 138265	h	y	4	0.724	17.9	0.168	11.8	1.5	26.0	11.20	8.61
1342185444	146.238106	HD 138265	h	y	7	0.708	18.4	0.167	11.8	1.6	26.7	14.15	7.47
1342185445	146.251663	HD 138265	h	y	12	0.755	18.7	0.185	13.0	1.4	27.2	12.88	7.93
1342191984	300.874850	HD 138265	h	y	10	0.653	23.1	0.151	10.7	2.2	33.5	14.90	10.40
1342191985	300.901319	HD 138265	h	y	20	0.616	19.5	0.124	8.8	2.2	28.4	13.16	10.10

Appendix C: Comparison scan map with chop/nod photometry

In Table C.1 we list the flux ratios of scan map photometry and chop/nod photometry for ten sources, which were observed in both modes. The comparison between the two photometry modes gives the following result:

For 70 μm photometry, the consistency of the fluxes is better than 3% for seven out of nine sources. The two excursions, HD 159330 and HD 15008, are consistent within the larger error margin which is caused by a larger uncertainty because of only one chop/nod measurement (HD 159330) or the faintness of the source (HD 15008).

For 100 μm photometry, the consistency of the fluxes is better than 2% for five out of eight sources. For HD 138265 the flux consistency is $\approx 4\%$, but the derived error margin is smaller. For η Dra and HD 41047 there is only one chop/nod measurement, which introduces a high uncertainty, but fluxes are consistent within the error margin.

For 160 μm photometry, the consistency of the fluxes is better than 3% for four out of seven sources. For ε Lep the scan map flux is 9% higher than the chop/nod one. There is only a small (4) number of chop/nod measurements versus a large (18) number of scan map measurements. We therefore consider the scan map mode result as the more reliable one. The opposite is the case for the number of photometric measurements of θ Umi, with 2 scan map measurements versus 16 chop/nod measurements. Here the scan map flux is 13% higher than the chop/nod one. However, the 2 scan map measurements, each with 6 repetitions, have the best S/N of all measurements and are therefore quite reliable. Fifteen out of 16 chop/nod measurements have a repetition factor of only 1. They still allow a reasonable detection of the source at the expected location but show considerable scatter in the resulting (colour-corrected) fluxes between 35.5 and 91.6 mJy (expected flux according to the model: 53.9 mJy). Only one chop/nod measurement has 20 repetitions with a S/N comparable to the two scan maps. Its resulting flux of 52.8 mJy is 13% lower than the average 60.9 mJy from the two scan maps. Here we should note that the annulus used for background determination is closer to the source and narrower for chop/nod aperture photometry (radius 24 – 28", Nielbock et al. (2013)) than for scan map photometry (radius 35 – 45", Balog et al. (2014)). As we discuss in Sect. 5.2, the scan map measurements prove contamination of the source flux by FIR cirrus emission in the order of 10% explaining the excess over the model flux. The maps also show that there is additional emission around the source which is much more picked up by the background annulus of the chop/nod photometry, resulting in a higher subtracted background value. This leads to the result that the chop/nod photometry is close to the expected model flux, because the underlying cirrus emission is by chance properly compensated for by the background subtraction, while the scan map photometry reveals the extra emission inside the aperture. The photometric result must therefore be associated by an additional uncertainty of 10%, because the background subtraction strongly depends on the selected background area geometry (c.f. Table 7). For HD 41047 there is only one chop/nod measurement with a very high assigned flux uncertainty, so that also the flux ratio of scan map to chop/nod photometry is highly uncertain.

Table C.1. Ratios of fluxes obtained in scan map mode photometry (Table 7) versus chop/nod mode photometry (Table 8) as a measure of consistency between the two photometry modes. Values in italics have a high uncertainty.

HD	Name	$R_{70}^{S/C}$	$R_{100}^{S/C}$	$R_{160}^{S/C}$
62509	β Gem	1.031 \pm 0.005	1.014 \pm 0.011	1.000 \pm 0.006
32887	ε Lep	0.987 \pm 0.006	1.019 \pm 0.025	1.093 \pm 0.038
148387	η Dra	0.993 \pm 0.034	1.059 \pm 0.068	0.969 \pm 0.095
180711	δ Dra	0.992 \pm 0.007	1.002 \pm 0.009	1.026 \pm 0.043
139669	θ Umi	1.009 \pm 0.008	1.018 \pm 0.043	1.131 \pm 0.070
41047	HR 2131		1.101 \pm 0.063	<i>1.248\pm0.652</i>
138265	HR 5755	1.001 \pm 0.011	0.958 \pm 0.011	1.000 \pm 0.050
159330	HR 6540	1.076 \pm 0.118	1.016 \pm 0.116	–
152222		1.008 \pm 0.099	–	–
15008	δ Hyi	1.110 \pm 0.064	–	–

Appendix D: ISOPHOT Highly Processed Data Product (HPDP) photometry

Table D.1. ISOPHOT (Lemke et al. 1996) Highly Processed Data Product (HPDP) photometry of P22 mini-maps of normal stars (<https://www.cosmos.esa.int/web/iso/highly-processed-data-products>; Moór et al., 2003, "Far-infrared observations of normal stars measured with ISOPHOT in mini-map mode"). The values in column f_ν are the original HPDP fluxes (for $\text{SED} \propto \nu^{-1}$). They have to be divided by the colour-correction factor cc , which is for a 5000 K BB SED.

Star	Filter	λ_c (μm)	ISO TDT no.	f_ν (mJy)	cc
α Ari	C_180	180	79001902	314 \pm 19	1.10
ε Lep	C_60	60	65701315	1779 \pm 71	1.06
	C_50	65	65701312	1835 \pm 65	1.29
	C_70	80	65701309	1113 \pm 46	1.23
	C_90	90	65701318	918 \pm 64	1.17
	C_100	100	65701306	692 \pm 36	1.10
	C_105	105	65701303	601 \pm 44	1.05
	C_120	120	65002709	507 \pm 43	1.21
	C_135	150	65002103	292 \pm 21	1.10
	C_160	170	65002406	225 \pm 21	1.20
ω Cap	C_60	60	72701415	1232 \pm 65	1.06
	C_50	65	72701412	1258 \pm 45	1.29
	C_70	80	72701409	779 \pm 32	1.23
	C_90	90	72701418	543 \pm 38	1.17
	C_100	100	72701406	490 \pm 25	1.10
	C_105	105	72701403	441 \pm 32	1.05
	C_120	120	73401709	337 \pm 28	1.21
	C_135	150	73401603	221 \pm 16	1.10
	C_160	170	73401706	219 \pm 26 ⁽¹⁾	1.20
η Dra	C_90	90	78300677	365 \pm 26	1.17
	C_160	170	35800501	123 \pm 16	1.20

⁽¹⁾ Measurement not used in Fig. 11